Comparing galaxy-galaxy(-galaxy) lensing in semi-analytic models and observations to study galaxy evolution

Dissertation
zur
Erlangung des Doktorgrades (Dr. rer. nat.)
der
Mathematisch-Naturwissenschaftlichen Fakultät
der
Rheinischen Friedrich-Wilhelms-Universität Bonn

von
Hananeh Saghiha
aus
Teheran (Iran)

Bonn, December 2016

Dieser Forschungsbericht wurde als Dissertation von der Mathematisch-Naturwissenschaftlichen Fakultät der Universität Bonn angenommen und ist auf dem Hochschulschriftenserver der ULB Bonn http://hss.ulb.uni-bonn.de/diss_online elektronisch publiziert.

1. Gutachter:	Prof. Dr. Peter Schneider
2. Gutachter:	Prof. Dr. Cristiano Porciani
Tag der Promotion:	19.12.2016
Erscheinungsjahr:	2017

For my parents.

Abstract

One of the main challenges in cosmology is to understand the properties of dark matter, its distribution in the Universe, and its connection with baryonic matter. An ideal method to study the relation between baryonic matter and dark matter is the so-called "gravitational lensing". It relies on the fact that the light emitted from a background source in the distant Universe is deflected by the foreground matter distribution or "lens", leading to distortions in the observed image of the source. By studying these image distortions, one can obtain information about the mass distribution associated with the lens. In the weak gravitational lensing regime, the lensing effect is too small to create a detectable lensing signal from a single image. One thus needs to examine the distortions in a large number of sources in order to derive statistical properties about the lenses mass.

In the case where both the source and the lens are galaxies, this technique is known as "galaxy-galaxy lensing" (GGL). Distortion patterns around lens galaxy pairs instead of individual galaxies can also be analysed, a method known as "galaxy-galaxy-galaxy lensing" (G3L) which gives information on the matter environment of galaxy pairs. In order to be able to interpret GGL and G3L measurements, a theoretical understanding of these statistics is required. A common approach is to use semi-analytic models (SAMs) which combine the results from dark matter N-body simulations with analytical prescriptions for the physical processes governing galaxy formation and evolution. Comparing the outcomes of SAMs with observations therefore offers an opportunity to connect observed properties of galaxies with the underlying physical processes leading to those features.

In this thesis, we first use synthetic galaxy catalogs from two SAMs, the Garching and Durham models, and their predictions of GGL and G3L for various galaxy populations. These SAMs are all implemented on one of the largest dark matter simulations, the Millennium Simulation. However, they differ in several details which lead to different predictions of GGL and G3L. Therefore, comparing the SAMs predictions against each other allows us to gain information on the physical processes involved and how the different treatments used in the models impact the signal. Moreover, comparisons between the SAMs predictions of GGL and G3L suggest that G3L provides new information which cannot be obtained from the second-order GGL statistics alone.

In order to identify shortcomings of the SAMs and obtain valuable information on how to improve the models, one needs to compare the SAMs results with observational measurements. Therefore, in the second part of this thesis, we investigate the ability of three SAMs, the Garching and Durham models as well as an updated version of the Garching model, to reproduce observations of GGL and G3L. For this purpose, we use measurements from the Canada-France-Hawaii Telescope Lensing Survey (CFHTLenS) which is a multi-color optical survey optimised for weak lensing analysis. We study the GGL and G3L signals for galaxy samples selected according to their stellar mass and redshift, and analyze the clustering properties of galaxies and galaxy pairs of these samples. Our results indicate that not all models can quantitatively reproduce the GGL and G3L observations although there is an overall qualitative agreement between the models and CFHTLenS data.

Contents

List of Figures

List of Tables

CHAPTER 1

Introduction

The word "galaxy" originates from the greek *galaxias* which means "milky", referring to our own galaxy the Milky Way. It is only about 100 years that we know the Milky Way is not the only galaxy in the Universe. This is thanks to the pioneering work of Edwin Hubble who discovered "nebulae" (later to be know as galaxies) outside our galaxy and marked the beginning of a new era in the field of astronomy, the *extragalactic astronomy*. Since then, we have observed billions of galaxies in the Universe. These objects come in different flavours: they can have different shapes (elliptical, spiral, irregular) and colors (red, blue), thus indicating how the history and evolution can change from one galaxy to another. The major problem related to our understanding of galaxies was without any doubt the discrepancy between the rotation curves observed in spiral galaxies (such as in the Milky Way, M31, and M33), and the mass estimates of galaxies inferred by the visible light. Instead of decreasing with respect to their distance to the centre of the galaxy, the orbital speeds of stars and dust in the galaxy were increasing. This problem was solved by the existence of an additional matter component that is not observable, hence called "dark matter". Understanding the nature of the dark matter and what it is made of is one of the great challenges in physics and astronomy.

We have observations of galaxies and clusters of galaxies that can only be explained by the existence of dark matter, and that it interacts with visible matter only via gravity. The Bullet cluster, shown in Fig. 1.1, is a nice example of such observations. The Bullet cluster consists of two clusters of galaxies that have recently collided. The different components of the clusters (stars, gas, dark matter) behave differently during the collision. The stars in the galaxies of the two clusters are observed in optical waveband and the hot gas of clusters is observed in X-ray. Since the mass of the cluster is higher than the mass in stars, it is expected that the mass concentration should fit the X-ray concentration (red). However, from the observed gravitation lensing effect of the cluster, the cluster mass is concentrated on the galaxy distribution (blue). This provides a strong evidence that dark matter exists and that it can only be "observed" through its gravitational effect.

The standard theory of gravity that we use is general relativity published by Albert Einstein in 1915. It concerns the effect of gravity on space and time and how the presence of matter and energy changes the geometry of space-time. In particular, the distortions of space-time caused by the gravitational field of a matter distribution, affects how lights travels. This phenomenon is called *gravitational lensing*. As an example, the light from a distant galaxy is distorted in shape and size when passing near another galaxy: this is the galaxy-galaxy lensing (GGL) effect. The gravitational field of the foreground galaxy is dominated by the dark matter component rather than the luminous matter. Therefore the observed

Figure 1.1: The Bullet cluster consisting of two clusters of galaxies colliding. The X-ray emission by the hot gas in the cluster is shown in red and dark matter concentration by gravitational lensing effect in blue. The fact that there is a clear separation between the two and that the cluster mass is higher than the visible mass in stars and gas, is a direct evidence of dark matter and that it interacts only gravitationally with the visible matter. Credits: Optical: NASA/STScI; Magellan/U.Arizona/D.Clowe et al.; X-ray: NASA/CXC/CfA/ M.Markevitch et al.; Lensing Map: NASA/STScI; ESO WFI; Magellan/U.Arizona/ D.Clowe et al.

distortion in the image of the background galaxy contains information on the dark matter content of the foreground galaxy.

Galaxies are not isolated objects. Rather they are found in groups and clusters of galaxies. In the past decade, the concept of galaxy-galaxy lensing has been developed to third-order galaxy-galaxy-galaxy lensing (G3L). The third-order correlation functions in this case probe the distortion pattern, or *shear profile*, around clustered pairs of foreground galaxies. G3L contains information on the common dark matter halo of galaxy pairs. Recent measurements of G3L indicate that when considering triplets of galaxies (one background and two foreground galaxies) the G3L correlator shows an excess in the shear profile around foreground pairs relative to the individual shear profiles.

The interpretation of GGL and G3L require a theoretical understanding of these statistics. A common approach is to use numerical simulations which are more accurate than, for example, analytical methods. Since dark matter is the dominant matter component in the Universe, we can use dark matter-only N-body simulations to study gravitational effects. To include galaxies in the simulation, one approach is to use hydrodynamical simulations which are computationally expensive and time consuming. A faster approach is to utilize Semi-analytic models (SAMs). SAMs combine simple analytical prescriptions to describe processes governing galaxy formation with the merger trees obtained numerically from N-body simulations. Therefore, SAMs still benefit from the high resolution and large cosmological volume of the dark matter simulations. Comparing SAMs results with observations therefore offers an opportunity to connect the observed properties of galaxies to the physical processes leading to those properties.

In this thesis, we use synthetic data available from the Millennium Simulation in combination with

SAMs to make predictions of GGL and G3L. By comparing the model predictions with observational measurements of GGL and G3L in the Canada-France-Hawaii Telescope Lensing Survey (CFHTLenS), we can obtain information on the galaxy properties and constraint SAMs.

This thesis is organized as follows:

- In chapter 2, we first summarize the framework of the cosmological model we use to describe the Universe. We describe the early phases of the Universe and the formation and evolution of structures in the linear regime and non-linear regime. Afterwards we present the important aspects of the cosmological dark matter simulations relevant for this thesis. In addition, we show how SAMs use the outcome of simulation to obtain information on the properties of galaxies populating dark matter halos. The SAMs used in this thesis are described afterwards.

- We review in chapter 3 the basic concepts of gravitational lensing while focusing on GGL and G3L. We derive the relevant relations and the estimators for the second- and third-order galaxy-matter correlation functions. The chapter ends with a brief summary on how we can extract lensing information from the cosmological simulations using the ray-tracing algorithm.

- In chapter 4, we present a method to obtain predictions of GGL and G3L using SAMs. We use various galaxy populations with color and magnitude selections to make a comparison between the models.

- Chapter 5 contains the analysis of galaxy-galaxy(-galaxy) lensing correlation functions predicted using SAMs and compared to the measurements of CFHTLenS for galaxies in different redshift and stellar mass bins. We report on the method we use to select model galaxies according the observed properties of galaxies. We investigate the differences between the model predictions and observational measurements to obtain insight on the properties of model galaxies. We further quantify these differences by applying a χ^2 test.

- In chapter 6, we introduce the concept of excess mass map in order to visualize the matter density profile around foreground galaxy pairs with fixed separation. We lay out the mathematical framework around the excess mass map and its relation to the three-point correlation function. We introduce the estimators we use to make predictions of the excess mass map using different SAMs. The predictions are then compared to the measurements of CFHTLenS.

- We summarize and conclude in chapter 7.

CHAPTER 2

Cosmology

From the beginning of times, humans have looked up at the sky and tried to find their place in the Universe. One of the first concepts of the Universe was developed during the Ancient Greece by the mathematician and philosopher Pythagoras. He believed in an ordered Universe which he called "cosmos". Literally, cosmology is thus the study of the creation, the evolution, and the fate of the Universe. Here, we focus on a strictly physical study of the Universe, study that is based on science (physics, astrophysics, mathematics) and relies on complementary approaches (observations, theory, simulations).

Thanks to recent improvements in our observational techniques and computational capabilities, we have been able to gather large and accurate information about the Universe. Consequently, scientists built a theoretical model whose goal was to explain the past, present and future of the Universe. This model is called *the standard model of cosmology* and its validity have been proven by various observations, such as the distribution of galaxies in the sky.

In this Chapter we provide a brief overview of the standard model and present geometrical and dynamical properties of the Universe. We also provide a description of formation and evolution of the structure in the Universe from very early times until today. More details can be found in, e.g., Dodelson (2003), Peacock (1999) or Schneider (2009a).

2.1 The standard cosmological model

The standard model of cosmology predicts that the baryonic matter component (stars, gas) represents only a small fraction ($\sim$ 5%) of the total content of the Universe. A bigger contribution ($\sim$ 25%) comes from the so-called *dark matter*, a matter component that interacts only gravitationally and is therefore not directly visible. The largest contribution ($\sim$ 70%) comes from the dark energy that drives the accelerated expansion of our Universe.

The standard model of cosmology describes a model of the Universe we live in based on the *cosmological principle* which is supported by observational measurements such as galaxy distribution and Cosmic Microwave Background (CMB) experiments. The cosmological principle states that our Universe is on average isotropic and homogeneous over large angular scales for *fundamental observers*. This implies that fundamental observers, comoving with the cosmic flow, observe the same history and evolution of the Universe since there is no preferred position or direction in this flow. The geometry of space-time in such systems is specified by a metric formulated in the framework of general relativity (GR). In GR the effects of gravity are incorporated in changes in the geometry of the Universe which is a

four-dimensional manifold representing space-time. The relation between the geometry and the energy and momentum of space-time are described through sets of equations know as Einstein field equations.

Applying the isotropy and homogeneity of the Universe, the metric known as Robertson-Walker (RW) metric can be written as

$$\mathrm{d}s^2 = \mathrm{c}^2\mathrm{d}t^2 - a^2(t)\left[\mathrm{d}\chi^2 + f_\mathrm{K}^2(\chi)\left(\mathrm{d}\theta^2 + \sin^2\theta\,\mathrm{d}\varphi^2\right)\right], \tag{2.1}$$

where c is the speed of light. The spatial coordinates (χ, θ, φ) are specified by comoving radial distance χ and angular coordinates θ and φ on a unit sphere. $a(t)$ is the *scale factor* characterizing the dynamics of the Universe. The function $f_\mathrm{K}(\chi)$ is the *comoving angular diameter distance*; it depends on the curvature of the Universe and is given by

$$f_\mathrm{K}(\chi) = \begin{cases} K^{-1/2}\sin(K^{1/2}\chi) & (K>0) \\ \chi & (K=0) \\ (-K)^{-1/2}\sinh((-K)^{1/2}\chi) & (K<0) \end{cases},$$

where K is the curvature constant. Solving the Einstein field equation using the RW metric yields the equations of motion for a perfect fluid with pressure P and density ρ,

$$\left(\frac{\dot{a}}{a}\right)^2 = \frac{8\pi G}{3}\rho - \frac{Kc^2}{a^2} + \frac{\Lambda}{3}, \tag{2.2}$$

$$\frac{\ddot{a}}{a} = -\frac{4}{3}\pi G\left(\rho + \frac{3P}{c^2}\right) + \frac{\Lambda}{3}, \tag{2.3}$$

where G is the gravitational constant and Λ denotes the cosmological constant. These equations govern the dynamics of the Universe and are called the *Friedmann equations*. Coupled with the RW metric, they form the Friedmann-Lemaitre-Robertson-Walker (FLRW) model. We now investigate each component contributing to these equations.

The scale factor relates the comoving coordinates, χ, to the physical coordinates, r, through

$$\boldsymbol{r}(t) = a(t)\boldsymbol{\chi}\,. \tag{2.4}$$

The scale factor is dimensionless and depends on the cosmic time. It is normalized so that for today, t_0, $a(t_0) = 1$. The expansion velocity in this coordinate system is

$$\boldsymbol{v}(\boldsymbol{r}, t) = \frac{\mathrm{d}}{\mathrm{d}t}\boldsymbol{r}(t) = \dot{a}\boldsymbol{\chi} = \frac{\dot{a}}{a}\boldsymbol{r}(t) \equiv H(t)\boldsymbol{r}(t) \tag{2.5}$$

with the expansion rate $H(t) \equiv \dot{a}/a$. For the local Universe at present ($t = t_0$), Eq. (2.5) simplifies to

$$\boldsymbol{v} = H_0\boldsymbol{r}\,, \tag{2.6}$$

known as the Hubble law with H_0 denoting the Hubble constant. Edwin Hubble discovered in 1928 that galaxies are receding from us with a velocity $\boldsymbol{v}$ which is on average proportional to their distance (this is interpreted as the expansion of the Universe). The constant of proportionality, the Hubble constant, H_0, has the units of inverse time and is parametrized as $H_0 = 100\,h\,\mathrm{km\,s^{-1}Mpc^{-1}}$ with h being a dimensionless constant, the Hubble parameter. The Hubble parameter is inserted to take into account the uncertainties in distance measurements. Since objects are moving away from us, from Eq. (2.6) we have $H_0 > 0$, and consequently $\dot{a}_0 > 0$. Therefore, the Universe is expanding at the present epoch.

According to the standard cosmological model, the Universe consists of three main matter and energy

components: radiation, pressureless matter, and dark energy. These components follow

$$\frac{\mathrm{d}(\mathrm{c}^2\rho a^3)}{\mathrm{d}t} = -P\frac{\mathrm{d}(a^3)}{\mathrm{d}t}\,, \tag{2.7}$$

from which we can find how the density changes over time. Eq. (2.7) states that the change in the energy contained in a system of fixed comoving volume equals the work done by the system (i.e. pressure times the change in that volume).

Radiation includes all the relativistic particles such as photons and neutrinos for which the pressure changes as $P_\mathrm{r} = \rho_\mathrm{r}\mathrm{c}^2/3$. Using Eq. (2.7) then yields $\rho_\mathrm{r} = \rho_{\mathrm{r}0}a^{-4}$ where $\rho_{\mathrm{r}0}$ is the current radiation density. The matter component includes non-relativistic particles (dark matter and baryonic matter), for which $P_\mathrm{m} = 0$ yielding $\rho_\mathrm{m} = \rho_{\mathrm{m}0}a^{-3}$. The third main component is the dark energy which is usually interpreted as a constant vacuum energy with an equation of state, $P_\Lambda = -\rho_\Lambda c^2$ and with the density related to the cosmological constant via $\rho_\Lambda = \frac{\Lambda}{8\pi G}$. Consequently, the total density and pressure in the Universe is:

$$\rho = \rho_\mathrm{r} + \rho_\mathrm{m} + \rho_\Lambda = \frac{\rho_{\mathrm{r}0}}{a^4} + \frac{\rho_{\mathrm{m}0}}{a^3} + \rho_\Lambda, \tag{2.8}$$

$$P = \frac{\rho_\mathrm{r}c^2}{3} - \rho_\Lambda c^2 = \frac{\rho_{\mathrm{r}0}c^2}{3a^4} - \rho_\Lambda c^2. \tag{2.9}$$

Solving Eq. (2.2) for the simple case of a flat geometry of the Universe, i.e. $K = 0$ and obtain the *critical density*:

$$\rho(t) = \frac{3H^2(t)}{8\pi G} \equiv \rho_\mathrm{cr}(t)\,. \tag{2.10}$$

For today ($t = t_0$), the critical density is:

$$\rho_\mathrm{cr} := \frac{3H_0^2}{8\pi G} = 1.88\times10^{-29}h^2\mathrm{g/cm}^3\,. \tag{2.11}$$

Using this definition, we can define the dimensionless density parameters for various components:

$$\Omega_\mathrm{m} := \frac{\rho_{\mathrm{m}0}}{\rho_\mathrm{cr}}; \qquad \Omega_\mathrm{r} := \frac{\rho_{\mathrm{r}0}}{\rho_\mathrm{cr}}; \qquad \Omega_\Lambda := \frac{\rho_\Lambda}{\rho_\mathrm{cr}}. \tag{2.12}$$

The baryon density parameter Ω_b can be defined similarly. The total density parameter is defined as $\Omega_0(t) = \sum_i \Omega_i(t)$. From Eq. (2.2), we see that

$$K = \left(\frac{H_0}{\mathrm{c}}\right)^2(\Omega_0 - 1)\,. \tag{2.13}$$

In the case of $K > 0$, the Universe is called *closed* while $K < 0$ belongs to a universe called *open*. We define the Hubble radius as the characteristic length-scale of the Universe,

$$R_H := \frac{\mathrm{c}}{H_0} = 2998h^{-1}\mathrm{Mpc}\,. \tag{2.14}$$

Finally, the Friedmann equation (Eq. 2.2) can be rearranged to find the expansion equation

$$\left(\frac{\dot{a}}{a}\right)^2 = H^2(t) = H_0^2\left[\frac{\Omega_\mathrm{r}}{a^4} + \frac{\Omega_\mathrm{m}}{a^3} + \frac{1-\Omega_0}{a^2} + \Omega_\Lambda\right], \tag{2.15}$$

which indicates that different components of the Universe change differently with the scale factor. For

very small a, the radiation is dominant and for larger a matter, the curvature term and cosmological constant (if non-zero) dominate, respectively. It can be immediately concluded that in an expanding universe the radiation was dominating the Universe at early times and afterwards the pressure-less matter started to be dominant. The transition between the two epochs occurs when these two components have equal energy density corresponding to a scale factor of,

$$a_{\mathrm{eq}} = \frac{\Omega_{\mathrm{r}}}{\Omega_{\mathrm{m}}} = 4.2 \times 10^{-5} \Omega_{\mathrm{m}}^{-1} h^{-2} \,. \tag{2.16}$$

The fate of the Universe then depends on the matter and vacuum energy densities. The constraints on the value of these parameters is obtained from cosmological probes such as Cosmic Microwave Background (CMB) observations. The classification of the model for different density parameters leads to the following conclusions:

- The Universe must have originated from a dense and hot singularity point called the "Bing Bang" with $a = 0$. The age of the Universe then means the time passed since the big bang.
- The Universe was expanding in the past for all $a \leqslant 1$.
- Spatially flat universes (like ours), for which $\Omega_{\mathrm{m}} + \Omega_{\Lambda} = 1$, expand at all time and for all a if $\Omega_{\mathrm{m}} \leqslant 1$ (i.e. $\Omega_{\Lambda} \geqslant 0$).

Redshift

One of the consequences of an expanding universe is the shift in the observed spectrum of cosmic objects towards higher wavelengths. This "redshift" can then be written the form of

$$z := \frac{\lambda_{\mathrm{obs}} - \lambda_{\mathrm{e}}}{\lambda_{\mathrm{e}}} \,, \tag{2.17}$$

where λ_{obs} and λ_{e} denote the observed and the rest frame wavelength of light emitted from a source at comoving distance χ. Light rays travel through null geodesics, $\mathrm{d}s^2 = 0$, therefore the comoving radial distance of the source can be related to cosmic time through,

$$\mathrm{c}\,\mathrm{d}t = -a(t)\,\mathrm{d}\chi \quad \Longrightarrow \quad \chi(t) = \int_t^{t_{\mathrm{obs}}} \frac{c\,\mathrm{d}t'}{a(t')} \,. \tag{2.18}$$

If the source emits two light rays at t_{e} and $t_{\mathrm{e}} + \mathrm{d}t_{\mathrm{e}}$ which reach the observer at t_{obs} and $t_{\mathrm{obs}} + \mathrm{d}t_{\mathrm{obs}}$, due to the expansion of the Universe one obtains $\mathrm{d}t_{\mathrm{e}} = a(t)\mathrm{d}t_{\mathrm{obs}}$ or in terms of frequency $\nu_{\mathrm{e}} = \frac{\nu_{\mathrm{obs}}}{a(t)}$. Therefore, the relation between the redshift and the scale factor is:

$$1 + z := \frac{\lambda_{\mathrm{obs}}}{\lambda_{\mathrm{e}}} = \frac{\nu_{\mathrm{e}}}{\nu_{\mathrm{obs}}} = \frac{1}{a(t)} \,. \tag{2.19}$$

It should be noted that if the scale factor is a monotonic function of time for all $a \in [0, 1]$, then z is also monotonic, meaning that a source with higher redshift is more distant from us than a source with lower redshift.

Angular diameter distance

There are different ways of measuring distances in cosmology. Unlike Euclidean space, distance measures using different methods in a curved space-time do not lead to the same results. One of the most

commonly used method is the angular diameter distance.

For a source with physical diameter ds and enclosing an angle dθ, the angular diameter distance is defined as

$$D_A = \frac{\mathrm{d}s}{\mathrm{d}\theta} = a(t) f_{\mathrm{K}}(\chi)\,, \tag{2.20}$$

where the last equality follows from the metric (Eq. 2.1).

The horizon

Due to the finite speed of light, at present we are only able to observe part of the Universe that corresponds to the distance light has travelled from the big bang to us. This observational limit is called the *horizon* which increases with time. Since for the light, $\mathrm{c}\,\mathrm{d}t = -a(t)\,\mathrm{d}\chi$, the comoving horizon size can be calculated as

$$r_{\mathrm{H}} = \int_0^t \frac{\mathrm{c}\,\mathrm{d}t}{a(t)} = \int_0^a \frac{\mathrm{c}\,\mathrm{d}a}{a^2 H(a)}\,. \tag{2.21}$$

Thermal history of the Universe

Another consequence of an expanding universe is that distribution of particles and their chemical equilibrium conditions changes over time. In models with a big bang, the Universe was hotter in the past, $T \propto (1+z)$. At temperature of $\sim$ 100MeV, baryons (proton and neutron), electrons, positrons, photons and neutrinos are in chemical equilibrium. Equilibrium here means that their production and annihilation rate is equal. About one second after the big bang, at lower temperatures ($\sim$ 1.4MeV), neutrinos can no longer stay in equilibrium and propagate without interacting with other particles. When then Universe cools down to temperatures of $\sim$ 0.7MeV, protons and neutrons leave the equilibrium state and at even lower temperature ($\sim$ 0.5MeV), the production of electron-positron pairs is not efficient anymore and the pair annihilation happens efficiently which injects energy to photons. The particles out of equilibrium, namely neutrinos, do not benefit from this excess of energy. Three minutes after the big bang, at $T \sim 0.1$MeV, atomic nuclei, namely deuterium, form by fusion of protons and neutrons and once the abundance of deuterium is sufficient, helium nuclei ^{4}He form. The big bang nucleosynthesis predicts that ^{4}He constitutes 1/4 of the total baryonic mass of the Universe, a result in excellent agreement with the observations.

After further cooling of the Universe, free electrons recombine with the atomic nuclei to form neutral atoms. This "recombination" is in competition with ionization of atoms by energetic photons and only when the abundance of neutral atoms is increased enough so that the number of free electron is decreased, the photons can propagate freely without further interaction with matter. Therefore, 400 000 years after the big bang and at the redshift of $z \sim 1100$, "the last-scattering surface", photons decoupled from matter and the Universe became neutral and photons travelled to us freely. These photons have a blackbody spectrum with the temperature that decreases as $T \propto (1+z)$ and frequencies shifted to microwave regime due to the expansion of the Universe. The presence of this *cosmic microwave background* (CMB) radiation has been observationally verified.

2.2 Structure formation

The origin of the structures

In the framework of the standard model, the structures we observe today such as galaxies and clusters of galaxies are results of the growth of very small fluctuations in the matter density field. A favoured model that describes the origin of these fluctuations is the "inflation". According to standard inflationary models, initial quantum fluctuations existed at early times which were exponentially expanded during an inflationary phase which ended at $t \sim 10^{-32}$s after the big bang. Afterwards the fluctuations in the density field grew through gravitational instability: regions denser than the environment expanded slower than the expansion flow of the Universe leading to even higher densities in those regions.

Structure growth

The evolution of structures after inflation depends on the size of the fluctuations. At early times, density fluctuations are comparable to or larger than the horizon size and therefore the properties of density field have to be studied within the framework of General Relativity. At later times, with the expansion of the Universe these perturbations "enter" the horizon and hence they have a smaller size than the horizon. In this regime, the structure growth can be explained by linear Newtonian physics. Finally, the perturbations grow large enough that a linear theory is not valid anymore and the analytical approach has to be replaced by a numerical approach. In this regime, the statistical properties of the density fluctuation is formulated using N-body simulations.

Newtonian theory of gravity

As long as density fluctuations are small, i.e. the density contrast $\frac{\Delta\rho}{\bar{\rho}} \ll 1$, and much smaller than horizon size in the matter-dominated era, the fluid approximation can be applied. The fluid equations are:

$$\frac{\partial\rho(\boldsymbol{r},t)}{\partial t} + \nabla_r \cdot [\rho \boldsymbol{u}(\boldsymbol{r},t)] = 0 \qquad \text{Continuity Eq.}\,, \tag{2.22}$$

$$\frac{\partial \boldsymbol{u}(\boldsymbol{r},t)}{\partial t} + (\boldsymbol{u}(\boldsymbol{r},t)\cdot\nabla_r)\boldsymbol{u}(\boldsymbol{r},t) = -\nabla_r\phi(\boldsymbol{r},t) \qquad \text{Euler Eq.}\,, \tag{2.23}$$

$$\nabla_r^2\phi(\boldsymbol{r},t) = 4\pi G\rho(\boldsymbol{r},t) - \Lambda \qquad \text{Poisson Eq.}\,, \tag{2.24}$$

where the matter density ρ, the velocity field $\boldsymbol{u}$ and the gravitational potential ϕ of the pressureless matter are used. These quantities can be written in the comoving coordinates,

$$\boldsymbol{\chi} = \frac{\boldsymbol{r}}{a(t)}\,, \tag{2.25}$$

$$\rho(\boldsymbol{r},t) = \hat{\rho}\left(\frac{\boldsymbol{r}}{a(t)},t\right) = \hat{\rho}\left(\boldsymbol{\chi},t\right)\,, \tag{2.26}$$

$$\boldsymbol{u}(\boldsymbol{r},t) = \frac{\dot{a}(t)}{a(t)}\boldsymbol{r} + \boldsymbol{v}\left(\frac{\boldsymbol{r}}{a(t)},t\right)\,, \tag{2.27}$$

$$\Phi(\boldsymbol{\chi},t) = \phi(a(t)\boldsymbol{\chi},t) + \frac{\ddot{a}a}{2}|\boldsymbol{\chi}|^2\,. \tag{2.28}$$

In Eq. (2.27), the velocity field was decomposed into two components, namely the Hubble flow and peculiar velocity which describes the deviation of the velocity field from the homogeneous expansion. Another quantity related to the deviation from a homogeneous field is the density contrast defined as:

$$\delta(\boldsymbol{\chi}, t) = \frac{\hat{\rho}(\boldsymbol{\chi}, t) - \bar{\rho}}{\bar{\rho}}\,, \tag{2.29}$$

where $\bar{\rho}$ is the mean number density. Eventually Eqs. (2.22)-(2.24) can be written in the comoving coordinates,

$$\frac{\partial \delta}{\partial t} + \frac{1}{a}\nabla_{\chi} \cdot [(1+\delta)\boldsymbol{v}] = 0\,, \tag{2.30}$$

$$\frac{\partial \boldsymbol{v}}{\partial t} + \frac{\dot{a}}{a}\boldsymbol{v} + \frac{1}{a}(\boldsymbol{v} \cdot \nabla_{\chi})\boldsymbol{v} = -\frac{1}{a}\nabla_{\chi}\Phi\,, \tag{2.31}$$

$$\nabla^2_{\chi}\Phi = \frac{3H_0^2\Omega_m^2}{2a}\delta\,. \tag{2.32}$$

Considering small-scale perturbations, $\delta \ll 1$, all orders higher than linear in δ and $\boldsymbol{v}$ can be neglected. The Poisson equation, Eq. (2.32), remains unchanged, however, the continuity and the Euler equations can be linearised to:

$$\frac{\partial \delta}{\partial t} + \frac{1}{a}\nabla_{\chi} \cdot \boldsymbol{v} = 0\,, \tag{2.33}$$

$$\frac{\partial \boldsymbol{v}}{\partial t} + \frac{\dot{a}}{a}\boldsymbol{v} = -\frac{1}{a}\nabla_{\chi}\Phi\,. \tag{2.34}$$

Taking the time derivative of Eq. (2.33),

$$\frac{\partial}{\partial t}\left[\frac{\partial \delta}{\partial t} + \frac{1}{a}\nabla_{\chi} \cdot \boldsymbol{v}\right] = 0\,, \tag{2.35}$$

and the divergence of Eq. (2.34),

$$\frac{\nabla}{a} \cdot \left[\frac{\partial \boldsymbol{v}}{\partial t} + \frac{\dot{a}}{a}\boldsymbol{v} = -\frac{1}{a}\nabla_{\chi}\Phi\right]\,, \tag{2.36}$$

and combining the results with the Poisson equation (Eq. 2.32), one obtains

$$\frac{\partial^2 \delta}{\partial t^2} + \frac{2\dot{a}}{a}\frac{\partial \delta}{\partial t} - \frac{3H_0^2\Omega_m^2}{2a^3}\delta = 0\,, \tag{2.37}$$

with a general solution of the form:

$$\delta(\boldsymbol{\chi}, t) = D_+(t)\Delta_+(\boldsymbol{\chi}) + D_-(t)\Delta_-(\boldsymbol{\chi})\,. \tag{2.38}$$

This implies that the shape of density fluctuations does not change in comoving coordinates and only their amplitude increases in the linear regime. $D_+(t)$ is an increasing function of cosmic time whereas $D_-(t)$ term decreases over time and will die out quickly, therefore has no contribution to the structure growth. It can be shown that one solution of Eq. (2.37) is the Hubble function $H(t) = \dot{a}/a$. However, since the Hubble function is a decreasing function of time, therefore $H(t) = D_-(t)$. The other solution,

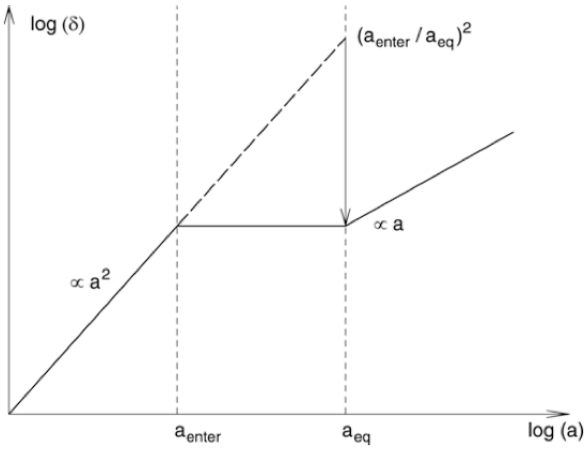

Figure 2.1: Sketch of the evolution of density perturbations with the scale factor. A perturbation that enters the horizon in the radiation dominated era ceases to grow until the universe is dominated by dark matter. Its growth is suppressed by $\left(a_{\rm enter}/a_{\rm eq}\right)^2$ compared to the perturbation that enters the horizon in the matter-dominated era. Figure adopted from Bartelmann & Schneider (2001).

called "the growth factor", can be expressed through the first as:

$$D_+(t) \propto H(t)H_0^2 \int_0^t \frac{{\rm d}t'}{a^2(t')H^2(t')}\,, \tag{2.39}$$

where the constant of proportionality can be fixed by normalising the growth factor to unity for present time. The growth of structure depends on the cosmological epoch through Eq. (2.39) which depends on density parameters through the Hubble function.

Relation to horizon scale

As mentioned above, the growth of structures changes during the expansion of the Universe in radiation- and matter-dominated epochs. It also depends on the scale of fluctuation relative to the comoving horizon size at the epoch considered. The horizon scale grows with a, therefore for any perturbation there exits a time when the scale of the perturbation equals the comoving horizon scale. This time is marked by $a_{\rm enter}$ in Fig. 2.1 denoting the time when the perturbation is said to "enter" the horizon.

For a perturbation in the radiation-dominated era the density contrast varies as $\delta \propto a^2$. If this perturbation enters the horizon at the matter-radiation equality time, $a_{\rm enter} = a_{\rm eq}$, or in the matter-dominated era, the density grows as $\delta \propto a$. However, if it enters the horizon in the radiation-dominated epoch, the density fluctuation is suppressed relative to a fluctuation that enters the horizon after matter-radiation equality, by a factor of $\left(a_{\rm enter}/a_{\rm eq}\right)^2$. The density contrast then remain unchanged until dark matter starts to dominate the density of the Universe. Afterwards it grows as $\delta \propto a$. Before recombination, baryons and photons are coupled via Thomson scattering as they enter the horizon and due to pressure force they oscillate. After recombination epoch, the radiation continues to oscillate, whereas baryons fall into the potential well of dark matter and therefore evolution of baryon perturbation follows that of dark matter.

2.2.1 Statistical properties of the structures

So far, we have focused on the evolutionary behaviour of density perturbations in the course of cosmic time. What we are actually interested in is to understand the exact density field that we observe today given a specific initial condition. However, there is no theory of structure formation that can exactly predict δ at early times. The inflationary models can provide only the statistical properties of the initial density field. We can only observe our Universe and it can be thought to be a particular realization of an ensemble of random field. All realizations of a random field share the same statistical properties, however they are picked randomly from a probability distribution. If a realization is described by a set of $\delta(\chi)$ functions, then a random field is specified by the probability of occurrence of a specific realization.

Correlation Function and Power Spectrum

Here we explore the statistical properties of the random field that our Universe belongs to. The statistical properties of a random field can be characterized by its moments. The first order moment is the mean which from the definition of δ one can see that $\langle\delta\rangle = 0$ where $\langle . \rangle$ denotes the ensemble average, which is the average over many realizations of δ. The second-order moment is called the two-point correlation function (2PCF) and is defined as:

$$\left\langle \delta(\boldsymbol{x})\delta^*(\boldsymbol{y})\right\rangle = \xi_{\delta\delta}(|\boldsymbol{x}-\boldsymbol{y}|)\,, \tag{2.40}$$

where δ^* denotes the complex conjugate of δ. It should be noted that since δ inhabits an isotropic and homogenous universe (on large-scale), the statistical properties of δ should also be isotropic and homogenous. Therefore the correlation function is a function of the separation between the two points $|\boldsymbol{x}-\boldsymbol{y}|$ only and not the direction of the separation vector.

The Fourier transform of δ can then be defined as

$$\tilde{\delta}(\boldsymbol{k}) = \int \mathrm{d}^3x\ \delta(\boldsymbol{x})\,\mathrm{e}^{-\mathrm{i}\boldsymbol{x}\cdot\boldsymbol{k}}\,. \tag{2.41}$$

The Fourier transform of the correlation function is then given by

$$\begin{aligned}\left\langle \tilde{\delta}(\boldsymbol{k})\tilde{\delta}^*(\boldsymbol{k'})\right\rangle &= (2\pi)^3\,\delta_{\mathrm{D}}(\boldsymbol{k}-\boldsymbol{k'})\int \mathrm{d}^3y\ \mathrm{e}^{\mathrm{i}\boldsymbol{y}\cdot\boldsymbol{k}}\,\xi_{\delta\delta}(|\boldsymbol{y}|)\\ &= (2\pi)^3\,\delta_{\mathrm{D}}(\boldsymbol{k}-\boldsymbol{k'})P_{\delta\delta}(|\boldsymbol{k}|)\,,\end{aligned} \tag{2.42}$$

where the power spectrum $P_\delta(|\boldsymbol{k}|)$ is defined as the Fourier transform of the two point correlation function $\xi_{gg}(|\boldsymbol{y}|)$. Roughly speaking, power spectrum specifies the amplitude of the density fluctuations at a given length scale $2\pi/k$ with k being the comoving wavenumber.

Standard inflationary models predict the initial density field as a Gaussian random field, i.e. the initial density fluctuations $\delta(\chi)$ have a Gaussian probability distribution. Inflation also predicts that at early times, t_i, when the density fluctuations are larger than horizon scale, the initial power spectrum is well characterized by a power law, $P(k,t_i) = A\,k^{n_s}$, with the spectral index $n_s \approx 1$ and A is a normalization constant that has to be determined observationally. The evolution of power spectrum over the cosmic time in the linear regime can be written as

$$P(k,t) = A\,k^{n_s}\,T_k^2\,D_+^2(t)\,. \tag{2.43}$$

The dependence on D_+^2 is due to the growth of perturbation with the growth factor. T_k is the transfer

function which accounts for the scale-dependence of structure growth.

Transfer function

As discussed, the evolution of density fluctuations is affected strongly by their length-scale as can be seen for example by suppression of growth during the radiation-dominated era (Fig. 2.1). The nature of dark matter also affects the structure growth, depending on if dark matter consists of cold dark matter (CDM) or hot dark matter (HDM) particles. The HDM particles have large velocities (and thus high pressure) which prevents them from falling into the gravitational potential wells and form matter concentrations unless for the strongest potential wells. It should be noted then if dark matter was entirely composed of HDM particles, only large scale density perturbations could form, a scenario which is rejected by observations.

To account for these effects, one considers the ratio of the amplitude of a perturbation with a wavenumber k to a perturbation of wavenumber k_s that enters the horizon at late times (in the matter-dominated era, well after $a_{\rm eq}$). The transfer function is defined through

$$\frac{\tilde{\delta}(k, t_0)}{\tilde{\delta}(k_s, t_0)} = T_k \frac{\tilde{\delta}(k, t_i)}{\tilde{\delta}(k_s, t_i)} \,. \tag{2.44}$$

where $\tilde{\delta}(k, t_i)$ is the amplitude of the fluctuations at early times, and $\tilde{\delta}(k, t_0)$ is that of today. For CDM, the behavior of transfer function is found to be

$$T_k \approx \begin{cases} 1 & \text{for } k \ll 1/r_{\rm H}(a_{\rm eq}) \\ (k r_{\rm H}(a_{\rm eq}))^{-2} & \text{for } k \gg 1/r_{\rm H}(a_{\rm eq}) \end{cases} \tag{2.45}$$

where $r_{\rm H}(a_{\rm eq}) \approx 16(\Omega_{\rm m} h)^{-2}$ Mpc is the comoving horizon size at the epoch of matter-radiation equality.

Normalization of the power spectrum

The normalization of the power spectrum is commonly parametrized in terms of σ_8, the dispersion of density fluctuations in a sphere of radius $8h^{-1}$ Mpc. It has been shown that observing galaxies in spheres of radius $8h^{-1}$ Mpc in the local Universe, the fluctuation amplitude of the galaxy density field is of the order of unity. If galaxies trace the underlying matter distribution then $\sigma_8 \approx 1$ which roughly specifies the scale for which the density become non-linear today.

2.2.2 Non-linear evolution

The assumptions we made in above statements are valid as long as the density contrast is considerably smaller than unity. When the density contrast approaches unity, $\delta \approx 1$, one can either utilize higher-order perturbation theories or use simplified model of structure formation and growth, namely the *halo model* in which all the matter content of the Universe is concentrated in self gravitationally bound objects called halos. Another more widely used method is *numerical simulations* which has proven to provide a rather accurate picture of the structure formation well into the non-linear regime. In the following we summarize some aspects of these simulations.

2.3 Cosmological N-body simulations

Developments in the computational capabilities have enabled us to use numerical methods to make simulation of our Universe. Numerical simulations present a novel approach to understand the non-linear evolution of the structure in the Universe. One popular technique is to use a set of particles to represent the distribution of matter. Numerical investigations of such N-body systems started in 1960s with low number of particles. For example, Peebles (1970) carried out simulations of the Coma Cluster of galaxies using 300 particles.

Considering that dark matter in the Universe is the dominant mass component, simulations use a set of collisionless particles representing dark matter that interact only gravitationally. This N-body system then approximates the dark matter distribution and its accuracy increases by increasing the number of particles. However, simulating large number of particles in large volumes means an increase in computational costs. Therefore, one has to find a compromise between sufficient resolution and reasonable computational resources.

For the simulation to be able to link the initial conditions of the structure formation to the one observed at present time, the simulation has to be large enough to include the large scale structure and still be able to resolve objects at small scales such as halos of galaxies.

In the following, we describe the basic principles of N-body simulations, from generating the initial conditions to modelling the evolution of dark matter particles.

2.3.1 Numerics and initial conditions

Dark matter particles interact only gravitationally, i.e. the force exerted on the i-th particle is:

$$\boldsymbol{F}_i = G \sum_{j \neq i}^{N} \frac{M_i M_j (\boldsymbol{r}_j - \boldsymbol{r}_i)}{|\boldsymbol{r}_j - \boldsymbol{r}_i|^3}\,, \tag{2.46}$$

where N is the total number of particles, G is the gravitational constant, M_i is the mass of i-th particle and $|\boldsymbol{r}_j - \boldsymbol{r}_i|$ is the distance between particles i and j.

As can be seen from Eq. (2.46), if there are N particles in the simulation, N^2 operations are required. Large number of particles considered in simulations makes it computationally expensive. Alternatively, one uses so-called particle-mesh (PM) algorithm (Hockney & Eastwood 1988) in which particles are deposited onto a regular mesh (hence the name "particle-mesh") where the number of cells is of the same order of the number of particles. Thus, we can use Fast Fourier Transform, which only requires $N \log N$ operations to calculate the gravitational field. The computational achievement comes with a price and that is the resolution. Assigning a grid limits the spatial resolution to a few grid cells over which the force field is smoothed out. This problem is solved by assuming that the gravitational potential of a particle can be divided to short-range and long-range components. The long-range component is computed using the PM algorithm since the resolution effect does not pose a problem when the separation of particle pairs is larger than the scale dividing the long- and short-range potentials. For shorter separations the resolution effects become important. In this case, the force is thus calculated by direct summation (Eq. 2.46). This is called particle-particle particle-mesh (P^3M) algorithm.

The initial conditions are set in such a way that the distribution of particles at high redshifts resembles that of a Gaussian random field and has the power spectrum that fits the linear power spectrum calculated analytically for the assumed cosmology.

2.3.2 Dark matter halos

As dark matter particles interact, they form self-bound objects called dark matter halos (DM halos). A common tool to identify DM halos is the "Friends-of-Friends" (FoF) algorithm (Davis et al. 1985). FOF links particles together in one halo if their separation is smaller than a linking length.The linking length is chosen in such a way the halo density is 200 times the critical density at the considered redshift. A common chosen linking length is 0.2 of the mean particle separation. Therefore DM halos are defined as collapsed virialized objects with density equal to 200 times the critical density. At each redshift, the virial mass $M_{\rm vir}$, virial radius $R_{\rm vir}$, and the virial velocity $V_{\rm vir}$ (the circular velocity at the the virial radius) of a halo are then related through:

$$M_{\rm vir} = \frac{100}{G} H^2(z) R_{\rm vir}^3 = \frac{V_{\rm vir}^3}{10GH(z)} \,. \tag{2.47}$$

One of the significant results of such N-body simulations is that DM halos show a universal density profile, the "NFW" profile (Navarro, Frenk, & White 1997),

$$\rho(r) = \frac{\rho_s}{(r/r_s)(1 + r/r_s)^2} \,, \tag{2.48}$$

where ρ_s and r_s are parameters determining the amplitude and the power-law behaviour of the density profile, respectively. At the outer part of the halo ($r \gg r_s$) the density steepens as $\rho \propto r^{-3}$ and in the inner regions ($r \ll r_s$) it follows $\rho \propto r^{-1}$. It should be noted that DM halos are generally not spherical however. Therefore the tidal force does not act similarly throughout the halo. Hence DM halos acquire angular momentum. In order for a halo to stay rotationally supported, the angular momentum has to balance with the binding energy of the halo.

DM halos usually contain substructures, subhalos. The FOF algorithm does not recognize subhalos within halos, therefore other algorithms have to be used to find overdensities within specific halos. Resolving halos and their corresponding subhalos at each output time (redshift), simulations are able to trace the merging history of each DM subhalo. These "merger trees" (see Fig. 2.2) are one of the fundamental outcome of DM simulations and are the essential requirement to construct semi-analytical models of galaxy formation.

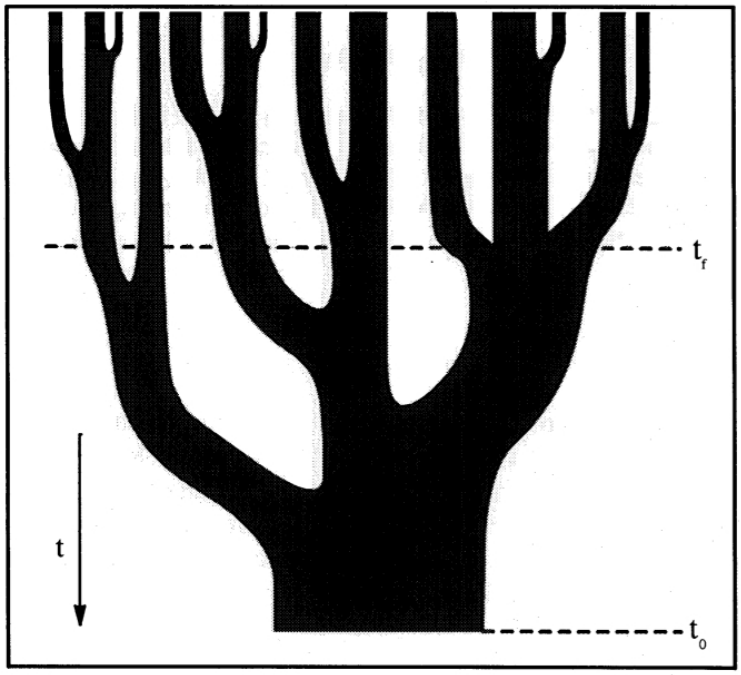

Figure 2.2: Illustration of a typical merger tree showing how a massive halo at present time ($t = t_0$) is built at time t_f by merging subhalos. Time increases from top to bottom. The width of the branches is correlated with the masses of subhalos. Credit: Lacey & Cole (1993a).

In the following we discuss the properties of semi-analytical models after briefly go through the simulations they are implemented on.

2.3.3 Millennium(-II) Simulations

Millennium Simulation (MS, Springel et al. 2005) and MS-II (Boylan-Kolchin et al. 2009) are dark matter N-body simulations tracing the evolution of 2160^3 particles from $z = 127$ (when the initial conditions where set) to the present day. MS was carried out in a cubic region of comoving side length $500h^{-1}$Mpc which is five times bigger than MS-II with $100h^{-1}$Mpc box size; hence, there is a factor of 125 in mass resolution between MS ($1.18\times10^9 M_\odot$) and MS-II ($9.45\times10^6 M_\odot$). Both simulations assume a ΛCDM cosmology with parameters based on 2dFGRS (Colless et al. 2001) and first-year WMAP data (Spergel et al. 2003). These parameters are summarized in Table 2.1. The resulting dark matter density field at present time in MS is shown in Fig. 2.3.

Table 2.1: Cosmological parameters for the assumed cosmology in MS and MS-II and the Planck cosmology (Planck Collaboration et al. 2014).

Parameters	MS & MS-II	Planck
Ω_Λ	0.75	0.685
Ω_b	0.045	0.0487
Ω_m	0.25	0.315
σ_8	0.9	0.829
n_s	1	0.96
$H_0[\mathrm{km\,s^{-1}Mpc^{-1}}]$	73	67.3

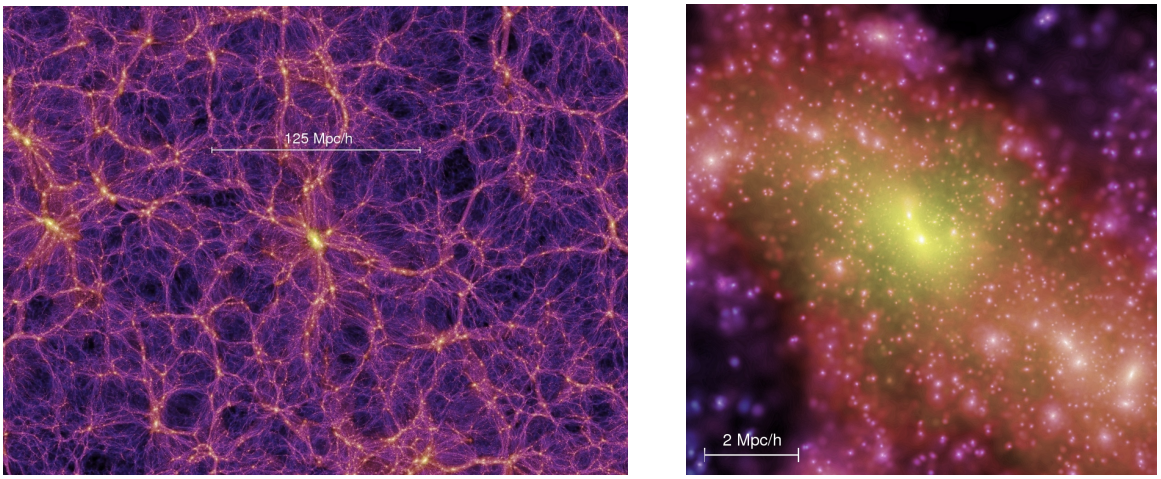

Figure 2.3: The projected dark matter distribution in the Millennium simulation at $z = 0$ both on very large scales (left panel) and for a massive cluster (right panel). Color-coded by the density of DM halos. Credit: http://www.mpa-garching.mpg.de/galform/virgo/millennium

2.4 Semi-analytical models of galaxy formation

Galaxies form in DM halos, however their evolution is not simply the same as that of the DM halo they reside in. To understand physical processes governing the formation and evolution of galaxies one has to take into account the baryonic effects. There are two approaches to deal with this, hydrodynamical simulations and semi-analytical models.

While the computational power has increased considerably in the past years, hydrodynamical simulations are still computationally expensive and time consuming to be carried out. Computationally, it is challenging to simultaneously resolve galaxy-scale structures, include large-scale structures, and take into account the role of baryons. Semi-analytic models (SAMs), on the other hand parametrise complicated baryonic physics with analytical prescriptions and still benefit from the high resolution and large cosmological volume of dark matter N-body simulations. SAMs combine analytical description of processes governing galaxy formation with the merger trees obtained numerically from N-body simulations. Matching SAMs results with observations therefore offer an opportunity to connect the observed properties of galaxies to the physical processes leading to those properties. In the following we give a general and simplified description of SAMs. While most of SAMs agree on these generalities, they differ in some details. We will give examples of such differences in the next section.

The basic idea followed by SAMs is summerized in Fig. 2.4. Generally, SAMs assume a cosmology with specific cosmological parameters and populate DM halos in the N-body simulation by assigning a baryon fraction to each halo at each output time. They follow the formation of disk galaxies by parametrizing the cooling of gas in the halo and the consequent formation of stars. For a review on galaxy formation see Silk et al. (2013). The star formation rate is regulated by feedback processes so that not all the cold gas in the halo will turn to stars. The formation of bulges and ellipticals is then modelled by merging of galaxies or by disk buckling. In order to determine the observable properties of galaxies such as colors and luminosities, SAMs follow the chemical evolution of galaxies through feedback processes, stellar population synthesis models, and dust effects. Taking into account all these considerations, SAMs are able to model the evolution and fate of galaxies undergoing these processes. The free parameters assumed in these models are then adjusted by comparing the output of SAMs with observational data.

Below, we discuss each of the procedures undertaken to account for the physical processes mentioned in Fig. 2.4.

Gas cooling SAMs populate DM halo/subhalos in each merger tree with galaxies. The baryon content of each halo, $f_b = \Omega_b/\Omega_m$, is assumed to be the cosmic mean baryon fraction. This baryonic content is initially in the form of primordial gas (that can later on be enriched) and has the same distribution and angular momentum as the hosting halo. However, baryon interactions in the halo is subject to physical effects such as friction which causes the heating of the gas. In order for stars to form in the halo, this gas has to overcome the pressure due to heating and it has to cool. Gas cooling can be due to radiation processes which help the gas to lose some of its energy in the form of radiation. The cooling rate depends on the density and temperature and the chemical composition of the gas.

Star formation and reionization When the gas cooling is efficient enough, stars can form. The first generation of stars (population III stars) form at high redshifts and in low-mass halos where cooling is provided by molecular hydrogen. The nuclear fusions in stars release energetic photons that ionize the surrounding material. This is the beginning of reionization era. These photons released from population III stars have enough energy to destroy the remaining molecular hydrogen. At lower redshifts and in

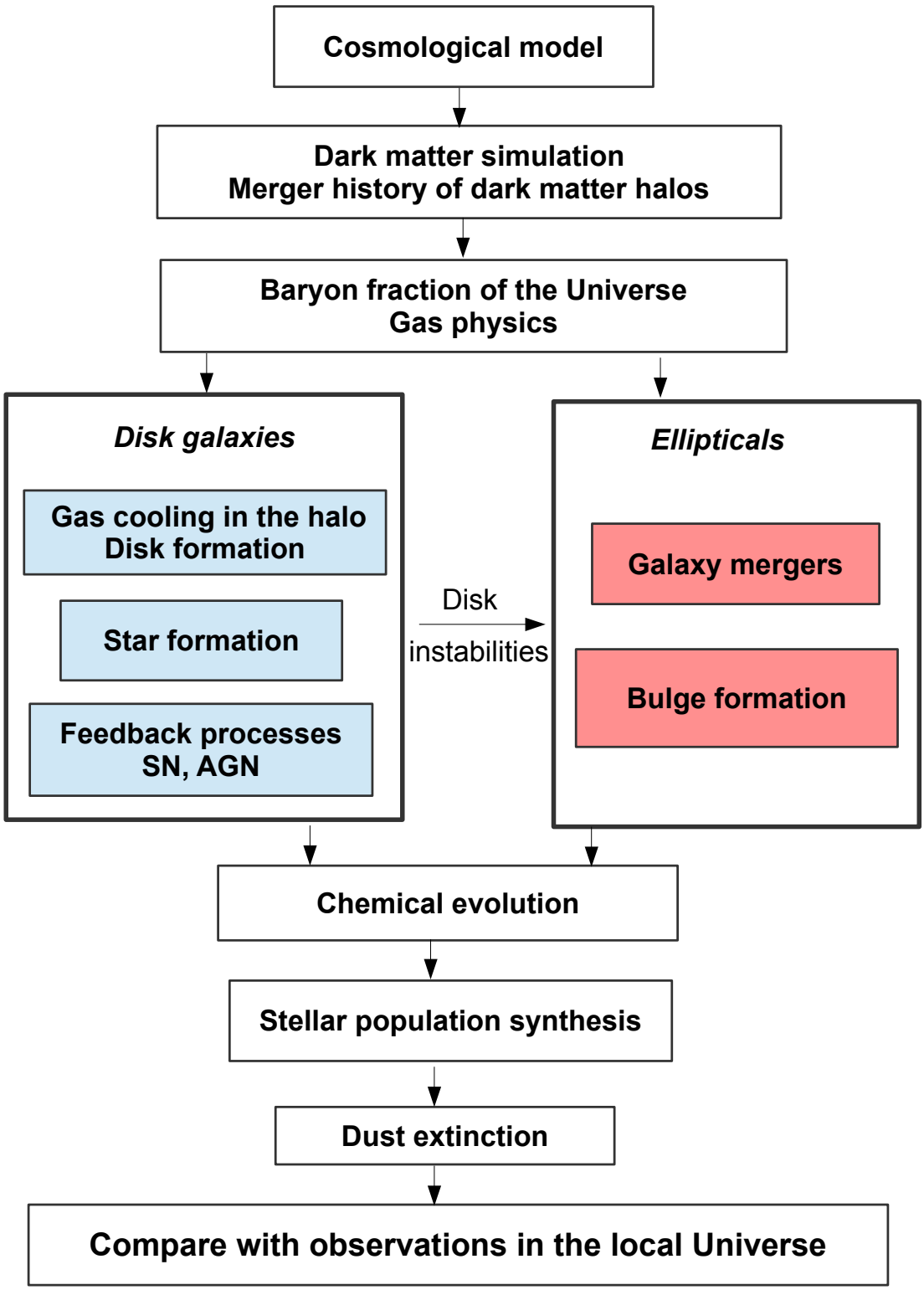

Figure 2.4: Sketch showing the general step-by-step algorithm followed by semi-analytical models.

more massive halos cooling is driven by atomic hydrogen. The star formation at this stage lead to creation of HII regions which eventually cover intergalactic medium (IGM) and only then the reionization is complete.

This reionization has several impacts on the cooling of gas in small-mass halos. First, the heating of IGM by the UV radiation increases the pressure to a point that accretion of gas onto these halos is suppressed, leading to a decrease in the baryon fraction of the halo. Secondly, the heating and ionization of the gas in the halos, both of which effects suppress further cooling and star formation. In high-mass halos the ionization radiation has little impact because the recombination rate is higher.

Formation of disk When the gas cools and accretes, it accretes towards the centre of the halo. This is because the baryons in the DM halo are assumed to have the same angular momentum as the hosting halo. To conserve the angular momentum, gas falls towards the centre of the halo and settles in a flat disk. The size of the disk then determines the surface mass density of gas. According to an empirical relation, the surface mass density falls exponentially from the centre:

$$\Sigma(R) = \Sigma_0 \exp\left(-\frac{R}{R_\mathrm{d}}\right), \tag{2.49}$$

where Σ_0 is the central surface density and R_d is the scale-length of the disk which is related to the angular momentum, mass and the circular velocity of the disk. Once this surface density exceeds a threshold, star formation sets in. The star formation rate (SFR) is then parametrized in terms of the surface density of the cold gas in the disk.

Supernovae feedback The newly formed massive stars have short lifetimes. They die young and explode as supernovae, injecting their kinetic energy into the interstellar medium. This transfer of energy heats the gas and suppresses further cooling. This feedback from the supernovae provide a self-regulating star-formation mechanism without which all the cool gas in the disk would transform into stars. The energy and radiation from supernovae is assumed to have two major impact on the gaseous content of the galaxy. It injects the cold gas in the disk to the hot halo and also blow away the hot gas from the halo which may accrete to the halo at later times. The rate at the which the mass of gas is reheated and ejected depends on the efficiencies of these two effects which in turn depend on assumptions of the initial mass function (IMF). In the semi-analytic models these efficiencies are parametrized in such a way to match the observed stellar mass function up to galaxy-mass halos.

AGN feedback Active galactic nuclei (AGNs) release large amount of energy to the IGM and have a significant impact on galaxy formation. Their energy is powered by a supermassive black hole (SMBH) in the centre of the halo. SMBH growth is due to accretion of gas ("radio" mode) or through mergers ("quasar" mode). When galaxies merge, their SMBHs also merge and the cold gas accretes to the centre of the more massive galaxy. Accreting SMBHs in bright AGNs release energy in the form of radiation to the AGN surrounding. This radiation in turn heats up the gas and prevents further star formation. In the "radio" mode, the AGN feedback is through accretion of hot gas to the SMBH and releasing energy by relativistic jets and radio lobs. This energy is then deposited to the environment as heat which in turn will prevent star formation.

Mergers and bulge formation When two halos (and the galaxies inside) collide if the collision velocity is comparable or smaller than the intrinsic velocity of the colliding halos, merging of the two component happens. The halo merger trees from the simulation provide a way to trace back the merger

history of each halo. The mergers occur between a central halo and a subhalo or two subhalos. The fate of these halos and their galaxies is considered depending on their mass ratios. If the mass ratio is large, "minor" mergers occur and if they have similar masses "major" mergers occur.

In minor mergers, a smaller mass halo/galaxy merges with a more massive one. The properties of the massive merging partner doesn't change noticeably. The low-mass galaxy will become a satellite in the massive galaxy and its evolution is subject to several mechanisms. The satellite's orbit decreases due to dynamical friction and its gas gets disrupted to be added to the disk of the massive progenitor, which may be incorporated in a starburst event. The stars in the satellite will be added to the bulge or the thick disk component. As the orbit shrinks the tidal forces become stronger and eventually the satellite will be completely disrupted and its mass adds to the mass of the massive galaxy.

Major mergers change the morphology of galaxies significantly. The disk of both progenitors are assumed to be destroyed and the gas and stars add to a spheroidal component. As for minor mergers, major collision of cold gas of both merging partner undergo starburst ("collisional starburst"). The feedback from the newly formed stars causes ejection or heating of the gas and suppress further cooling and star formation. Major mergers provide a possible scenario for the formation of elliptical galaxies. Therefore, if the merger occurs between gas-rich galaxies of comparable mass at high redshifts, an elliptical galaxy forms which eventually will have old and red population of stars. These galaxies are preferentially found in high density regions such as groups. They may undergo further merging with other ellipticals the outcome of which is yet another elliptical galaxy probably with higher mass. However, if they are more isolated, they might accrete gas from the surrounding which will cool in a disk and therefore lead to the formation of disk galaxies with a bulge component.

Another scenario leading to formation of bulges is disk buckling. When the disk component becomes unstable and its self-gravity dominates, the disk is not rotationally supported anymore. When this happens, sufficient amount of mass is transferred to the bulge component until the disk becomes stable again.

Dynamical evolution Satellites moving in orbits of a more massive halos are subject to several forces imposed by the host halo which strip the satellite galaxy of its hot gas, partially or in extreme cases entirely. Dynamical friction causes shrinking of the orbit of the satellite. The tidal forces exerted are stronger closer to the centre of the host halo and lead to the removal of the material, namely hot gas, from the satellite. The amount of gas stripped in this way is correlated to the amount of dark matter removed from the subhalo by tidal forces. This is due to the property that tidal forces act on the dark matter and gas in a similar way.

Another effect is the stripping of gas due to ram-pressure forces. This force is triggered by the motion of satellites in the intracluster medium. It depends on the square of the orbital velocity of the satellite with respect to the medium and on the density of the intracluster medium. The amount of gas stripped from the galaxy depends on how the self-gravity of the galaxy balances the ram-pressure.

Chemical evolution The initial metal enrichment of the IGM happens after massive population III stars die. They inject metals to IGM through supernova explosion. Typically when stars evolve, they eject heavy elements to the surrounding through supernova explosions and stellar winds, therefore increasing the metallicity. The metals released to the hot diffuse gas in the galaxy can later be used in the cooling process, since it is easier for the metal-rich gas to cool, and incorporate to formation of metal-rich stars. Alternatively, they might be completely ejected from the galaxy and later on be accreted onto the same system or a neighbouring one.

Stellar population synthesis The light emitted from galaxies carries information about the stellar population and star formation history of the galaxy. Stellar population synthesis models are widely used in semi-analytical models to infer spectral properties of galaxies based on their stellar content. These models are based on the "isochrone synthesis". The main ingredients in this approach are the stellar IMF and star formation history. We call a "simple stellar population" (SSP) a population of stars with the same age (born in the same star formation event) and the same metallicity, and which follow a mass distribution given by an assumed IMF. These stars are located on an isochrone in the HR diagram (hence the name isochrone synthesis) and the sum of their stellar spectra is the spectral energy distribution (SED) of the population. Assuming a model for the star formation rate (SFR), the isochrone synthesis then defines the SED of galaxies with specific SFR as the integrated SED of SSPs over time. The spectral evolution of SSPs are the natural outcome of the synthesis models. The photometric properties can also be obtained with specific filters such as the ones commonly used in the observation to predict the photometric properties of the SSPs and the galaxies composed of these SSPs.

Dust extinction The presence of dust in galaxies affect their spectra and consequently their observed magnitude and colors. The effect is more prominent at short wavelengths leading to reddening of the emitted spectra. In other words dust extinction is more prominent in optical and UV range. The amount of this attenuation depends on the creation rate, physical properties (chemical composition and size), and the distribution of dust grains.

Semi-analytical models parametrize dust extinction in terms of optical depth of the dust. In these models the attenuation by dust depends on the column density and metallicity of the gas.

2.5 Semi-analytical models used in this thesis

We use two SAMs developed in Durham and in Garching. Both models follow the recipes explained in the previous section, however they differ in some details. In the following we summarise the main assumptions in each model and highlight some similarities and differences between the models.

2.5.1 Garching model (G11 and H15)

Garching models laid out in Guo et al. (2011), hereafter G11, and Henriques et al. (2015), hereafter H15, are updates of the model by Springel et al. (2005) developed in Garching. An illustration of the local galaxy distribution in this model is shown in Fig. 2.5.

Both G11 and H15 are implemented on MS and MS-II. As mentioned before the cosmological parameters assumed in these DM simulations are taken from WMAPI (Spergel et al. 2003). In H15, MS and MS-II simulations are rescaled (according to: Angulo & Hilbert 2015; Angulo & White 2010) so that the outcome of the simulation is represented according to the Planck cosmology (Planck Collaboration et al. 2014). The cosmological parameters are listed in Table 5.2. We now describe how the different physical processes described in the previous section are modelled.

Reionization Reionization increases the temperature of the IGM and thus the gas pressure. Therefore the infall of gas in DM halo is suppressed in low-mass halos and the baryon fraction is then smaller in these halos. Considering the effects of hot IGM on halos, SAMs can track how much baryonic matter is available in the halo of a given mass at a given time. These baryons are then distributed in five components: in the form of hot halo gas, cold disk gas, stars in the disk and in the bulge, and ejecta reservoir.

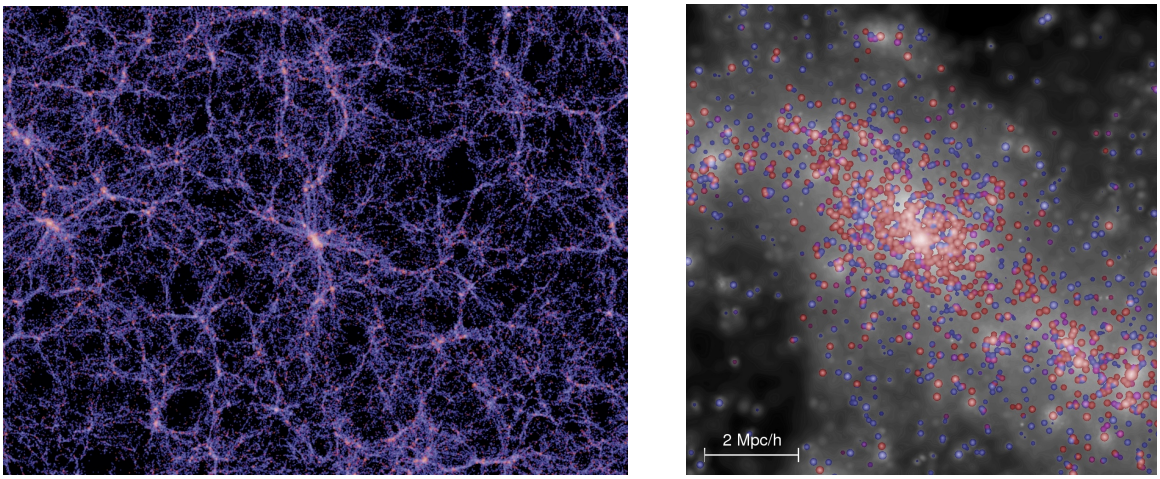

Figure 2.5: Galaxy distribution in the Garching model by Springel et al. (2005) at $z = 0$ both on very large scales (left panel) and for a massive cluster of galaxies (right panel). Colors encode the rest frame stellar $B - V$ color index. The underlying dark matter distribution is shown in Fig. 2.3. Credit: http://www.mpa-garching.mpg.de/galform/virgo/millennium

G11 and H15 assign a fraction of baryons f_b to each DM halo and also take into account the effect of reionization on this baryon fraction. They use fitting formula obtained from hydrodynamical simulations of reionization effects originally proposed by Gnedin (2000) to describe how the baryon fraction in a halo depends on mass and redshift of the halo:

$$f_b(z, M_{vir}) = \frac{f_b^{cos}}{\left(1 + (2^{\alpha/3} - 1)\left[\frac{M_{vir}}{M_C(z)}\right]^{-\alpha}\right)^{3/\alpha}} . \tag{2.50}$$

In this formula, M_{vir} is the virial mass of the DM halo, α is a free parameter and is set to $\alpha = 2$ to fit the hydrodynamical simulations of reionization in Okamoto et al. (2008). M_C is a characteristic halo mass which halos would have on average half of baryons they would have in the absence of reionization effect (the Universal baryon fraction). In halos with $M_{vir} \gg M_C$, the baryon fraction is set to the universal value whereas for halos with $M_{vir} \ll M_C$, the baryon fraction drops to $(M_{vir}/M_C)^3$. M_C adopts values from $\sim 6.5 \times 10^9 M_\odot$ (corresponding to circular velocity of $25 km\, s^{-1}$) at present to $\sim 10^7 M_\odot$ just before reionization starts at $z \sim 8$ according to Okamoto et al. (2008).

G11 adopts the universal baryon fraction as given by first year WMAP estimates, $f_b^{cos} = 17\%$, and in H15, $f_b^{cos} = 15.5\%$ according to the Planck cosmology.

Different reionization recipes lead to different luminosity and stellar mass estimates for low-mass galaxies. By comparing the observed luminosity function of Milky Way satellite galaxies to the simulated one using different reionization prescriptions, G11 argues in favor of Okamoto et al. (2008) parameters in order to reproduce the predicted number of faint galaxies. They claim that reionization effects have noticeable effect only on the abundance of faint dwarf galaxies (with masses below $10^7 M_\odot$).

Gas cooling The hot gas of a galaxy is assumed to have an isothermal distribution, $\rho_{hot}(r) = \frac{M_{hot}}{4\pi R_{vir} r^2}$, with M_{hot} being the total hot gas mass associated with the halo of virial radius R_{vir},

$$M_{hot} = f_b M_{vir} - \Sigma_i M_{cold}^{(i)} , \tag{2.51}$$

where $M_{\rm cold}$ is the cold gas mass and the sum extends over all galaxies in the halo. The temperature of the hot gas component in the halo is assumed to be the same as the virial temperature of the halo, $T_{\rm vir} = \frac{1}{2}\frac{\mu m_{\rm H}}{k_{\rm B}} V_{\rm vir}^2$ or $T_{\rm vir} = 35.9(V_{\rm vir}/{\rm km\,s^{-1}})^2{\rm K}$.

The stellar component of the disk is formed by cooling and accretion of this surrounding hot gas. The time it takes for the hot gas to lose its thermal energy at constant cooling rate is the "cooling time", $t_{\rm cool}$, and the "cooling radius", $r_{\rm cool}$, is the radius where the cooling time equals the halo dynamical time. G11 and H15 assume the dynamical time of the halo (the time required to orbit across the halo) to be $t_{\rm dyn,h} = R_{\rm vir}/V_{\rm vir} = 0.1H(z)^{-1}$ (De Lucia et al. 2004). This choice of $t_{\rm dyn,h}$ when defining the cooling radius results in the prediction of the amount of gas condensed in the halo to be in good agreement with hydrodynamical simulations (Croton et al. 2006).

Both models distinguish between "rapid infall" and "cooling flow" regimes. The rapid infall regime is when $r_{\rm cool} > R_{\rm vir}$ and the halo accretes gas on free-fall. The cooling rate is in this case:

$$\dot{M}_{\rm cool} = \frac{M_{\rm hot}}{t_{\rm dyn,h}} \,. \tag{2.52}$$

In massive halos, when $r_{\rm cool} < R_{\rm vir}$ the gas accretes via a cooling flow at a rate:

$$\dot{M}_{\rm cool} = M_{\rm hot}\frac{r_{\rm cool}}{R_{\rm vir}}\frac{1}{t_{\rm dyn,h}} \,. \tag{2.53}$$

Formation of disk The size of the disk is determined by the angular momentum of the gas which has settled in the disk. G11 and H15 assume a disk model that distinguishes between the stellar disk and the gas disk component. According to the model, angular momentum of the gas disk ($J_{\rm gas}$) changes due to gas cooling, accretion and star formation and the angular momentum of stellar disk (J_*) only changes by star formation. They also assume both stellar and gas disks have exponential density profiles (Eq. 2.49).

The scale-length of the gas and stellar disk then can be calculated to be related to the mass and angular momentum of the gaseous and stellar disks and also the rotational velocity of the disks which is assumed to be constant and equal to the maximum circular velocity of the halo. Using this treatment, G11 finds a fairly good agreement with observational results, such as the distribution of the stellar half-mass radius for local disk galaxies as function of stellar mass extracted by Shen et al. (2003) using data from the Sloan Digital Sky Survey (SDSS, Stoughton et al. 2002).

Star formation Stars form from the cold gas only when its mass exceeds a threshold calculated using models for the instability of a rotationally supported disk (see e.g. Toomre 1964). The critical mass that the cold gas must attain for the star formation to be efficient is assumed to be:

$$M_{\rm crit} = M_{\rm crit,0}\left(\frac{V_{\rm vir}}{200{\rm km\,s^{-1}}}\right)\left(\frac{R_{\rm gas,d}}{10{\rm kpc}}\right) , \tag{2.54}$$

where $R_{\rm gas,d}$ is the scale-length of the gaseous disk and $M_{\rm crit,0} = 3.8\times10^9{\rm M}_\odot$ is a fixed parameter in G11 to produce comparable results with Milky Way observations. However, H15 adopts a $M_{\rm crit,0}$ value which is smaller by a factor of two.

The star formation rate (SFR) then can be calculated:

$$\dot{M}_* = \alpha_{\rm SF}\frac{(M_{\rm gas} - M_{\rm crit})}{t_{\rm dyn,d}} \,, \tag{2.55}$$

where $M_{\rm gas}$ is the total cold gas mass and $\alpha_{\rm SF}$ is a free efficiency parameter. The dynamical time of the disk is calculated by $t_{\rm dyn,d} = 3R_{\rm gas,d}/V_{\rm max}$ in G11 and $t_{\rm dyn,d} = R_{*,\rm d}/V_{\rm max}$ in H15.

Supernovae feedback The total energy available from supernovae and stellar winds, $\Delta E_{\rm SN}$, is assumed to reheat the cold disk gas and eject it to the hot halo or to heat the hot gas atmosphere directly and transfer it to the ejecta reservoir. This energy is parametrized as:

$$\Delta E_{\rm SN} = \epsilon_{\rm halo} \times \frac{1}{2}\Delta M_* V_{\rm SN}^2 \,, \tag{2.56}$$

where $\frac{1}{2}V_{\rm SN}^2$ is the mean kinetic energy released per unit of mass of stars formed and $V_{\rm SN} = 630{\rm km\,s^{-1}}$ based on assumptions of stellar IMF and standard supernova explosion theory. ΔM_* is the mass of newly formed stars. $\epsilon_{\rm halo}$ is the efficiency parameter with which the supernova ejecta heats the gas and is defined as:

$$\epsilon_{\rm halo} = \eta \times \left[0.5 + \left(\frac{V_{\rm max}}{70{\rm km\,s^{-1}}}\right)^{-\beta_2}\right] , \tag{2.57}$$

in G11 and

$$\epsilon_{\rm halo} = \eta \times \left[0.5 + \left(\frac{V_{\rm max}}{V_{\rm eject}}\right)^{-\beta_2}\right] , \tag{2.58}$$

in H15. η and β_2 are free parameters. η accounts for possible variations of the IMF and supernova assumptions. β_2 controls the dependency of the ejection efficiency on the maximum circular velocity $V_{\rm max}$ and affects the amplitude of the stellar mass function at the low-mass end. $V_{\rm eject}$ is a free parameter in H15 model which quantifies the supernova ejection scale and its best fit value is $110{\rm km\,s^{-1}}$.

Part of the energy injected by supernovae goes to reheating the cold gas in the disk, $\Delta E_{\rm reheat}$,

$$\Delta E_{\rm reheat} = \frac{1}{2}\Delta M_{\rm reheat} V_{\rm vir}^2 \,. \tag{2.59}$$

The amount of reheated cold gas mass $\Delta M_{\rm reheat}$ is proportional to the mass of newly-formed stars,

$$\Delta M_{\rm reheat} = \epsilon_{\rm disk} \Delta M_* \,, \tag{2.60}$$

where $\epsilon_{\rm disk}$ is the efficiency parameter parametrized by:

$$\epsilon_{\rm disk} = \epsilon \times \left[0.5 + \left(\frac{V_{\rm max}}{70{\rm km\,s^{-1}}}\right)^{-\beta_1}\right] ,$$

in G11 and

$$\epsilon_{\rm disk} = \epsilon \times \left[0.5 + \left(\frac{V_{\rm max}}{V_{\rm reheat}}\right)^{-\beta_1}\right] , \tag{2.61}$$

in H15. ϵ is the ratio of reheated mass to the new stellar mass ($\epsilon = 6.5$ in G11 and $\epsilon = 2.6$ in H15) and β_1 is the scaling of this ratio with $V_{\rm max}$ and affects the slope of the stellar mass function at the low-mass end ($\beta_1 = 3.5$ and $\beta_1 = 0.80$). The best fit value of $V_{\rm eject} = 430{\rm km\,s^{-1}}$ is used in H15. It should be mentioned that in all the previous versions of the Garching model, the efficiency parameters $\epsilon_{\rm halo}$ and $\epsilon_{\rm disk}$ were taken to be constant. However, G11 argues that using a constant efficiency does not suppress the star formation enough to reproduce the observed stellar mass function.

The remaining energy of supernova is spent on ejecting gas from the hot halo to the ejecta reservoir. The amount of ejected material is estimated by:

$$\Delta M_{\rm eject} = \frac{\Delta E_{\rm SN} - \Delta E_{\rm reheat}}{\frac{1}{2}V_{\rm vir}^2} \tag{2.62}$$

The material ejected from the system is stored in the ejecta reservoir associated with halo and will be reincorporated to the halo at later times. It should be noted that the exact location of the reservoir is not clear. G11 adopts a model to calculate the rate with which the reservoir gas reaccrete to the halo,

$$\dot{M}_{\rm eject} = -\gamma\left(\frac{V_{\rm vir}}{220{\rm km\,s^{-1}}}\right)\left(\frac{M_{\rm eject}}{t_{\rm dyn,h}}\right), \tag{2.63}$$

where $\gamma = 0.3$ is a free parameter. The dependence of the $\dot{M}_{\rm eject}$ to the circular velocity ($V_{\rm vir}$) in G11 is motivated by the assumption that in low-mass halos, hot winds have higher velocities than the escape velocity of the halo; therefore the reaccretion of the gas is more difficult. However, comparing the stellar mass function predicted by G11 with observations, it seems that low-mass galaxies form too early in the model. H15 addresses this issue by introducing a $\dot{M}_{\rm eject}$ model that depends on the reincorporation time rather than circular velocity.

$$\dot{M}_{\rm eject} = -\frac{M_{\rm eject}}{t_{\rm reinc}}, \tag{2.64}$$

with

$$t_{\rm reinc} = -\gamma'\frac{10^{10}{\rm M_\odot}}{M_{\rm vir}}. \tag{2.65}$$

AGN feedback The "quasar mode" applies to the mergers of black holes. During mergers, the mass of the major progenitor (central galaxy) increases by absorbing the black hole mass of the minor progenitor (satellite galaxy) and by accreting gas (with mass of $M_{\rm cold}$). The increase in the central black hole mass ($\Delta M_{\rm BH,Q}$) is proportional to the total cold gas mass and is calculated by:

$$\Delta M_{\rm BH,Q} = \frac{f_{\rm BH}(M_{\rm sat}/M_{\rm cen})M_{\rm cold}}{1 + (V_{\rm BH}/V_{\rm vir})^2}, \tag{2.66}$$

where $M_{\rm cen}$ and $M_{\rm sat}$ are the total baryonic mass of the central and satellite galaxies (major and minor progenitors), $f_{\rm BH}$ is a free parameter controlling the black hole growth efficiency. G11 adopts $f_{\rm BH} = 0.03$ in order to reproduce the local observations of $M_{\rm BH} - M_{\rm bulge}$ relation. $f_{\rm BH}$ and $V_{\rm BH}$ are adjustable free parameters in H15 (set to $f_{\rm BH} = 0.036$ and $V_{\rm BH} = 730{\rm km\,s^{-1}}$), where $V_{\rm BH}$ describes the virial velocity at which the efficiency saturates. $V_{\rm vir}$, as usual, is the virial velocity of the central halo.

The "radio mode" feedback applies to the growth of the central black hole due to accretion of hot gas. The growth rate in G11 is calculated following the prescription in Croton et al. (2006):

$$\dot{M}_{\rm BH} = k\left(\frac{f_{\rm hot}}{0.1}\right)\left(\frac{V_{\rm vir}}{200{\rm km\,s^{-1}}}\right)^3\left(\frac{M_{\rm BH}}{10^8 h^{-1}{\rm M_\odot}}\right), \tag{2.67}$$

where k is the efficiency of the accretion and is set to $1.5\times10^{-5}{\rm M_\odot yr^{-1}}$ in G11 in order to match the stellar mass function at the high-mass end. $f_{\rm hot}$ is assumed to be the ratio of the hot gas mass and the total halo mass. H15 adopts,

$$\dot{M}_{\rm BH} = k_{\rm AGN}\left(\frac{M_{\rm hot}}{10^{11}{\rm M_\odot}}\right)\left(\frac{M_{\rm BH}}{10^8{\rm M_\odot}}\right), \tag{2.68}$$

which is essentially Eq. (2.67) divide by the expansion rate, $H(z)$, to account for the enhancement of

accretion of hot gas at lower redshifts which they accounted for by introducing longer reincorporation time ($t_{\rm reinc}$). The radio feedback efficiency is $k_{\rm AGN} = 4.4 \times 10^{-3} {\rm M}_{\odot} {\rm yr}^{-1}$ in H15.

The energy released by the radio jets has the rate of:

$$\dot{E}_{\rm radio} = \eta \dot{M}_{\rm BH} {\rm c}^2 \,, \tag{2.69}$$

where η is the efficiency parameter set to 0.1 in both models and c is the speed of light. The energy released in the radio mode decreases the cooling rate of the hot gas to the cold disk resulting in the effective cooling rate of:

$$\dot{M}_{\rm cool,eff} = \max\left[\dot{M}_{\rm cool} - 2\dot{E}_{\rm radio}/V_{\rm vir}^2, 0\right] . \tag{2.70}$$

Mergers and bulge formation In G11 and H15, galaxies are classified into three groups: type 0 galaxies are the central galaxies of the main (sub)halo, type 1 galaxies are satellite galaxies residing in non-dominant subhalos, and type 2 galaxies are satellite galaxies which have lost their own subhalo or equivalently their subhalo has fallen below the detection limit of the simulation. Type 2 galaxies are referred to as "orphan" galaxies. Each galaxy is born as a central, i.e. type 0, and only after they fall into a bigger system they become type 1. The orbit of this satellite in the massive halo decreases due to dynamical friction until the merging is completed. The merger clock is switched on as soon as the subhalo mass drops below that of the galaxy it contains and the position and velocity of the most bound particle of the subhalo are assigned to the satellite galaxy. Merging is completed after $t_{\rm friction}$ time has passed. $t_{\rm friction}$ is the time of the orbital decay due to dynamical friction and is (for derivation see, Binney & Tremaine 1987):

$$t_{\rm friction} = \alpha_{\rm friction} \frac{V_{\rm vir} r_{\rm sat}^2}{G M_{\rm sat} \ln \Lambda} \,, \tag{2.71}$$

where $\alpha_{\rm friction}$ is a parameter needed to reproduce the bright end of observed luminosity function at $z = 0$ ($\alpha_{\rm friction} = 2.34$ in G11 and $\alpha_{\rm friction} = 2.6$ in H15). $M_{\rm sat}$ is the total mass of the satellite (i.e. the DM mass of the subhalo + the baryonic mass of the galaxy). $\ln \Lambda = \ln(1 + \frac{M_{\rm vir}}{M_{\rm sat}})$ is the Coulomb logarithm.

In the case that a type 2 galaxy is merging with a type 1 or type 0 galaxy, when the merging clock is set, the velocity of the orphan is the velocity of the particle that it is identified with (i.e. the most bound particle). However the position of the orphan equals that of a particle whose positional offset from the central galaxy is multiplied by $(1 - \frac{\Delta t}{t_{\rm friction}})$ where Δt is the time since the merger clock started. Therefore, when $\Delta t = t_{\rm friction}$ the merging processes has been completed.

Major mergers happen when the total baryonic mass ratio of the less massive galaxy to the more massive one exceeds $R_{\rm merger}$, otherwise the merging is minor. $R_{\rm merger}$ is set to 0.3 (0.41) in G11 (H15), respectively.

When major mergers occur, all the stars (newly formed and pre-existing) are associated with the bulge of the new galaxy formed, whereas in minor mergers the newly formed stars are added to the disk of the more massive progenitor and only the pre-existing stars of the lower mass progenitor are added to the bulge. Using the conservation of energy and the virial theorem, G11 and H15 compute the bulge size after a merger event (major and minor) to be :

$$\frac{G M_{\rm new,bulge}^2}{R_{\rm new,bulge}} = \frac{G M_1^2}{R_1} + \frac{G M_2^2}{R_2} + \frac{\alpha_{\rm inter}}{c} \frac{G M_1 M_2}{R_1 + R_2} \,. \tag{2.72}$$

The left-hand side of the equation represents the gravitational binding energy of the final bulge with stellar mass $M_{\rm new,bulge}$ and half-mass radius $R_{\rm new,bulge}$. The right-hand side of the equation is the sum of

the binding energy of each progenitor with stellar mass M_1 and M_2 and stellar-half-mass radii R_1 and R_2 and the binding energy of the relative orbit of the two progenitors. c is the form factor relating the binding energy to the mass and radius of a galaxy and its value depends on the density profile of the galaxy; $c = 0.45$ for a bulge with $r^{1/4}$ profile and $c = 0.49$ for an exponential disk. G11 and H15 adopt $c = 0.5$. $\alpha_{\rm inter}$ is a parameter quantifying the interactions between the two progenitors and is set to 0.5 in both models to match the observed bulge sizes measured from SDSS data. Bulge formation due to disk instabilities occur when

$$V_{\rm max} < \sqrt{\frac{GM_{*,\rm d}}{3R_{*,\rm d}}} \tag{2.73}$$

is satisfied. $M_{*,\rm d}$ and $R_{*,\rm d}$ are the mass and radius of the stellar disk. The factor 3 is inserted to account for the fact that $V_{\rm max}$ is significantly larger for an unperturbed halo than a perturbed one.

Dynamical evolution When a (sub)halo becomes part of a larger system, it loses mass due to tidal stripping. The tidal radius, $R_{\rm tidal}$, is the radius beyond which the matter is stripped away from the halo and is given by

$$R_{\rm tidal} = \left(\frac{M_{\rm DM}}{M_{\rm DM,infall}}\right) R_{\rm DM,infall}\,, \tag{2.74}$$

where $R_{\rm DM,infall}$ is the $R_{\rm vir}$ of the halo prior to the infall, $M_{\rm DM}$ is the current dark matter mass of the halo and $M_{\rm DM,infall}$ is $M_{\rm vir}$ just before the infall. This relation is based on the assumption that the density fallows an isothermal profile ($\rho \propto r^{-2}$) and therefore $M \propto r$.

Another stripping agent is the ram-pressure which affects the hot gas of the satellite as soon as it first falls within the virial radius of the hosting halo. The ram-pressure force is effective for distances (from the centre of the satellite) larger than $R_{\rm r.p.}$. At $R_{\rm r.p.}$ the self-gravity of the satellite balances the ram-pressure. The minimum of $R_{\rm r.p.}$ and $R_{\rm tidal}$ is taken as the stripping radius of the satellite. The hot gas in "ejecta reservoir" is assumed to be stripped in proportion to the hot gas component of the satellite. Once these hot gas components are stripped, they'll be part of the corresponding hot gas components of the main (sub)halo and will not be reincorporated to the same subhalo they were stripped off in the first place.

The stellar and cold gas components are tidally disrupted in the models only after the satellite has become type 2 and lost the DM subhalo. The position of this orphan galaxy is traced by the position of the most bound particle at the time the halo could still be identified. The orphan satellite is completely disrupted of its stars and cold gas when its density within half-mass radius falls below the dark matter density of the main halo within the pericentre of the satellite's orbit. When this condition is satisfied, the stars of the orphan are added to the intracluster stars of the central galaxy and the cold gas is added to its hot gas atmosphere.

Chemical evolution Both G11 and H15 follow the model of metal enrichment by De Lucia et al. (2004). In this model, each solar mass of gas converted into stars produces a mass ("yield") Y of metals. In Fig. 2.6, the exchange of metals between different baryonic component of a galaxy is shown. Through star formation, cold gas and the metals are transferred to stars (with 100% efficiency), and through feedback processes and winds these metals can be transferred to the gas component or be ejected entirely (stored in the ejecta reservoir) to be reincorporated at later times. G11 computed the metallicity of cold interstellar medium gas as function of stellar mass for star-forming galaxies. They show that their results match the observational results of the gas-phase oxygen abundance as function of stellar mass for star-forming galaxies in SDSS at $z = 0.1$ quite well. They argue that this is mainly

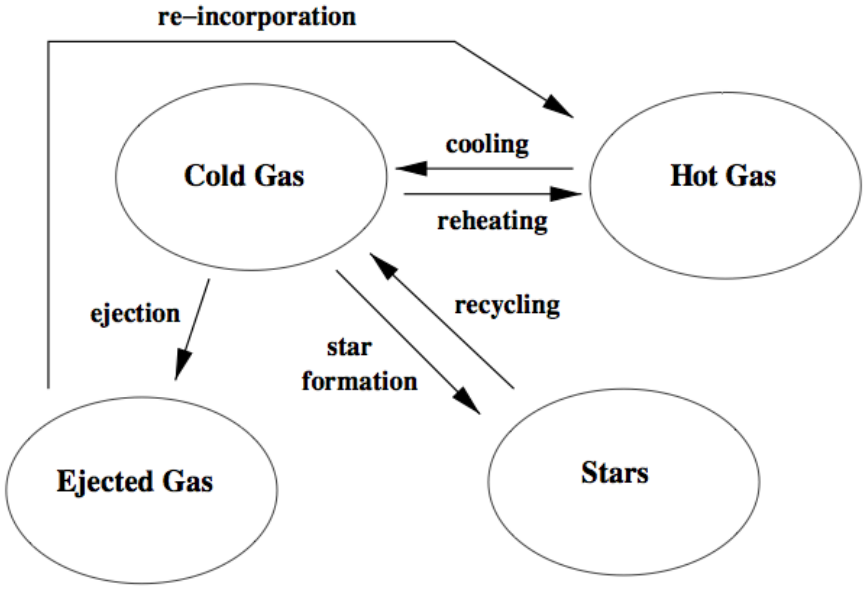

Figure 2.6: Sketch showing how mass and metals are exchanged between different baryonic components of a galaxy in the G11 and H15 models. The physical process driving each exchange is indicated by arrows. Source: De Lucia et al. (2004).

due to the introduction of a velocity-dependent supernovae feedback efficiency.

Stellar population synthesis The photometric properties of galaxies in G11 are obtained using stellar population synthesis (SPS) model by Bruzual & Charlot (2003), whereas in H15 the default model is that of Maraston (2005). H15 argues that for Garching SAMs, newer SPSs produce better agreement with observations of mass function and K-band luminosity function. One of the major differences between these SPSs is the treatment of thermally pulsating AGB (TP-AGB) stars which can lead to different predictions of spectral flux for the population of stars considered.

Dust extinction Dust extinction depends on the metallicity, gas column density and redshift. The redshift dependency introduced by G11 follows $(1+z)^{-0.4}$ to ensure that galaxies at high redshift have little dust, as observed. H15 adopts even stronger redshift dependency, $(1+z)^{-1}$. Following De Lucia & Blaizot (2007), the overall extinction curve at each wavelength λ in G11 and H15 is given by:

$$A_\lambda = -2.5 \log \left(\frac{1 - \exp^{-\tau_\lambda \sec\theta}}{\tau_\lambda \sec\theta} \right), \tag{2.75}$$

where τ_λ is the optical depth and θ is the inclination angle of the galaxy with respect to line of sight. τ_λ depends on the metallicity and the redshift (see H15, equation S37).

Observational constraints We call the *stellar mass function* (SMF) the abundance of galaxies as function of stellar mass. One of the achievements of the Garching models is the good agreement between the predicted SMF and the observed one in the local Universe. This is mainly due to enhanced treatments of feedback processes. For supernovae feedbacks they assume that the efficiencies with which cold disk gas is reheated and the gas ejection efficiency are not constant (unlike what was assumed in the previous

Table 2.2: Free parameters assumed in G11 and H15 to calibrate the stellar mass function.

Parameters	G11	H15
$\alpha_{\rm SF}$ (star formation efficiency - Eq. 2.55)	0.02	0.03
ϵ (SN reheating efficiency - Eq. 2.61)	6.5	2.6
$V_{\rm reheat}[{\rm km\,s^{-1}}]$ (SN reheating scale - Eq. 2.61)	–	430
β_1 (SN reheating slope - Eq. 2.61)	3.5	0.8
η (SN ejection efficiency - Eq. 2.58)	0.32	0.64
$V_{\rm eject}[{\rm km\,s^{-1}}]$ (SN ejection efficiency - Eq. 2.58)	–	110
β_2 (SN ejection slope - Eq. 2.58)	3.5	0.81
γ (Ejecta reincorporation efficiency - Eq. 2.63)	0.3	–
γ'[yr] (Ejecta reincorporation - Eq. 2.65)	–	3.6×10^{10}
$K[{\rm M_\odot yr^{-1}}]$ (Hot gas accretion on to black hole efficiency - Eq. 2.67)	1.5×10^{-5}	–
$k_{\rm AGN}[{\rm M_\odot yr^{-1}}]$ (Radio feedback efficiency - Eq. 2.68)	–	4.4×10^{-3}

versions of the model) but depend on the rotational velocity of the disk which is approximated by maximum circular velocity of the hosting DM (sub)halo. The list of parameters which were adjusted to tune the model result with the observations of mass function in G11 and H15 are given in Table 2.2.

G11 tune their parameters by mainly fitting the model prediction to the observed local stellar mass function, whereas H15 uses the observed stellar mass function of galaxies at $z = 0, 1, 2$ and 3 and also the observed fraction of "passive" (no longer star forming) galaxies as function of stellar mass at redshifts $z = 0, 0.4, 1, 2$ and 3 to find the best fit parameters.

It should be noted that G11 and H15 use the same initial mass function, Chabrier (2003) IMF, as the observational measurements they use to tune their model parameters. This way, the uncertainties in stellar mass estimates from the IMF is not relevant for their fitting. In SMF fitting, G11 and H15 convolve the model stellar masses by a Gaussian function with a fixed (redshift dependent) dispersion to account for the uncertainties in the observed stellar mass estimates. Moreover, H15 takes into account the difference in stellar mass estimates due to different choices of SPS models; observational measurements assume Bruzual & Charlot (2003) SPS model, whereas H15 uses SPS model of Maraston (2005).

Observations suggest that most of the low-mass galaxies are star forming at late times and more massive galaxies have higher star formation rate at high redshift than the local Universe. G11 appear to produce too many low-mass galaxies which have stopped star formation early and turned red. H15 addresses this issue by improving the timescale for the reincorporation of gas ejecta (the gas that has beed expelled from the galaxy and will accrete again at some later time) and also by lowering the threshold of the cold gas density for star formation and also removing the ram-pressure stripping of low-mass galaxies. All these improvements prevent the low-mass satellite galaxies to form early and turn red early. Therefore, H15 can model more accurately the evolution of stellar mass function up to high redshifts and in full stellar mass range considered in the observations.

As mentioned before, G11 and H15 approximate the disk rotational velocity by the maximum circular velocity of the halo. One consequence of this assumption can be seen in the prediction of the *Tully-Fisher relation*, the relation between the luminosity and the rotational velocity. Comparing with observations, G11 and H15 produce fairly good agreement with the observational data over an absolute magnitude range of 8 mag.

Models also measure the abundance of galaxies as function of luminosity, or the *luminosity function* of galaxies, to match the observed one. G11 shows that although their model slightly overpredicts the

abundance of low-mass galaxies, their abundance as function of luminosity is underpredicted. This might point out that the model produce too many dwarf galaxies with large stellar mass-to-light ratios.

The choice of IMF and dust extinction model affects the predicted *colors* of galaxies. G11 uses (Chabrier 2003) IMF and a redshift dependent dust model and (Bruzual & Charlot 2003) population synthesis model. G11 shows the $u - i$ color distribution of galaxies as function of stellar mass and find that the distribution in the range $9.5 < \log M_*/\mathrm{M}_\odot < 11$ is in reasonable agreement with observations. However at lower stellar masses the model predicts larger fraction of red galaxies. H15 makes predictions of the $u-i$ color distribution, age and star formation rate of low-redshift galaxies and compare the distributions with the SDSS observations. Overall, the discrepancies seen in G11 still remains, however the distribution of low mass galaxies shows that features such as overprediction of the the number of galaxies with red colour, old ages, and low star formation rates seen in the previous versions of the model has significantly decreased. This reinsures that their new treatment of reincorporation of the ejecta, ram-pressure stripping, and star formation have made the model more accurate.

Finally, a successful model of galaxy formation has to be able to reproduced the observed *correlation function* of galaxies. G11 represents a qualitative agreement with the final data release of SDSS in predicting the autocorrelation function of galaxies. The amplitude on smaller scales is slightly higher in the model which might reflect the high $\sigma_8 = 0.9$ in MS cosmology.

2.5.2 Durham model (B06)

The Durham model is built on the treatments explained by Cole et al. (2000) and Benson et al. (2003). We use the latest version of the model implemented on MS which is laid out in Bower et al. (2006), hereafter B06.

One main general difference between the Durham model and Garching models is the definition of independent halos and classification of galaxy types. Durham model only distinguishes between satellite and central galaxies, i.e. only type 0 and type 1. This is mainly due to different methods used in B06 to implement the model on dark matter merger trees. They chop off merger trees to branches at each halo "formation event". A formation event occurs when a halo has doubled its mass since the last formation event in that branch. Also, a halo with no progenitor marks a formation event. Therefore, the properties of merger trees differ from that of Springel et al. (2005) in several respects such as the definition of independent halos and the way a descendants of a halos are identified in the merger tree. Constructing such independent merger trees has impacts on the treatment of some physical processes such as gas cooling and mergers. We summarize some aspects of the B06 model below.

Reionization Reionization completely suppresses star formation in halos with circular velocities below $50\mathrm{km\,s^{-1}}$ after the redshift at which reionization happens, that is assumed to be at $z = 6$. Benson et al. (2003) argues that with this simple choice of including reionization effect, the model matches the results of Benson et al. (2002) which studied the effect of reionization on the properties of satellite galaxies. They used the Gnedin (2000) filtering mass to determine how much gas is available in each halo at a given time. B06 argues that including this reionization recipe reproduces the observed abundance of local satellite galaxies as function of circular velocity.

Gas cooling The diffuse hot gas in the halo is assumed to have a density profile well fitted by the β model,

$$\rho_{\mathrm{hot}}(r) = \frac{\rho_0}{\left[1 + (r/r_c)^2\right]^{3\beta/2}}\,, \tag{2.76}$$

where r_c is the "core" radius and β is a parameter characterizing the slope of the density profile for radii larger than r_c and ρ_0 is the density at the centre of the halo. The β model was traditionally used to describe the density profile of hot gas emitting X-ray in clusters (Eke et al. 1998). The model parameters are set to $r_c = 0.07 R_{\rm vir}$ and $\beta = 2/3$ to match the gasdynamics simulations and the observed X-ray profile of clusters.

The gas temperature is assumed to equal the virial temperature of the halo. The cooling time is calculated similar to G11 and H15, however, the cooling radius is defined as the radius at which the $t_{\rm cool}$ equals the time since the halo was formed (the formation event). The cooling radius and cooling time are calculated and reset at each formation event. This definition implies that the cooling radius does not exceed the virial radius, therefore B06 does not distinguish between the rapid infall and cooling flow regimes. The time it takes for the gas to accrete to the centre of the halo defines the free-fall time. A free-fall radius is then defined accordingly, the radius beyond which the gas did not have enough time to fall into the central disk. The infall radius is then the minimum of the cooling and free-fall radius. The amount $M_{\rm infall}$ of gas accreting to the halo is added to the hot gas component of the halo at each formation event:

$$M_{\rm infall} = \max\left[\left(M_{\rm vir} - \Sigma_i M^i_{\rm vir}\right) f_{\rm b}, 0\right], \tag{2.77}$$

where $f_{\rm b} = 0.17$ is the universal baryon fraction and the sum extends over all progenitors of the halo (De Lucia et al. 2010).

The amount of infalling gas δM between each time interval $\delta t = t_2 - t_1$ is the mass difference enclosed in the infall radius at t_1 and t_2. The cooling rate then can be calculated as $\dot{M}_{\rm cool} = \frac{\delta M}{\delta t}$.

Star formation The star formation rate (ψ) is directly proportional to the cold gas mass available in the disk ($M_{\rm cold}$),

$$\psi = \frac{M_{\rm cold}}{\tau_*}, \tag{2.78}$$

where τ_*,

$$\tau_* = \epsilon_*^{-1} \tau_{\rm disk} \left(\frac{V_{\rm disk}}{200 {\rm km\,s^{-1}}}\right)^{\alpha_*}, \tag{2.79}$$

is related to the dynamical time of the disk $\tau_{\rm disk} \equiv r_{\rm disk}/V_{\rm disk}$ and the circular velocity of the disk at half-mass radius, $V_{\rm disk}$. ϵ_* and α_* are dimensionless parameters affecting the star formation time-scale and its dependence to the circular velocity. Matching observations of the cold gas content of spiral galaxies as a function of luminosity, B06 adopts $\epsilon_* = 0.0029$ and $\alpha_* = -1.5$.

Mergers and bulge formation When two galaxies merge, the more massive one becomes the central galaxy. The satellite galaxy is given a random orbit which decays by dynamical friction. The time it takes for the merging to be completed is modelled by Lacey & Cole (1993b):

$$\tau_{\rm merge} = f_{\rm fudge} \Theta_{\rm orbit} \tau_{\rm dyn} \frac{0.3722}{\ln(\lambda_{\rm Coulomb})} \frac{M_{\rm H}}{M_{\rm sat}}, \tag{2.80}$$

where $M_{\rm sat}$ is the mass of the satellite including the mass of the halo in which it formed, $M_{\rm H}$ is the mass of the halo in which the satellite galaxy orbits and $\ln(\lambda_{\rm Coulomb}) = \ln\left(\frac{M_{\rm halo}}{M_{\rm sat}}\right)$ is the Coulomb logarithm. The dimensionless parameter $f_{\rm fudge}$, which controls the efficiency of galaxy mergers and influences the luminosity function, is set to 1.5 . The orbital dependence of the merging time is contained in $\Theta_{\rm orbit}$ which is modelled by a log-normal distribution with a mean $\langle \log \Theta_{\rm orbit} \rangle = -0.14$ and a dispersion

$\langle(\log\Theta_{\rm orbit} - \langle\log\Theta_{\rm orbit}\rangle)^2\rangle^{1/2} = 0.26$. These values are based on Tormen (1997) who used N-body simulations of infall of satellites on clusters of galaxies to study their orbital parameters.

The fate of the merging galaxies depends on their mass (only cold gas and stellar mass) ratio. If $M_{\rm sat}/M_{\rm cen} \geq 0.3$, the merger is major, a spheroidal component is formed and all gas in galaxies is converted to stars in a starburst event. If $M_{\rm sat}/M_{\rm cen} < 0.3$, the merger is minor: the stars of the satellite are added to the bulge of the central galaxy and the cold gas is added to the disk component.

Minor and major mergers provide a channel through which a spheroidal component of the galaxy is formed. Using the conservation of energy and the virial theorem, the bulge size is computed by Eq. (2.72). Defining $M_1 \geq M_2$, M_1 and M_2 are the total masses of the two progenitors (the bulge mass and the total stellar mass) in case of major (minor) merger, respectively. One difference between the definitions used here in B06 and the one used by G11 and H15 is that here M_1 and M_2 include the contribution from the DM halos. G11 and H15 only included stellar masses of galaxies in their bulge size calculations since in their model dark matter masses of the satellites are very small at the time of merging. B06 adopts $c = 0.5$ and $\alpha_{\rm inter} = 1$ from Eq. (2.72).

In B06, bulges also can form through disk instabilities when,

$$\epsilon = V_{\rm max}\left(\frac{GM_{\rm disk}}{r_{\rm disk}}\right)^{-1/2}, \tag{2.81}$$

is less than $\epsilon_{\rm disk}$. B06 adapts $\epsilon_{\rm disk} = 0.8$ to match the observed $M_{\rm BH} - M_{\rm bluge}$ relation. This relation is similar to that of Eq. (2.73) except the factor of 3 missing here and that $V_{\rm max}$ is the circular velocity at the half-mass radius, $r_{\rm disk}$.

The size of the newly formed bulge $r_{\rm new}$ can be calculated by:

$$\frac{c_{\rm B}(M_{\rm disk} + M_{\rm bulge})^2}{r_{\rm new}} = \frac{c_{\rm B}M_{\rm bulge}^2}{r_{\rm bulge}} + \frac{c_{\rm D}M_{\rm disk}^2}{r_{\rm disk}} + f_{\rm int}\frac{M_{\rm bulge}M_{\rm disk}}{r_{\rm bulge} + r_{\rm disk}}, \tag{2.82}$$

where $M_{\rm disk}$ and $M_{\rm bulge}$ are the mass of the unstable disk and the mass of pre-exisiting bulge, respectively, and parameters are $c_{\rm B} = 0.45$, $c_{\rm D} = 0.49$ and $f_{\rm int} = 2$.

Supernovae feedback The energy released by supernovae reheats the cold gas in the disk with a rate

$$\dot{M}_{\rm reheat} = \left(\frac{V_{\rm disk}}{V_{\rm hot}}\right)^{-\alpha_{\rm hot}}\psi, \tag{2.83}$$

where ψ is the star formation rate (Eq. 2.78), $V_{\rm disk}$ is the circular velocity of the disk at the disk half-mass radius and $\alpha_{\rm hot}$ and $V_{\rm hot}$ are free parameters.

It should be noted that the model considers that the reheated gas is also available for cooling, in addition to the hot gas available in the halo. Therefore the increase in the hot gas mass available for cooling ΔM in time interval Δt is:

$$\Delta M = \frac{M_{\rm reheat}\Delta t}{\tau_{\rm reheat}}, \tag{2.84}$$

with

$$\tau_{\rm reheat} = \tau_{\rm dyn}/\alpha_{\rm reheat}, \tag{2.85}$$

being the time-scale of transferring the reheated gas to the hot gas reservoir of the halo and $\alpha_{\rm reheat}$ is a free parameter. The dynamical time of the halo is $\tau_{\rm dyn} \equiv \pi r_{\rm vir}/V_{\rm H}$, with $V_{\rm H}$ being the circular velocity of the main halo with virial radius $r_{\rm vir}$.

AGN feedback The channels through which the black hole mass increases include accretion of gas during starbursts triggered by galaxy mergers and disk instabilities. The rate of this growth is parametrized by an efficiency parameter, $F_{\rm bh}$, which indicates the fraction of the gas mass turned into stars during starbursts that is accreted to the black hole, $\Delta M_{\rm bh} = F_{\rm bh}\Delta M_*$. This parameter is set to $F_{\rm bh} = 0.5\%$ to mach the observed relation between the black hole mass and bulge mass.

In the radio mode, AGN feedback is efficient where the gas accretes from the hot atmosphere of the halo with

$$t_{\rm cool}(r_{\rm cool}) > \alpha_{\rm cool} t_{\rm ff}(r_{\rm cool})\,, \tag{2.86}$$

where $t_{\rm cool}(r_{\rm cool})$ is the cooling time at the cooling radius which equals the age of the halo, $t_{\rm ff}$ is the free-fall time, and $\alpha_{\rm cool}$ is a free parameter.

If the energy released by the accreting black hole during the radio mode counterbalances the energy radiated away from the accreting hot gaseous atmosphere, then the halo is prevented from further cooling and star formation is suppressed. Cooling is assumed to stop if the energy radiated away per unit time $L_{\rm cool}$ is lower than a fraction of the Eddington luminosity of the black hole:

$$L_{\rm cool} < \epsilon_{\rm BH} L_{\rm Edd}\,, \tag{2.87}$$

where $\epsilon_{\rm BH} = 0.5$.

Chemical evolution Stars enrich the cold gas with metals through supernovae explosions and stellar winds with a rate depending on the star-formation rate and the yield. B06 also considers the possibility that a fraction of metals produced by stars be transferred to the hot gas atmosphere. Moreover, enriched gas which later will be condensed to form stars, transfer metals to stars at rate proportional to the star formation rate and metallicity of the cold gas. Metals can also be exchanged between the cold and hot gas in the halo depending on the cooling and star-formation rates and the metallicity of each component. In Fig. 2.7, the channels through which mass and metals are exchanged between different galaxy components in B06 is shown by solid and dashed arrows, respectively.

Stellar population synthesis Spectral properties of galaxies are obtained using stellar population synthesis model by Bruzual A. & Charlot (1993) assuming a Kennicutt (1983) IMF.

Dust extinction Effects of dust on the stellar light is modelled based on the method of Ferrara et al. (1999). In this model, stars and dust have a three-dimensional distribution (stars in the disk and bulge, dust in the disk) and the dust extinction is a function of stellar light wavelength, inclination of the galaxy and the central V-band optical depth, $\tau_{\rm v0}$. B06 calculates $\tau_{\rm v0}$ for each galaxy, and assume that it is proportional to dust mass per unit area and uses an Milky Way extinction curve as the standard choice:

$$\tau_{\rm v0} \propto \frac{M_{\rm dust}}{r_{\rm disk}^2}\,. \tag{2.88}$$

Observational constraints The main observational measurement to fit the parameters in B06 is the local *luminosity function*. The luminosity function of galaxies gives the abundance of galaxies as function of their luminosity. B06 fits the blue optical B band and in near-infrared K band using the fitting parameters from Table 2.3.

With these parameters, the B06 model predicts a reasonable match to the observational local luminosity function. They argue that the enhanced treatment of AGN feedback that they implement quenches

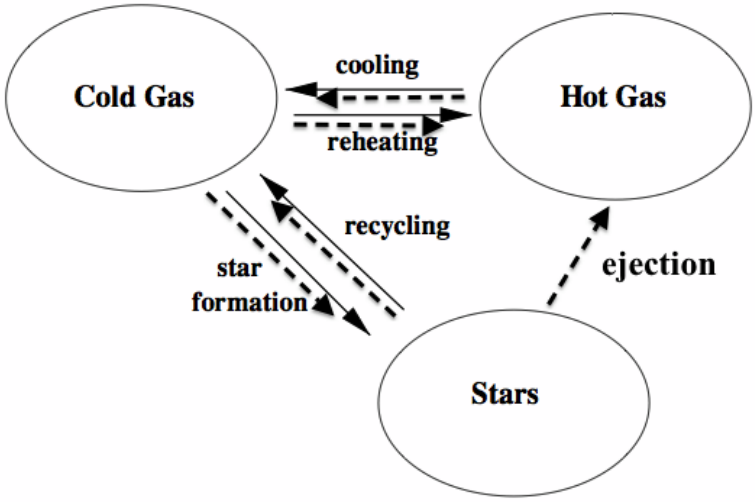

Figure 2.7: Sketch showing how mass and metals are exchanged between different baryonic components of a galaxy in the B06 model. Solid arrows refer to mass transfer and dashed arrows refer to metal transfer. Source: Cole et al. (2000).

Table 2.3: Free parameters assumed in B06 to calibrate the luminosity function.

Parameters	Constrained by:	value
$\alpha_{\rm hot}$ (Eq. 2.83)	the faint end slope	3.2
$V_{\rm hot}$ (Eq. 2.83)	the faint end slope	485 km s^{-1}
$\alpha_{\rm cool}$ (Eq. 2.86)	position of the exponential break	0.58
$\alpha_{\rm reheat}$ (Eq. 2.85)	overall normalization	0.92

the cooling flow in massive galaxies so that the number of bright massive galaxies is lowered to match the observed abundance.

The observed $M_{\rm BH} - M_{\rm bluge}$ relation at $z = 0$ is another observational constraint used to find the best fit values of $\epsilon_{\rm disk} = 0.8$ and $F_{\rm bh} = 0.5\%$. B06 finds reasonably good agreement with local observations in measurements of black hole-bulge mass relation and galaxy luminosity function. They argue that this agreement ensures that the criteria they use to suppress gas cooling which depends on the Eddington luminosity is sufficient.

Assuming a Kennicutt (1983) IMF, they also trace the evolution of the SMF. Note that in order to account for the variations in the stellar mass estimates of galaxies due to the assumed IMF, B06 claim to transform the data to the Kennicutt (1983) IMF assumed in their model. Their results match the overall amplitude of the observed mass function up to high redshift ($z \sim 4$).

CHAPTER 3

Gravitational lensing

One of the predictions of general relativity is that light is deflected from its path while passing through a gravitational field. Assuming that this gravitational field is created by a point mass object with mass M and that light from a more distant source is passing with an impact parameter ξ, general relativity predicts the deflection angle of the light ray to be:

$$\hat{\alpha} = \frac{4GM}{c^2\xi} . \tag{3.1}$$

The theory was confirmed during a solar eclipse in 1919 when the apparent position of distant stars was shifted due to their light passing around the Sun. In this case, the Sun acted as a gravitational lens.

An image of a gravitational lensing effect is shown in Fig. 3.1. Features such as arcs seen in the picture are images of background sources stretched tangentially with respect to the centre of the foreground object, which in this case is a cluster of galaxies Abell 2218. When such features are observed we are in the *strong gravitational lensing* regime, which has been observed for the first time in 1979 as a twin quasar with the same spectra (Walsh et al. 1979). On the other hand, distortions are weaker in the outskirts of clusters as well as in the vicinity of lower mass objects such as galaxies. These weaker effects belong to the *weak gravitational lensing* regime. To obtain a weak lensing signal a statistical approach is required. For example in the case of weak lensing by galaxies called *galaxy-galaxy lensing*, the foreground and background objects are both galaxies and the lensing measurement is obtained by considering a large sample of galaxies. The first detection of galaxy-galaxy lensing was reported by Brainerd et al. (1996).

In this chapter we discuss some general properties of lens systems before focusing on the weak gravitational lensing. The reader is referred to Schneider et al. (1999), Schneider (2009b) and Schneider et al. (2006) for more detailed reviews.

3.1 Lens equation

The geometry of a typical lens system is depicted in Fig. 3.2. Light from a source at distance of D_s from the observer is deflected (by an angle $\hat{\boldsymbol{\alpha}}$) by an intervening mass concentration, the lens. The true angular position of the source on the sky, $\boldsymbol{\beta}$, is not an observable. However, the observable is $\boldsymbol{\theta}$, the

angular position of the image and is related to $\hat{\boldsymbol{\alpha}}$ through the lens equation:

$$\boldsymbol{\beta} = \boldsymbol{\theta} - \frac{D_{\mathrm{ds}}}{D_{\mathrm{s}}}\,\hat{\boldsymbol{\alpha}}(D_{\mathrm{d}}\boldsymbol{\theta}) \equiv \boldsymbol{\theta} - \boldsymbol{\alpha}(\boldsymbol{\theta})\,. \tag{3.2}$$

$\boldsymbol{\eta} = D_{\mathrm{s}}\,\boldsymbol{\beta}$ and $\boldsymbol{\xi} = D_{\mathrm{d}}\,\boldsymbol{\theta}$ are two dimensional positions of the source on the source and lens planes and

$$\boldsymbol{\alpha}(\boldsymbol{\theta}) = \frac{D_{\mathrm{ds}}}{D_{\mathrm{s}}}\,\hat{\boldsymbol{\alpha}}(D_{\mathrm{d}}\boldsymbol{\theta})\,, \tag{3.3}$$

is the scaled deflection angle.

A mass distribution for which the extend along the line-of-sight is negligible compared to distances between the observer, the source and the lens is called a *thin lens*. For such a system, the light ray in the vicinity of the lens can be approximated as a straight line and the total deflection angle is the sum of the deflection angles by individual point mass elements constituting the lens. For a mass element $\mathrm{d}m = \mathrm{d}^2\xi^{'}\,\mathrm{d}r_3^{'}\rho(\boldsymbol{r}^{'})$ with position $\boldsymbol{r}^{'} = (\xi_1^{'}, \xi_2^{'}, r_3^{'})$ with $r_3^{'}$ being the component along the line-of-sight, the deflection angle is:

$$\hat{\boldsymbol{\alpha}}(\boldsymbol{\xi}) = \frac{4G}{\mathrm{c}^2}\int \mathrm{d}^2\xi^{'} \int \mathrm{d}r_3^{'}\,\rho(\xi_1^{'}, \xi_2^{'}, r_3^{'})\,\frac{\boldsymbol{\xi} - \boldsymbol{\xi}^{'}}{\left|\boldsymbol{\xi} - \boldsymbol{\xi}^{'}\right|^2}\,. \tag{3.4}$$

By defining the surface mass density as the projection of the mass density onto the lens plane:

$$\Sigma(\boldsymbol{\xi}) \equiv \int \mathrm{d}r_3^{'}\,\rho(\xi_1^{'}, \xi_2^{'}, r_3^{'})\,, \tag{3.5}$$

we can express Eq. (3.4) in terms of the scaled deflection angle,

$$\boldsymbol{\alpha}(\boldsymbol{\theta}) = \frac{1}{\pi}\int \mathrm{d}^2\theta'\,\kappa(\boldsymbol{\theta}')\frac{\boldsymbol{\theta} - \boldsymbol{\theta}'}{|\boldsymbol{\theta} - \boldsymbol{\theta}'|^2}\,. \tag{3.6}$$

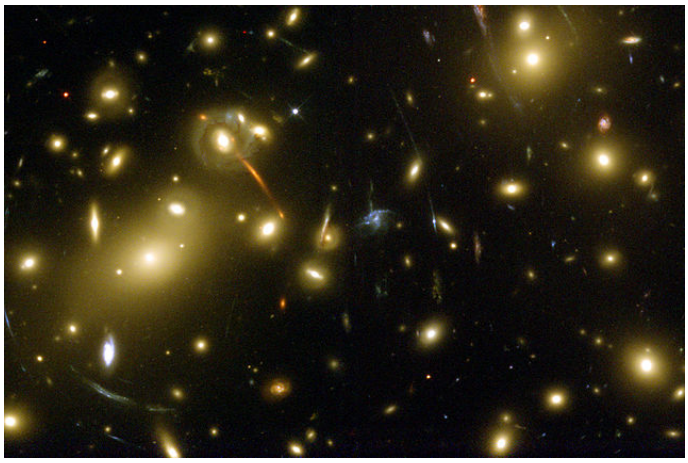

Figure 3.1: Gravitational lensing caused by the cluster of galaxies Abell 2218. Giant arcs and distortions observed in the image of background sources can be clearly seen in this NASA's Hubble Space Telescope image. Credit: NASA (www.nasa.gov)

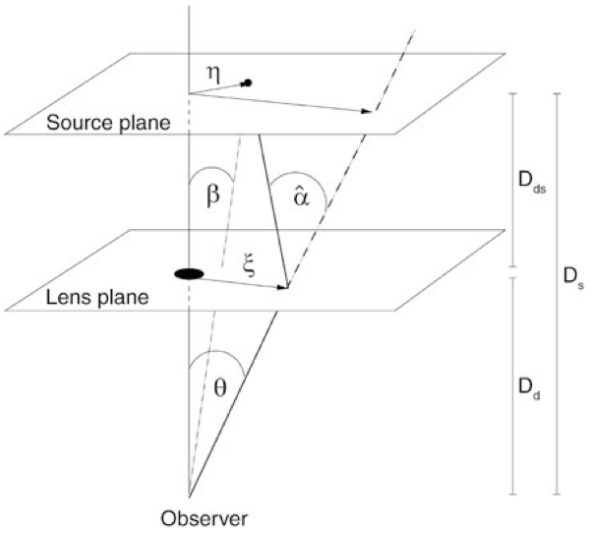

Figure 3.2: Sketch showing the geometry of a lens system. Light from a source at the source plane is deflected by the presence of an intervening matter distribution at the lens plane. Figure adopted from Schneider (2009b).

The dimensionless surface mass density or *convergence* is defined as,

$$\kappa(\boldsymbol{\theta}) \equiv \frac{\Sigma(D_\mathrm{d}\boldsymbol{\theta})}{\Sigma_\mathrm{cr}} \qquad \text{with} \qquad \Sigma_\mathrm{cr} = \frac{c^2}{4\pi G}\frac{D_s}{D_d D_{ds}}\,, \tag{3.7}$$

where Σ_cr is called the critical surface mass density.

Using $\nabla \ln|\boldsymbol{\theta}| = \boldsymbol{\theta}/|\boldsymbol{\theta}|^2$, the scaled deflection angle can be written in terms of the deflection potential, $\psi(\boldsymbol{\theta})$:

$$\begin{aligned}\boldsymbol{\alpha}(\boldsymbol{\theta}) &= \frac{1}{\pi}\int \mathrm{d}^2\theta'\,\kappa(\boldsymbol{\theta}')\nabla \ln\left|\boldsymbol{\theta}-\boldsymbol{\theta}'\right| \\ &= \nabla\psi(\boldsymbol{\theta})\,.\end{aligned} \tag{3.8}$$

In addition since $\nabla^2 \ln|\boldsymbol{\theta}| = 2\pi\delta_\mathrm{D}(\theta)$, Eq. (3.8) leads to:

$$\nabla^2\psi = 2\kappa\,. \tag{3.9}$$

The lens equation (Eq. 3.2) corresponds to a mapping from the lens plane to the source plane. The Jacobian of this mapping is given by

$$A_{ij}(\boldsymbol{\theta}) = \frac{\partial\boldsymbol{\beta}}{\partial\boldsymbol{\theta}} = \delta_{ij} - \frac{\partial^2\psi(\boldsymbol{\theta})}{\partial\theta_i\partial\theta_j}\,, \tag{3.10}$$

where δ_{ij} denotes the Kronecker delta. Defining the *shear* components γ_1 and γ_2 in the Cartesian reference frame and the notation $\psi_{,ij} = \partial^2\psi(\boldsymbol{\theta})/\partial\theta_i\partial\theta_j$, the Jacobian matrix can be written as

$$A(\boldsymbol{\theta}) = \begin{pmatrix} 1-\kappa-\gamma_1 & -\gamma_2 \\ -\gamma_2 & 1-\kappa+\gamma_1 \end{pmatrix} \tag{3.11}$$

with

$$\gamma_1 = \frac{1}{2}(A_{22} - A_{11}) = \frac{1}{2}(\psi_{,11} - \psi_{,22})\,, \tag{3.12}$$
$$\gamma_2 = -A_{12} = \psi_{,12}\,.$$

The shear is a complex quantity:

$$\gamma = \gamma_1 + \mathrm{i}\gamma_2 = |\gamma|\,\mathrm{e}^{2\mathrm{i}\varphi}\,, \tag{3.13}$$

and is related to the *reduced shear* g through

$$g = \frac{\gamma}{1-\kappa} = g_1 + \mathrm{i}g_2\,. \tag{3.14}$$

The Jacobian matrix can then be rewritten in terms of the reduced shear,

$$A(\boldsymbol{\theta}) = (1-\kappa)\begin{pmatrix} 1-g_1 & -g_2 \\ -g_2 & 1+g_1 \end{pmatrix}. \tag{3.15}$$

Similar to the shear, the reduced shear is a complex quantity, $g = g_1 + \mathrm{i}g_2 = |g|\,e^{2\mathrm{i}\varphi}$, with an amplitude specifying a distortion in the observed image of the source and a phase corresponding to the direction of this distortion.

3.2 Weak gravitational lensing

In the weak gravitational lensing regime, $\kappa \ll 1$ and distortions in the source images are weak. A lensing signal is then obtained by considering an average signal of many lens systems. It can be shown that the observed image of a circular source, such as a galaxy, is distorted to an ellipse (see Fig. 3.3). However, galaxies are not perfectly circular. In weak gravitational lensing, the expectation value of the observed ellipticity, ϵ^{obs}, is then the intrinsic ellipticity ϵ^{int} (the ellipticity in the absence of lensing) plus the reduced shear due to lensing:

$$\langle\epsilon^{\mathrm{obs}}\rangle = \langle\epsilon^{\mathrm{int}}\rangle + \langle g\rangle\,. \tag{3.16}$$

To estimate the reduced shear, it is assumed that intrinsic ellipticity of galaxies have random orientations, therefore when averaging over many galaxies, the term $\langle\epsilon^{\mathrm{int}}\rangle$ can be neglected. This assumption

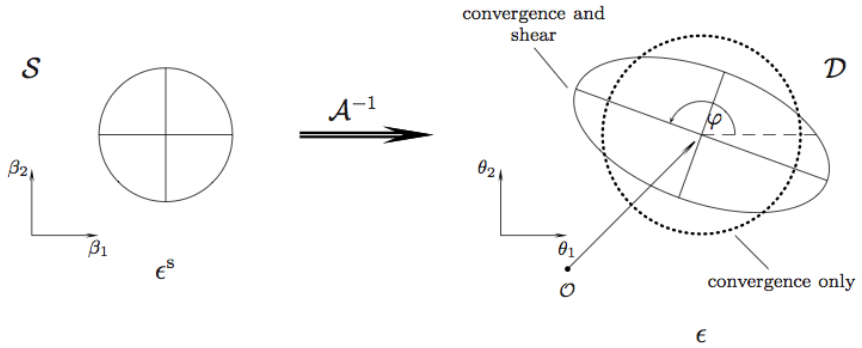

Figure 3.3: Figure shows a circular source in the presence of a lens is observed as an ellipse. The size of the image is affected by the convergence and the axis ratio and orientation of the ellipse by the shear. Figure adopted from Schneider (2009b).

then leads to an important conclusion that in weak gravitational lensing observed ellipticities of galaxies are unbiased estimate of the reduced shear. Since in weak lensing regime $\kappa \ll 1$, Eq. (3.14) implies $g \approx \gamma$ and shear can be estimated by the observed ellipticities.

In practice, it is more convenient to define shear with respect to a rotated reference frame. Given a direction φ, the real and imaginary parts of the rotated shear can be defined:

$$\gamma_t = -\mathrm{Re}[\gamma e^{(-2i\varphi)}] \qquad \text{and} \qquad \gamma_\times = -\mathrm{Im}[\gamma e^{(-2i\varphi)}]\,. \tag{3.17}$$

Since κ and γ are both second derivatives of the deflection potential (Eqs. 3.9 and 3.12), one can write their relation as

$$\tilde{\gamma}(\boldsymbol{\ell}) = \left(\frac{\ell_1^2 - \ell_2^2}{|\boldsymbol{\ell}|^2} + 2i\frac{\ell_1\ell_2}{|\boldsymbol{\ell}|^2}\right)\tilde{\kappa}(\boldsymbol{\ell}) = \frac{(\ell_1 + i\ell_2)^2}{|\boldsymbol{\ell}|^2}\tilde{\kappa}(\boldsymbol{\ell}) = e^{2i\phi_\ell}\tilde{\kappa}(\boldsymbol{\ell}) \tag{3.18}$$

in Fourier space (Kaiser & Squires 1993). Here ϕ_ℓ is the polar angle of $\boldsymbol{\ell}$ and we used the Fourier transform of $\tilde{\kappa} = -|\boldsymbol{\ell}|^2\,\tilde{\psi}/2$ and $\tilde{\gamma}_1 = -(\ell_1^2 - \ell_2^2)\tilde{\psi}/2$ and $\tilde{\gamma}_2 = -\ell_1\ell_2\tilde{\psi}$.

3.2.1 Light propagation in an inhomogeneous Universe

Light rays emitted from a distant source are continuously deflected by the large scale structure in the Universe. The thin lens approximation appears not feasible in this case. However, using the so-called *Born approximation*, one can consider each time a deflection occurs separately from the other deflection events and assume that part of the Universe is decoupled from the rest and apply the thin lens algorithm. The total deflection and distortion is then the sum of all these events occurring along the path of the light ray. The convergence at a given direction is then the sum of convergence of all thin lenses along that direction and can be written as (for derivation see Bartelmann & Schneider 2001)

$$\begin{aligned}\kappa(\boldsymbol{\theta}) &= \int \mathrm{d}\chi\, p_\mathrm{s}(\chi)\kappa(\boldsymbol{\theta},\chi) \\ &= \frac{3H_0^2\Omega_\mathrm{m}}{2c^2}\int_0^{\chi_h}\mathrm{d}\chi\, g(\chi) f_\mathrm{K}(\chi)\frac{\delta(f_\mathrm{K}(\chi)\boldsymbol{\theta},\chi)}{a(\chi)}\,,\end{aligned} \tag{3.19}$$

with

$$g(\chi) = \int_\chi^{\chi_\mathrm{h}}\mathrm{d}\chi'\, p_\mathrm{s}(\chi')\frac{f_\mathrm{K}(\chi'-\chi)}{f_\mathrm{K}(\chi')}\,, \tag{3.20}$$

where χ_h is the comoving horizon size and $g(\chi)$ is the lensing efficiency factor weighted with source redshift distribution $p_\mathrm{s}(\chi)\mathrm{d}\chi$. The two-point statistics of the convergence field is expressed in terms of the power spectrum (Kaiser 1998)

$$P_{\kappa\kappa}(\ell) = \frac{9H_0^4\Omega_\mathrm{m}^2}{4c^4}\int_0^{\chi_\mathrm{h}}\mathrm{d}\chi\frac{g^2(\chi)}{a^2(\chi)}P_{\delta\delta}\left(\frac{\ell}{f_\mathrm{K}(\chi)},\chi\right), \tag{3.21}$$

where the matter power spectrum is defined by the correlator in Eq. (2.42).

3.2.2 Galaxy-galaxy lensing

The galaxy distribution does not follow the matter distribution: galaxies form preferentially in high density regions of matter density field. The number density field of galaxies is related to the matter density field through what we call the bias parameter. In a simple case of *linear deterministic* biasing,

the bias parameter b is defined by $\delta_{\rm g} = b\delta$. The three-dimensional number density contrast of galaxy distribution $\delta_{\rm g}$ is defined as:

$$\delta_{\rm g}(\boldsymbol{x},\chi) := \frac{n_{\rm g}(\boldsymbol{x},\chi) - \bar{n}_{\rm g}(\chi)}{\bar{n}_{\rm g}(\chi)}\,, \tag{3.22}$$

in analogy to the matter density contrast. Here, $n_{\rm g}(\boldsymbol{x},\chi)$ denotes the number density of galaxies at comoving position $\boldsymbol{x}$ and $\bar{n}_{\rm g}(\chi)$ is mean number density of galaxies. The projection of the (mean) number density field of a population for foreground galaxies at position θ on the sky is then given by

$$N(\boldsymbol{\theta}) = \int {\rm d}\chi\, v(\chi)\, n_{\rm g}(f_{\rm K}(\chi)\boldsymbol{\theta},\chi)\,, \tag{3.23}$$

and

$$\bar{N} = \int {\rm d}\chi\, v(\chi)\, \bar{n}_{\rm g}(\chi)\,, \tag{3.24}$$

where $v(\chi)$ is a selection function accounting for the fraction of galaxies included in the sample. For a foreground galaxy distribution, the selection function is related to probability distribution $p_{\rm f}$ in comoving distance through $p_{\rm f}(\chi) = v(\chi)\bar{n}_{\rm g}(\chi)/\bar{N}$. Therefore, the relation between N and $\bar{N}$ can be written as

$$N(\boldsymbol{\theta}) = \bar{N}\left[1 + \int {\rm d}\chi\, p_{\rm f}(\chi)\, \delta_{\rm g}(f_{\rm K}(\chi)\boldsymbol{\theta},\chi)\right]. \tag{3.25}$$

The fractional number density contrast of foreground galaxies on the sky is then defined as

$$\kappa_{\rm g}(\boldsymbol{\theta}) := \frac{N(\boldsymbol{\theta}) - \bar{N}}{\bar{N}} = \int {\rm d}\chi\, p_{\rm f}(\chi)\, \delta_{\rm g}(f_{\rm K}(\chi)\kappa_{\rm g}\boldsymbol{\theta},\chi)\,. \tag{3.26}$$

The galaxy power spectrum is defined by

$$\left\langle \tilde{\delta}_{\rm g}(\boldsymbol{k},\chi)\, \tilde{\delta}^{*}_{\rm g}(\boldsymbol{k}',\chi)\right\rangle = (2\pi)^3 \delta_{\rm D}(\boldsymbol{k}-\boldsymbol{k}') P_{\rm gg}(|\boldsymbol{k}|,\chi)\,, \tag{3.27}$$

which is related to the matter power spectrum through the bias parameter by

$$P_{\rm gg}(|\boldsymbol{k}|,\chi) = b^2(|\boldsymbol{k}|,\chi) P_{\delta\delta}(|\boldsymbol{k}|,\chi)\,. \tag{3.28}$$

The projected galaxy power spectrum at angular scales $2\pi/\ell$ is obtained by integrating the $P_{\rm gg}(|\boldsymbol{k}|,\chi)$ at scales $f_{\rm K}(\chi)(2\pi/\ell)$ along χ,

$$P_{\rm gg}(\ell) = \int_0^{\chi_{\rm h}} {\rm d}\chi \frac{p_{\rm f}^2(\chi)}{f_{\rm K}^2(\chi)}\, b^2(k,\chi)\, P_{\delta\delta}\,(k,\chi)\,, \tag{3.29}$$

where $\chi_{\rm h}$ is the comoving horizon size and $\boldsymbol{k} = \boldsymbol{\ell}/f_{\rm K}(\chi)$. The cross-power spectrum,

$$\left\langle \tilde{\delta}(\boldsymbol{k},\chi)\, \tilde{\delta}^{*}_{\rm g}(\boldsymbol{k}',\chi)\right\rangle = (2\pi)^3 \delta_{\rm D}(\boldsymbol{k}-\boldsymbol{k}') P_{\delta{\rm g}}(|\boldsymbol{k}|,\chi) \tag{3.30}$$

is related to the matter power spectrum through

$$P_{\delta{\rm g}}(|\boldsymbol{k}|,\chi) = b(|\boldsymbol{k}|,\chi) r(|\boldsymbol{k}|,\chi) P_{\delta\delta}(|\boldsymbol{k}|,\chi)\,, \tag{3.31}$$

where the correlation coefficient $r(|\boldsymbol{k}|,\chi)$ was defined. The projection of $P_{\delta g}(|\boldsymbol{k}|,\chi)$ along the line-of-sight is related to the matter power spectrum by

$$P_{\kappa g}(\ell) = \frac{3H_0^2\Omega_m}{2c^2}\int_0^{\chi_h} d\chi \frac{g(\chi)p_f(\chi)}{f_K(\chi)a(\chi)}\, b(k,\chi)\, r(k,\chi)\, P_{\delta\delta}(k,\chi)\,. \tag{3.32}$$

Galaxy-galaxy lensing (GGL) is the study of the relation between κ_g and κ. Observed images of distant background galaxies are distorted by the gravitational potential of foreground galaxies. This distortion is a tangential alignment of the ellipticities or the shear of the background galaxy with respect to the foreground lensing galaxy. The GGL signal determines the correlation between this tangential alignment and the position of foreground galaxies (e.g. Hoekstra et al. 2002). To carry out GGL measurements, the galaxy sample is divided into foreground and background populations (for example by means of redshift information) and the pairs of foreground-background galaxies are selected according to their angular separation. The correlation of the tangential shear pattern in the observed image of background galaxy and the position of the foreground galaxy is measured for each galaxy pair. The average of this correlation for all pairs in the same angular separation bin then yields the GGL signal in that bin:

$$\langle\gamma_t\rangle(\theta) \equiv \left\langle \kappa_g(\boldsymbol{\vartheta})\gamma_t(\boldsymbol{\vartheta}+\boldsymbol{\theta};\varphi)\right\rangle\,, \tag{3.33}$$

where φ is the polar angle of the connection vector $\boldsymbol{\theta}$. Similar to the matter density field, the galaxy density field is a homogeneous random field, therefore Eq. (3.33) can be rewritten as

$$\langle\gamma_t\rangle(\theta) = \left\langle \kappa_g(0)\gamma_t(\boldsymbol{\theta};\varphi)\right\rangle\,, \tag{3.34}$$

and calculated by

$$\begin{aligned}
\langle\gamma_t\rangle(\theta) &= \left\langle \kappa_g(0)\gamma_t(\boldsymbol{\theta};\varphi)\right\rangle + \mathrm{i}\left\langle \kappa_g(0)\gamma_\times(\boldsymbol{\theta};\varphi)\right\rangle \\
&= -\mathrm{e}^{-2\mathrm{i}\varphi}\left\langle \kappa_g(0)\gamma(\boldsymbol{\theta})\right\rangle \\
&= -\int\frac{d^2\ell}{(2\pi)^2}\int\frac{d^2\ell'}{(2\pi)^2}\mathrm{e}^{-\mathrm{i}\boldsymbol{\theta}\cdot\boldsymbol{\ell}'}\mathrm{e}^{-2\mathrm{i}\varphi}\left\langle \tilde\kappa_g(\boldsymbol{\ell})\tilde\gamma(\boldsymbol{\ell}')\right\rangle \\
&= -\int\frac{d^2\ell}{(2\pi)^2}\int\frac{d^2\ell'}{(2\pi)^2}\mathrm{e}^{-\mathrm{i}\boldsymbol{\theta}\cdot\boldsymbol{\ell}'}\mathrm{e}^{2\mathrm{i}(\phi_\ell-\varphi)}\left\langle \tilde\kappa_g(\boldsymbol{\ell})\tilde\kappa(\boldsymbol{\ell}')\right\rangle\,.
\end{aligned} \tag{3.35}$$

In the second step we set the imaginary part of the correlator $\langle\gamma_\times(\boldsymbol{\theta})\rangle$ to zero (a non-vanishing $\langle\gamma_\times(\boldsymbol{\theta})\rangle$ would violate the parity invariance and implies a preferred sense of rotation on the sky). In the next steps we transformed κ and γ to Fourier space and used the Kaiser-Squires relation (Eq. 3.18).

Mean tangential shear on circles

It can be shown that the average tangential shear on concentric circles of radius θ is related to the mean convergence inside the circle and the azimuthally-averaged convergence at θ:

$$\langle\gamma_t\rangle(\theta) = \bar\kappa(<\theta) - \langle\kappa(\theta)\rangle\,. \tag{3.36}$$

A derivation of this relation can be found in Schneider (2005).

3.2.3 Galaxy-galaxy-galaxy lensing

Two classes of correlation functions can be defined when studying galaxy-galaxy-galaxy lensing (G3L): galaxy-shear-shear and galaxy-galaxy-shear. The galaxy-shear-shear three-point correlation function (3PCF) describes the cross-correlation between the shear of two background galaxies at positions $\boldsymbol{\theta}_1$ and $\boldsymbol{\theta}_2$ and the position of a foreground galaxy at $\boldsymbol{\theta}_3$ on the sky.

$$G_+(\boldsymbol{\vartheta}_1, \boldsymbol{\vartheta}_2) = G_+(\vartheta_1, \vartheta_2, \phi_3) = \left\langle \gamma(\boldsymbol{\theta}_1; \varphi_1)\gamma^*(\boldsymbol{\theta}_2; \varphi_2)\kappa_\mathrm{g}(\boldsymbol{\theta}_3) \right\rangle , \tag{3.37}$$

$$G_-(\boldsymbol{\vartheta}_1, \boldsymbol{\vartheta}_2) = G_-(\vartheta_1, \vartheta_2, \phi_3) = \left\langle \gamma(\boldsymbol{\theta}_1; \varphi_1)\gamma(\boldsymbol{\theta}_2; \varphi_2)\kappa_\mathrm{g}(\boldsymbol{\theta}_3) \right\rangle , \tag{3.38}$$

where $\boldsymbol{\vartheta}_i = \boldsymbol{\theta}_i - \boldsymbol{\theta}_3$ with $i = 1, 2$ denotes the separation between the two foreground galaxies and the background galaxy. The geometrical configuration of these galaxies is sketched in the left panel of Fig. 3.4. To obtain practical estimators for the 3PCFs, Schneider & Watts (2005) introduced modified correlators in the terms of number density of galaxies as

$$\begin{aligned} \hat{G}_+(\vartheta_1, \vartheta_2, \phi_3) &\equiv \frac{1}{\bar{N}} \langle \gamma(\boldsymbol{\theta}_1; \varphi_1)\gamma^*(\boldsymbol{\theta}_2; \varphi_2)N(\boldsymbol{\theta}_3) \rangle \\ &= G_+(\vartheta_1, \vartheta_2, \phi_3) + \langle \gamma(\boldsymbol{\theta}_1; \varphi_1)\gamma^*(\boldsymbol{\theta}_2; \varphi_2) \rangle , \end{aligned} \tag{3.39}$$

$$\begin{aligned} \hat{G}_-(\vartheta_1, \vartheta_2, \phi_3) &\equiv \frac{1}{\bar{N}} \langle \gamma(\boldsymbol{\theta}_1; \varphi_1)\gamma(\boldsymbol{\theta}_2; \varphi_2)N(\boldsymbol{\theta}_3) \rangle \\ &= G_-(\vartheta_1, \vartheta_2, \phi_3) + \langle \gamma(\boldsymbol{\theta}_1; \varphi_1)\gamma(\boldsymbol{\theta}_2; \varphi_2) \rangle . \end{aligned} \tag{3.40}$$

In the second step, we used Eq. (3.26). Due to statistical properties of the density fields, the $\hat{G}_\pm$ correlators depends only on the dimensions of the triangles made by triplets of galaxies (two sources and a lens galaxy). Estimators for $\hat{G}_\pm$ can be obtained by finding triangles with similar geometry and sum the products of shears of background galaxies. The $G_\pm$ correlators can then be measured by subtracting the second-order shear correlation function. Therefore the signature of galaxy-shear-shear correlation function is the excess of shear two-point correlation function around lens galaxies. Another class of 3PCF is the galaxy-galaxy-shear correlation function which correlates the positions of two lens galaxies

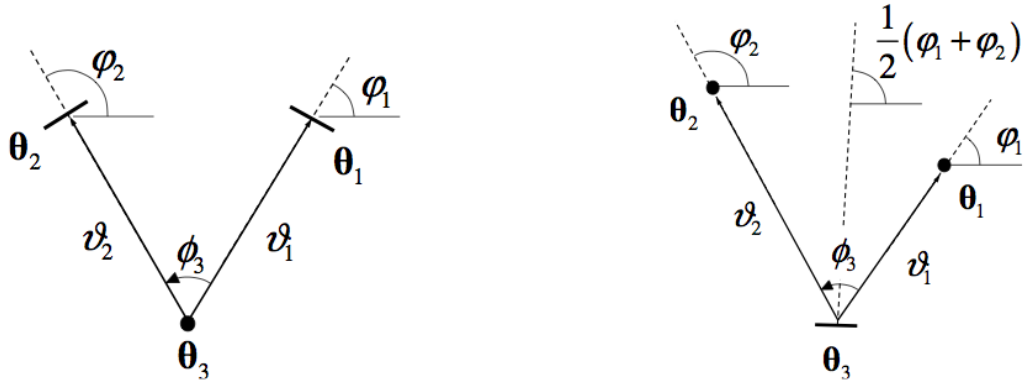

Figure 3.4: Two possible configurations of triplets of galaxies corresponding to $G_\pm$ (left panel) and G (right panel). Source: Schneider & Watts (2005)

with the shear at the position of a source galaxy with the geometry shown in the right panel of Fig. 3.4,

$$\mathcal{G}(\boldsymbol{\vartheta}_1, \boldsymbol{\vartheta}_2) = \mathcal{G}(\vartheta_1, \vartheta_2, \phi_3) = \left\langle \kappa_\mathrm{g}(\boldsymbol{\theta}_1)\, \kappa_\mathrm{g}(\boldsymbol{\theta}_2)\, \gamma\left(\boldsymbol{\theta}_3; \frac{\varphi_1 + \varphi_2}{2}\right)\right\rangle . \tag{3.41}$$

It should be noted that the shear is rotated in the direction bisecting the angle ϕ_3 between two lens galaxies. The modified correlator, $\hat{\mathcal{G}}$, is defined by:

$$\begin{aligned}\hat{\mathcal{G}}(\vartheta_1, \vartheta_2, \phi_3) &\equiv \frac{1}{\bar{N}^2}\left\langle N(\boldsymbol{\theta}_1)\, N(\boldsymbol{\theta}_2)\, \gamma\left(\boldsymbol{\theta}_3; \frac{\varphi_1 + \varphi_2}{2}\right)\right\rangle \\ &= \mathcal{G}(\vartheta_1, \vartheta_2, \phi_3) + \langle\gamma_\mathrm{t}\rangle\,(\vartheta_1)\mathrm{e}^{-\mathrm{i}\phi_3} + \langle\gamma_\mathrm{t}\rangle\,(\vartheta_2)\mathrm{e}^{\mathrm{i}\phi_3} .\end{aligned} \tag{3.42}$$

In the last step we used Eq. (3.26) and,

$$\gamma\left(\boldsymbol{\theta}_3; \frac{\varphi_1 + \varphi_2}{2}\right) = \gamma\,(\boldsymbol{\theta}_3; \varphi_1)\,\mathrm{e}^{2\mathrm{i}\left(\varphi_1 - \frac{\varphi_1+\varphi_2}{2}\right)} = \gamma\,(\boldsymbol{\theta}_3; \varphi_1)\,\mathrm{e}^{-\mathrm{i}\phi_3} , \tag{3.43}$$

$$\gamma\left(\boldsymbol{\theta}_3; \frac{\varphi_1 + \varphi_2}{2}\right) = \gamma\,(\boldsymbol{\theta}_3; \varphi_2)\,\mathrm{e}^{2\mathrm{i}\left(\varphi_2 - \frac{\varphi_1+\varphi_2}{2}\right)} = \gamma\,(\boldsymbol{\theta}_3; \varphi_2)\,\mathrm{e}^{\mathrm{i}\phi_3} . \tag{3.44}$$

If one considers triplets of galaxies, two lenses and a source, that have similar dimensions (i.e. that fall into same $[\vartheta_1, \vartheta_2, \phi_3]$ bin) and one sums over the shears of the background galaxies, one gets an estimate of $\hat{\mathcal{G}}/\left(1 + w_\mathrm{gg}(|\boldsymbol{\theta}_2 - \boldsymbol{\theta}_1|)\right)$. In this expression, $w_\mathrm{gg}(|\Delta\boldsymbol{\theta}|)$ is the angular clustering of galaxies defined as

$$w_\mathrm{gg}(|\Delta\boldsymbol{\theta}|) \equiv \left\langle \kappa_\mathrm{g}(\boldsymbol{\theta})\kappa_\mathrm{g}(\boldsymbol{\theta} + \Delta\boldsymbol{\theta})\right\rangle . \tag{3.45}$$

The third-order spectra of the three dimensional matter and galaxy distribution are defined as

$$\begin{aligned}\left\langle\tilde{\delta}(\boldsymbol{k}_1)\tilde{\delta}(\boldsymbol{k}_2)\tilde{\delta}(\boldsymbol{k}_3)\right\rangle &= (2\pi)^3\delta_\mathrm{D}(\boldsymbol{k}_1 + \boldsymbol{k}_2 + \boldsymbol{k}_3)\boldsymbol{B}_{\delta\delta\delta}(\boldsymbol{k}_1, \boldsymbol{k}_2, \boldsymbol{k}_3; \chi) , \\ \left\langle\tilde{\delta}_\mathrm{g}(\boldsymbol{k}_1)\tilde{\delta}_\mathrm{g}(\boldsymbol{k}_2)\tilde{\delta}_\mathrm{g}(\boldsymbol{k}_3)\right\rangle &= (2\pi)^3\delta_\mathrm{D}(\boldsymbol{k}_1 + \boldsymbol{k}_2 + \boldsymbol{k}_3)\boldsymbol{B}_{\mathrm{ggg}}(\boldsymbol{k}_1, \boldsymbol{k}_2, \boldsymbol{k}_3; \chi) , \\ \left\langle\tilde{\delta}(\boldsymbol{k}_1)\tilde{\delta}(\boldsymbol{k}_2)\tilde{\delta}_\mathrm{g}(\boldsymbol{k}_3)\right\rangle &= (2\pi)^3\delta_\mathrm{D}(\boldsymbol{k}_1 + \boldsymbol{k}_2 + \boldsymbol{k}_3)\boldsymbol{B}_{\delta\delta\mathrm{g}}(\boldsymbol{k}_1, \boldsymbol{k}_2; \boldsymbol{k}_3; \chi) , \\ \left\langle\tilde{\delta}_\mathrm{g}(\boldsymbol{k}_1)\tilde{\delta}_\mathrm{g}(\boldsymbol{k}_2)\tilde{\delta}(\boldsymbol{k}_3)\right\rangle &= (2\pi)^3\delta_\mathrm{D}(\boldsymbol{k}_1 + \boldsymbol{k}_2 + \boldsymbol{k}_3)\boldsymbol{B}_{\mathrm{gg}\delta}(\boldsymbol{k}_1, \boldsymbol{k}_2; \boldsymbol{k}_3; \chi) .\end{aligned} \tag{3.46}$$

The statistical homogeneity and isotropy of the random field implies that the correlators vanish unless the three k-vectors form a closed triangle (ensured with the delta function) and that the bispectrum depends only on the moduli of the k-vectors and their enclosed angle.

The third-order bias parameter b_3 and the galaxy-mass correlation coefficients r_1 and r_2 are introduced so that the galaxy bispectrum $\boldsymbol{B}_\mathrm{ggg}$ and the two cross-bispectra, $\boldsymbol{B}_{\mathrm{gg}\delta}$ and $\boldsymbol{B}_{\delta\delta\mathrm{g}}$ are related to the dark matter bispectrum $\boldsymbol{B}_{\delta\delta\delta}$:

$$\begin{aligned}\boldsymbol{B}_{\mathrm{ggg}}(\boldsymbol{k}_1, \boldsymbol{k}_2, \boldsymbol{k}_3; \chi) &= b_3^3(\boldsymbol{k}_1, \boldsymbol{k}_2, \boldsymbol{k}_3; \chi)\boldsymbol{B}_{\delta\delta\delta}(\boldsymbol{k}_1, \boldsymbol{k}_2, \boldsymbol{k}_3; \chi) , \\ \boldsymbol{B}_{\mathrm{gg}\delta}(\boldsymbol{k}_1, \boldsymbol{k}_2, \boldsymbol{k}_3; \chi) &= b_3^2(\boldsymbol{k}_1, \boldsymbol{k}_2, \boldsymbol{k}_3; \chi)r_2(\boldsymbol{k}_1, \boldsymbol{k}_2, \boldsymbol{k}_3; \chi)\boldsymbol{B}_{\delta\delta\delta}(\boldsymbol{k}_1, \boldsymbol{k}_2, \boldsymbol{k}_3; \chi) , \\ \boldsymbol{B}_{\delta\delta\mathrm{g}}(\boldsymbol{k}_1, \boldsymbol{k}_2, \boldsymbol{k}_3; \chi) &= b_3(\boldsymbol{k}_1, \boldsymbol{k}_2, \boldsymbol{k}_3; \chi)r_1(\boldsymbol{k}_1, \boldsymbol{k}_2, \boldsymbol{k}_3; \chi)\boldsymbol{B}_{\delta\delta\delta}(\boldsymbol{k}_1, \boldsymbol{k}_2, \boldsymbol{k}_3; \chi) .\end{aligned} \tag{3.47}$$

It should be noted that in the case of linear deterministic biasing, $b_3 = b$ and $r_2 = 1 = r_1$. The projected bispectra are related to the three-dimensional bispectra through Limber's equations by integration along χ and can be written as

$$
\begin{aligned}
b_{\kappa\kappa\kappa}(\boldsymbol{\ell}_1,\boldsymbol{\ell}_2,\boldsymbol{\ell}_3) &= \frac{27H_0^6\Omega_m^3}{8c^6}\int \mathrm{d}\chi\,\frac{g^3(\chi)}{f_\mathrm{K}(\chi)a^3(\chi)}\,B_{\delta\delta\delta}(\boldsymbol{k}_1,\boldsymbol{k}_2,\boldsymbol{k}_3;\chi)\,,\\
b_{\kappa\kappa\mathrm{g}}(\boldsymbol{\ell}_1,\boldsymbol{\ell}_2,\boldsymbol{\ell}_3) &= \frac{9H_0^4\Omega_m^2}{4c^4}\int \mathrm{d}\chi\,\frac{g^2(\chi)p_f(\chi)}{f_\mathrm{K}^2(\chi)a^2(\chi)}\,\left[b_3r_1B_{\delta\delta\delta}\right](\boldsymbol{k}_1,\boldsymbol{k}_2;\boldsymbol{k}_3;\chi)\\
b_{\mathrm{gg}\kappa}(\boldsymbol{\ell}_1,\boldsymbol{\ell}_2,\boldsymbol{\ell}_3) &= \frac{3H_0^2\Omega_\mathrm{m}}{2c^2}\int \mathrm{d}\chi\,\frac{g(\chi)p_f^2(\chi)}{f_\mathrm{K}^3(\chi)a(\chi)}\,\left[b_3^2r_2B_{\delta\delta\delta}\right](\boldsymbol{k}_1,\boldsymbol{k}_2;\boldsymbol{k}_3;\chi)\\
b_{\mathrm{ggg}}(\boldsymbol{\ell}_1,\boldsymbol{\ell}_2,\boldsymbol{\ell}_3) &= \int \mathrm{d}\chi\,\frac{p_f^3(\chi)}{f_\mathrm{K}^4(\chi)}\,\left[b_3^3B_{\delta\delta\delta}\right](\boldsymbol{k}_1,\boldsymbol{k}_2,\boldsymbol{k}_3;\chi)\,,
\end{aligned}
\tag{3.48}
$$

where $\boldsymbol{k}_\mathrm{i} = \boldsymbol{\ell}_\mathrm{i}/f_\mathrm{K}(\chi)$.

3.3 Ray-tracing simulations

Assumptions such as the Born approximation made to find simplified analytical description of weak gravitational lensing measurements, may not be accurate enough. Alternatively, ray-tracing simulations explicitly trace the propagation of light through the large scale structure of the Universe and provide accurate synthetic lensing observations, see e.g. Jain et al. (2000) and Vale & White (2003).

Ray-tracing simulations employ the multiple lens-plane algorithm and use the inhomogeneous matter distribution generated by dark matter N-body simulations. The three-dimensional matter density is stored in snapshots of the simulation at different redshifts. The basic idea of the multiple-lens-plane algorithm is to project the matter in each snapshot along the line-of-sight onto a lens plane. The light from a distant source is deflected only when passing through a lens plane. The deflection angle can be computed at each position on the lens plane as the gradient of the lensing potential corresponding to the matter distribution in the snapshot. The backward light cone of the observer is then constructed by the stack of all lens planes, with the first lens plane (the closest one to the observer) being the sky that the observer sees. The light rays travel from the observer through the light cone. The path of a light ray in the multiple-lens-plane algorithm is sketched in Fig. 3.5 where $\boldsymbol{\beta}^{(k)}$ is the angular position on the k-th lens plane, and $f_\mathrm{K}^{(k)}$ is the comoving angular diameter distance to the k-th lens plane, and $f_\mathrm{K}^{(k,k')}$ is the distance between plane k and plane k'. As the light rays are deflected intersecting lens planes, using the precalculated deflection angle, the positions of the sources ($\boldsymbol{\beta}$) on each lens plane (knowing that $\boldsymbol{\beta}^{(0)} = \boldsymbol{\beta}^{(1)} = \boldsymbol{\theta}$), can be computed using the equation below (for derivation see Hilbert et al. 2009).

$$
\boldsymbol{\beta}^{(k)} = \frac{1}{f_\mathrm{K}^{(k)}}\left[\left(1+\frac{f_\mathrm{K}^{(k-1,k)}}{f_\mathrm{K}^{(k-2,k-1)}}\right)f_\mathrm{K}^{(k-1)}\boldsymbol{\beta}^{(k-1)} - f_\mathrm{K}^{(k-1,k)}\boldsymbol{\alpha}^{(k-1)}(\boldsymbol{\beta}^{(k-1)}) - \frac{f_\mathrm{K}^{(k-1,k)}}{f_\mathrm{K}^{(k-2,k-1)}}f_\mathrm{K}^{(k-2)}\boldsymbol{\beta}^{(k-2)}\right]. \tag{3.49}
$$

By differentiating this equation with respect to $\boldsymbol{\theta}$ the Jacobian matrix can then be computed.

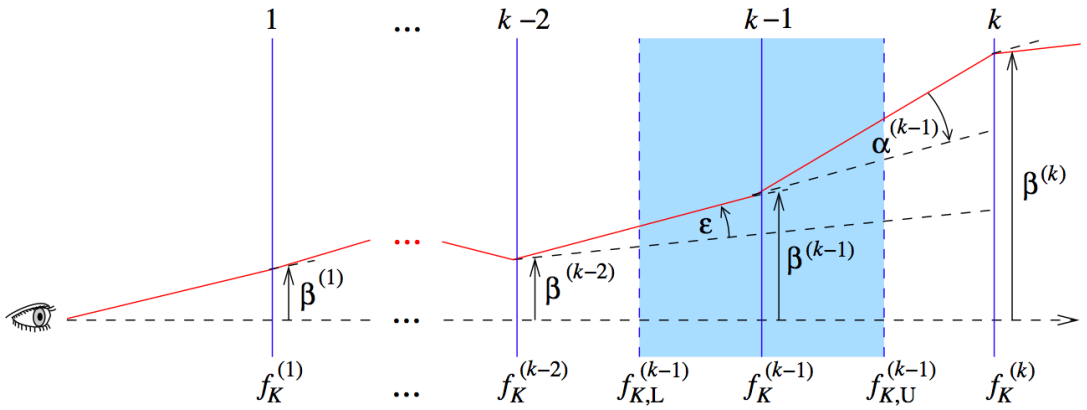

Figure 3.5: Sketch of a light ray path in the multiple-lens-plane approximation. Matter distribution between $f_{\mathrm{K,L}}^{(k-1)}$ and $f_{\mathrm{K,U}}^{(k-1)}$ is projected onto the lens plane $f_{\mathrm{K}}^{(k-1)}$. Source: Hilbert et al. (2009)

CHAPTER 4

Galaxy-galaxy(-galaxy) lensing as a sensitive probe of galaxy evolution

This chapter is based on Saghiha et al. (2012), published in Astronomy & Astrophysics, Volume 547, id.A77, 11 pp.

4.1 Abstract

The gravitational lensing effect provides various ways to study the mass environment of galaxies.

We investigate how galaxy-galaxy(-galaxy) lensing can be used to test models of galaxy formation and evolution.

We consider two semi-analytic galaxy formation models based on the Millennium Run N-body simulation: the Durham model by Bower et al. (2006) and the Garching model by Guo et al. (2011). We generate mock lensing observations for the two models, and then employ Fast Fourier Transform methods to compute second- and third-order aperture statistics in the simulated fields for various galaxy samples.

We find that both models predict qualitatively similar aperture signals, but there are large quantitative differences. The Durham model predicts larger amplitudes in general. In both models, red galaxies exhibit stronger aperture signals than blue galaxies. Using these aperture measurements and assuming a linear deterministic bias model, we measure relative bias ratios of red and blue galaxy samples. We find that a linear deterministic bias is insufficient to describe the relative clustering of model galaxies below ten arcmin angular scales. Dividing galaxies into luminosity bins, the aperture signals decrease with decreasing luminosity for brighter galaxies, but increase again for fainter galaxies. This increase is likely an artifact due to too many faint satellite galaxies in massive group and cluster halos predicted by the models.

Our study shows that galaxy-galaxy(-galaxy) lensing is a sensitive probe of galaxy evolution.

4.2 Introduction

Gravitational lensing effects provide versatile tools for probing the matter distribution in the Universe. Galaxy-galaxy lensing (GGL), for example, is a statistical approach using lensing to obtain information on the mass associated with individual galaxies (see, e.g, Bartelmann & Schneider 2001). This

is achieved by dividing the galaxy population into lenses (foreground) and sources (background). The images of the sources are sheared due to the gravitational field of the foreground lenses and their surrounding mass. The image shearing is usually too small to be detected for individual source-lens galaxy pairs. Instead, the lensing effect is measured as a correlation between the observed image ellipticities and the lens positions. The signal obtained from averaging over many source-lens pairs can then be related to the average mass profiles of the lenses.

Since its first detection (Brainerd et al. 1996), GGL has been measured in many large galaxy surveys (e.g., Hoekstra et al. 2002; Kleinheinrich et al. 2006; Mandelbaum et al. 2006a; Simon et al. 2008; van Uitert et al. 2011, and references therein). Schneider & Watts (2005) advanced GGL to galaxy-galaxy-galaxy lensing (G3L) by introducing third-order correlation functions that involve either configurations with two background sources and one lens galaxy ($G_{\pm}$), or with two lenses and one background source ($\mathcal{G}$). The latter measures the lensing signal around pairs of lens galaxies in excess of what one obtains by simply adding the average signals of two individual galaxies, and thus provides a measure of the excess matter profile about clustered lens galaxy pairs (Simon et al. 2012). This G3L signal has been measured in the Red sequence Cluster Survey (RCS, Gladders & Yee 2005) by Simon et al. (2008), who indeed found an excess mass about lens pairs with projected separation of $250h^{-1}$ kpc. The GG(G)L correlations can be converted to aperture statistics (which we utilize in this work), providing a convenient probe of the galaxy-matter power(bi-)spectra at particular scales.

The galaxy-mass correlation as seen by weak lensing can also be studied theoretically by combining dark matter simulations with semi-analytic models (SAM) of galaxy evolution (White & Frenk 1991; Kauffmann et al. 1999; Springel et al. 2001). In this approach, the dark matter halos of an N-body simulation of cosmic structure formation are populated with galaxies. The propertiesf of the galaxies are calculated by combining information on the halo merger trees of the underlying dark matter simulation with an analytic model of the gas physics in galaxies. The physical processes considered include gas cooling, star formation, metal enrichment, and feedback due to supernovae and active galactic nuclei. Using ray-tracing (e.g. Hilbert et al. 2009), one can then simulate lensing observations of the resulting galaxy distribution.

This work provides a study of the second- and third-order galaxy-mass correlations in semi-analytic galaxy formation models as probed by lensing via aperture statistics (Schneider 1996; Schneider et al. 1998). We consider two models based on the Millennium Run (Springel et al. 2005): the *Durham* model by Bower et al. (2006) and the *Garching* model by Guo et al. (2011). We find that the predicted second- and third-order lensing signals differ between galaxies of different color and magnitude, but also between the different galaxy models. The differences between the models can be traced back to, among other things, different treatments of the satellite galaxy evolution. This illustrates that galaxy-galaxy(-galaxy) lensing can be a sensitive probe of galaxy evolution.

The outline of the chapter is as follows: Section 5.3 provides a brief account of gravitational lensing, aperture statistics, and their relation to correlation functions. Our lensing simulations and the method we use to measure aperture statistics (a fast method based on Fast Fourier Transforms) are described in Sect. 4.4. The results of these measurements for different subsets of galaxies, defined by redshift, luminosity or color, are presented in Sect. 5.5. The main part of the chapter concludes with a summary and discussion in Sect. 5.6. In the Appendix A, we briefly discuss shot-noise corrections for the aperture statistics.

4.3 Theory

4.3.1 Gravitational lensing basics

The matter density inhomogeneities can be quantified by the dimensionless density contrast

$$\delta(\boldsymbol{x},\chi) = \frac{\rho(\boldsymbol{x},\chi) - \bar{\rho}(\chi)}{\bar{\rho}(\chi)}, \tag{4.1}$$

where $\rho(\boldsymbol{x},\chi)$ is the spatial matter density at comoving transverse position $\boldsymbol{x}$ and comoving radial distance χ, and $\bar{\rho}(\chi)$ denotes the mean density at that distance.

To lowest order, the convergence κ for sources at comoving distance χ is related to the matter density contrast δ_m by the projection along the line-of-sight by (e.g. Schneider et al. 2006)

$$\kappa(\boldsymbol{\vartheta},\chi) = \frac{3H_0^2\Omega_\mathrm{m}}{2c^2}\int_0^\chi \mathrm{d}\chi' \, \frac{f_K(\chi-\chi')f_K(\chi')}{f_K(\chi)}\frac{\delta(f_K(\chi')\boldsymbol{\vartheta},\chi')}{a(\chi')}, \tag{4.2}$$

where κ describes the dimensionless projected matter density, H_0 denotes the Hubble constant, Ω_m the mean matter density parameter, c the speed of light, $f_K(\chi)$ the comoving angular diameter distance, and $a(\chi) = 1/(1+z(\chi))$ the scale factor at redshift $z(\chi)$.

For a distribution of sources with probability density $p_\mathrm{s}(\chi)$, the effective convergence is given by Eq. (3.19).

Similar to the definition of the dimensionless matter density contrast δ, one can define the number density contrast δ_g of the lens galaxies as Eq. (3.22). Using the projected number density and the mean projected number density, the projected number density contrast for lens galaxies can be defined as Eq. (3.26).

4.3.2 Aperture Statistics

Aperture statistics was originally introduced as a way to quantify the surface mass density that is unaffected by the mass sheet degeneracy (Schneider 1996). The aperture mass is defined as a convolution,

$$M_\mathrm{ap}(\boldsymbol{\vartheta};\theta) = \int \mathrm{d}^2\boldsymbol{\vartheta}' \, U_\theta(|\boldsymbol{\vartheta}-\boldsymbol{\vartheta}'|)\,\kappa(\boldsymbol{\vartheta}'), \tag{4.3}$$

of the convergence κ and an axi-symmetric filter $U_\theta(|\boldsymbol{\vartheta}|)$ whose size is given by the scale θ, and that is compensated, i.e.

$$\int \mathrm{d}\vartheta \, \vartheta \, U_\theta(\vartheta) = 0. \tag{4.4}$$

In this work, we use the filter introduced by Crittenden et al. (2002),

$$U_\theta(\vartheta) = \frac{1}{2\pi\theta^2}\left[1 - \frac{\vartheta^2}{2\theta^2}\right]\exp\left(\frac{-\vartheta^2}{2\theta^2}\right) = \frac{1}{\theta^2}\,u\left(\frac{\vartheta}{\theta}\right) \quad \text{with} \tag{4.5}$$

$$u(x) = \frac{1}{2\pi}\left[1 - \frac{x^2}{2}\right]\exp\left(\frac{-x^2}{2}\right). \tag{4.6}$$

Its (2-D) Fourier transform has a simple analytical form

$$\tilde{U}_\theta(\ell) = \int \mathrm{d}^2\boldsymbol{\vartheta}\, U_\theta(|\boldsymbol{\vartheta}|)\, \mathrm{e}^{\mathrm{i}\boldsymbol{\ell}\cdot\boldsymbol{\vartheta}} = \frac{\theta^2\ell^2}{2}\, \mathrm{e}^{-\frac{1}{2}\theta^2\ell^2} = \tilde{u}(\theta\ell) \quad \text{with} \tag{4.7}$$

$$\tilde{u}(k) = \frac{k^2}{2}\exp\left(\frac{-k^2}{2}\right). \tag{4.8}$$

The filter falls off exponentially for $\vartheta \gg \theta$. This makes the support of the filter finite in practice.

In analogy to the aperture mass M_ap, one can define the aperture number count

$$\mathcal{N}(\boldsymbol{\vartheta};\theta) = \int \mathrm{d}^2\boldsymbol{\vartheta}'\, U_\theta(|\boldsymbol{\vartheta}-\boldsymbol{\vartheta}'|)\, \kappa_\mathrm{g}(\boldsymbol{\vartheta}'). \tag{4.9}$$

The aperture number count dispersion is related to the angular two-point correlation function w_gg in Eq. (3.45) and its Fourier transform, the angular power spectrum $P_\mathrm{gg}(\ell)$ of the lens galaxies, through

$$\begin{aligned}\langle\mathcal{N}^2\rangle(\theta) &\equiv \langle\mathcal{N}(\boldsymbol{\vartheta};\theta)\mathcal{N}(\boldsymbol{\vartheta};\theta)\rangle \\ &= \int \mathrm{d}^2\boldsymbol{\vartheta}_1\, U_\theta(|\boldsymbol{\vartheta}_1|) \int \mathrm{d}^2\boldsymbol{\vartheta}_2\, U_\theta(|\boldsymbol{\vartheta}_2|)\, w_\mathrm{gg}(|\boldsymbol{\vartheta}_2-\boldsymbol{\vartheta}_1|) \\ &= \int_0^\infty \frac{\ell\mathrm{d}\ell}{2\pi}\tilde{u}^2(\theta\ell)P_\mathrm{gg}(\ell).\end{aligned} \tag{4.10}$$

The function $\tilde{u}(\ell\theta)$ features a sharp peak at $\ell\theta = \sqrt{2}$. Thus, $\langle\mathcal{N}^2\rangle(\theta)$ provides a measurement of the corresponding power spectrum $P_\mathrm{gg}(\ell)$ at wave numbers $\ell \sim 1/\theta$.

Within the halo model framework of cosmic structure (e.g. Cooray & Sheth 2002), $\langle\mathcal{N}^2\rangle(\theta)$ on small scales θ probes the distribution of the lens galaxies within individual dark matter halos. On large scales, $\langle\mathcal{N}^2\rangle$ provides a probe of the clustering of the host halos of the lens galaxies.

Correlating $M_\mathrm{ap}(\theta)$ with $\mathcal{N}(\theta)$ yields

$$\begin{aligned}\left\langle\mathcal{N}M_\mathrm{ap}\right\rangle(\theta) &\equiv \left\langle\mathcal{N}(\boldsymbol{\vartheta};\theta)M_\mathrm{ap}(\boldsymbol{\vartheta};\theta)\right\rangle \\ &= \int \mathrm{d}^2\boldsymbol{\vartheta}_1\, U_\theta(|\boldsymbol{\vartheta}_1|) \int \mathrm{d}^2\boldsymbol{\vartheta}_2\, U_\theta(|\boldsymbol{\vartheta}_2|) w_\mathrm{gm}(|\boldsymbol{\vartheta}_2-\boldsymbol{\vartheta}_1|) \\ &= \int_0^\infty \frac{\ell\mathrm{d}\ell}{2\pi}\tilde{u}^2(\theta\ell)P_\mathrm{gm}(\ell),\end{aligned} \tag{4.11}$$

with $w_\mathrm{gm}(|\boldsymbol{\vartheta}_2-\boldsymbol{\vartheta}_1|) = \langle\kappa_\mathrm{g}(\boldsymbol{\vartheta}_1)\kappa(\boldsymbol{\vartheta}_2)\rangle$, whose Fourier transform is the cross-power spectrum of galaxies and convergence P_gm. The galaxy-galaxy lensing aperture statistics $\langle\mathcal{N}M_\mathrm{ap}\rangle$ probes the average matter profiles around lens galaxies.

A third-order aperture correlator (Schneider & Watts 2005) is obtained by

$$\begin{aligned}\left\langle\mathcal{N}^2M_\mathrm{ap}\right\rangle(\theta) &\equiv \left\langle\mathcal{N}(\boldsymbol{\vartheta};\theta)\mathcal{N}(\boldsymbol{\vartheta};\theta)M_\mathrm{ap}(\boldsymbol{\vartheta};\theta)\right\rangle \\ &= \int \mathrm{d}^2\boldsymbol{\vartheta}_1\, U_\theta(|\boldsymbol{\vartheta}_1|) \int \mathrm{d}^2\boldsymbol{\vartheta}_2\, U_\theta(|\boldsymbol{\vartheta}_2|) \int \mathrm{d}^2\boldsymbol{\vartheta}_3\, U_\theta(|\boldsymbol{\vartheta}_3|) \\ &\qquad \times \left\langle\kappa_\mathrm{g}(\boldsymbol{\vartheta}_1)\kappa_\mathrm{g}(\boldsymbol{\vartheta}_2)\kappa(\boldsymbol{\vartheta}_3)\right\rangle \\ &= \int \frac{\mathrm{d}^2\boldsymbol{\ell}_1}{(2\pi)^2} \int \frac{\mathrm{d}^2\boldsymbol{\ell}_2}{(2\pi)^2}\, \tilde{u}(\theta\,|\boldsymbol{\ell}_1|)\, \tilde{u}(\theta\,|\boldsymbol{\ell}_2|)\, \tilde{u}(\theta\,|\boldsymbol{\ell}_1+\boldsymbol{\ell}_2|) \\ &\qquad \times B_\mathrm{ggm}(\boldsymbol{\ell}_1, \boldsymbol{\ell}_2, -\boldsymbol{\ell}_1-\boldsymbol{\ell}_2)\,,\end{aligned} \tag{4.12}$$

where the last line contains the angular bispectrum of the projected quantities (Schneider & Watts 2005),

$$\langle\tilde{\kappa}_1(\boldsymbol{\ell}_1)\tilde{\kappa}_2(\boldsymbol{\ell}_2)\tilde{\kappa}_3(\boldsymbol{\ell}_3)\rangle = (2\pi)^2\delta_{\rm D}(\boldsymbol{\ell}_1+\boldsymbol{\ell}_2+\boldsymbol{\ell}_3)B_{123}(\boldsymbol{\ell}_1,\boldsymbol{\ell}_2,\boldsymbol{\ell}_3). \tag{4.13}$$

On small scales, $\langle\mathcal{N}^2 M_{\rm ap}\rangle$ can teach us about the average mass distribution of halos hosting two lens galaxies. On larger scales, $\langle\mathcal{N}^2 M_{\rm ap}\rangle$ also provides information on the higher-order clustering of the host halos.

4.3.3 Relative galaxy bias

Clusters and galaxies are biased tracers of the matter distribution (Kaiser 1984; Bardeen et al. 1986; Mo et al. 1996). In the simplest conceivable non-trivial bias model, the bias can be expressed as a linear deterministic relation between the galaxy density contrast and the matter density contrast,

$$\delta_{\rm g}(\boldsymbol{x},\chi) = b_{\rm gm}\delta(\boldsymbol{x},\chi), \tag{4.14}$$

with a bias factor $b_{\rm gm}$ that does not depend on time or scale, but only on the galaxy sample in question.

A more realistic assumption is that the galaxy bias is stochastic and depends on the time and spatial scale. At the two-point level, the bias may then be quantified by a scale-dependent bias factor and correlation factor. A description of the relation between the galaxy and matter densities at the three-point level or higher requires additional, higher-order bias and correlation parameters.

Aperture statistics can be used to constrain the galaxy bias (Schneider 1998; van Waerbeke 1998; Hoekstra et al. 2002; Schneider & Watts 2005; Simon et al. 2007; Jullo et al. 2012). For example, assuming a linear deterministic bias, $\langle\mathcal{N}^2\rangle \propto b^2$, $\langle\mathcal{N}M_{\rm ap}\rangle \propto b$, and $\langle\mathcal{N}^2 M_{\rm ap}\rangle \propto b^2$. For two lens galaxy samples with identical redshift distributions, but different bias parameters b_1 and b_2, one can then determine the relative bias b_1/b_2 from the aperture statistics $\langle\mathcal{N}_{1/2}^2\rangle$, $\langle\mathcal{N}_{1/2}M_{\rm ap}\rangle$, and $\langle\mathcal{N}_{1/2}^2 M_{\rm ap}\rangle$ of the two lens samples by using any of

$$\frac{b_1}{b_2} = \sqrt{\frac{\langle\mathcal{N}_1^2\rangle(\theta)}{\langle\mathcal{N}_2^2\rangle(\theta)}} = \frac{\langle\mathcal{N}_1 M_{\rm ap}\rangle(\theta)}{\langle\mathcal{N}_2 M_{\rm ap}\rangle(\theta)} = \sqrt{\frac{\langle\mathcal{N}_1^2 M_{\rm ap}\rangle(\theta)}{\langle\mathcal{N}_2^2 M_{\rm ap}\rangle(\theta)}}. \tag{4.15}$$

If the measured ratios of the aperture statistics change with scale θ, one can extend the idea to a measurement of a scale-dependent bias. For lens galaxy samples with narrow redshift distributions and deterministic bias, the above ratios still agree (roughly) when compared on the same scales. If the galaxy bias is stochastic or non-linear (Dekel & Lahav 1999), however, the ratios from the different statistics disagree even if measured on the same scale. In that case, the second- and third-order aperture statistics each contain valuable independent information on the second- and third-order bias of the galaxies (Schneider & Watts 2005).

4.4 Methods

4.4.1 Lensing simulations

For our analysis we use the data obtained by ray-tracing through the Millennium Run (Springel et al. 2005). The Millennium Run (MR) is a large N-body simulation of structure formation in a flat ΛCDM universe with matter density $\Omega_{\rm m} = 0.25$, baryon density $\Omega_{\rm b} = 0.045$, dark-energy density $\Omega_\Lambda = 0.75$, a Hubble constant $H_0 = h100\,{\rm km\,s^{-1}Mpc^{-1}}$ with $h = 0.73$, and with a power spectrum normalization

$\sigma_8 = 0.9$. It follows the evolution of $N_\mathrm{p} \sim 10^{10}$ dark matter particles with mass $m_\mathrm{p} = 8.6 \times 10^8 h^{-1}\,\mathrm{M}_\odot$ in a cubic region of comoving side length $500h^{-1}$ Mpc from redshift $z = 127$ to the present.

The simulation volume of the MR is large enough to include massive rare objects, yet with sufficiently high spatial and mass resolution to resolve dark matter halos of galaxies. This allows the construction of merger trees of dark matter halos and subhalos within them. These merger trees have been used in various semi-analytic galaxy formation models to calculate the properties of galaxies in the simulation. Here we consider the *Durham model* by Bower et al. (2006) and the *Garching model* by Guo et al. (2011).[1] Both models have similar treatments of, e.g., gas cooling and star formation, but differ in various details (see the original papers for a full description). The models have been adjusted to be consistent with a large number of observations, in particular the luminosities, stellar masses, morphologies, gas contents and correlations of galaxies at low redshift, but they have not been tuned to match galaxy properties at higher redshift. We make use of the public Millennium Simulations Database[2] (Lemson & Virgo Consortium 2006) to obtain the properties of the galaxies predicted by the two models.

We employ the multiple-lens-plane ray-tracing algorithm described in Hilbert et al. (2009) to calculate the light propagation through the matter in the MR. We generate 64 simulated $4 \times 4\,\mathrm{deg}^2$ fields of view. For each field, we calculate the convergence to sources at a number of redshifts on a regular mesh of 4096^2 pixels, as well as the apparent sky positions, redshifts, and magnitudes of the model galaxies from the Garching and Durham models. The galaxy properties are then used to select various subsamples of the full mock galaxy catalogs as lens populations for the GG(G)L.

4.4.2 Computing aperture statistics

We introduce a fast method to perform aperture statistics measurements on the 64 simulated fields. The statistic used here is built on two main components: (i) the pixelized convergence field $\kappa(\boldsymbol{\vartheta})$ of the source galaxies on square meshes of 4096^2 pixels, and (ii) the pixelized lens galaxy number density fields on meshes with the same geometry. The convergence fields are obtained directly from the ray-tracing algorithm. The galaxy density fields are obtained by projecting the apparent position of the lens galaxies in the fields and counting the number of galaxies in each pixel. Finally, dividing by the mean number density of lens galaxies across all 64 fields results in the galaxy number density contrast $\kappa_\mathrm{g}(\boldsymbol{\vartheta})$.

We calculate the aperture statistics $M_\mathrm{ap}(\vec{\vartheta};\theta)$ and $\mathcal{N}(\vec{\vartheta};\theta)$ from κ and κ_g on a grid by exploiting the convolution theorem, using Fast Fourier Transforms (FFT, in particular the FFTW library by Frigo & Johnson 2005) to carry out the convolution in Eqs. (4.3) and (4.9). To measure M_ap (or $\mathcal{N}$), we calculate the Fourier transforms of κ (or κ_g) and $U_\theta(|\boldsymbol{\vartheta}|)$. We then multiply the results in the Fourier space. Finally an inverse Fourier transformation gives M_ap (or $\mathcal{N}$). The number of grid points in the field is finite (4096×4096 pixels). Therefore, a "Discrete Fourier Transform" is performed by using the Fast Fourier Transform (FFT) algorithm which reduces an $O(N^2)$ process to $O(N\,\log_2 N)$, with N being the number of points being Fourier transformed. Hence, FFT reduces the computation time immensely.

Since $M_\mathrm{ap}(\vec{\vartheta};\theta)$ and $\mathcal{N}(\vec{\vartheta};\theta)$ fields are not periodic, we exclude points closer than 4θ to the field edges from the subsequent analysis. On the remaining points, we then calculate $\mathcal{N}^2(\boldsymbol{\vartheta};\theta)$, $\mathcal{N}(\boldsymbol{\vartheta};\theta)M_\mathrm{ap}(\boldsymbol{\vartheta};\theta)$, and $\mathcal{N}^2(\boldsymbol{\vartheta};\theta)M_\mathrm{ap}(\boldsymbol{\vartheta};\theta)$, and estimate $\langle\mathcal{N}^2\rangle(\theta)$, $\langle\mathcal{N}M_\mathrm{ap}\rangle(\theta)$, and $\langle\mathcal{N}^2M_\mathrm{ap}\rangle(\theta)$ from these products by spatial averaging. We correct the estimates involving $\mathcal{N}^2$ for shot noise as described in Appendix A.

The G3L statistics can also be calculated from the shear field corresponding to κ and the positions of the lens galaxies. In particular, Schneider & Watts (2005) and Simon et al. (2008) showed that $\langle\mathcal{N}^2M_\mathrm{ap}\rangle$

[1] We also considered an earlier incarnation of the Garching model by De Lucia & Blaizot (2007). However, the differences between the results from two Garching models are minor. Thus, we concentrate the discussion on the models by Bower et al. (2006) and Guo et al. (2011).

[2] `http://www.mpa-garching.mpg.de/millennium/`

can be obtained as an integral over a three-point correlation function (3PCF). In order to check our procedure, we use 32 randomly selected simulated fields and calculate $\langle \mathcal{N}^2 M_{\rm ap} \rangle$ also with the latter method, by first calculating this 3PCF with the help of a tree code. We note that, while this tree method is more flexible than the simple FFT-based method described above, in particular with regard to field boundaries and gaps, it is also considerably slower.

For some of the individual fields, we find fairly large discrepancies between the results from the FFT and the tree method – in particular for fields with a large matter overdensity near the field boundaries. We can attribute these discrepancies to the different ways in which the three-point information is weighted in the two approaches. For example, a triplet of points near the boundary of the field enters the statistics in the tree method with the same weight as a similar triplet near the field center. In contrast, the FFT method, by excluding the stripe at the field boundary, assigns zero weight to such a triple. Hence, the results on individual fields can be quite different.

Both methods are consistent, however, when averaging the results over many fields. Randomly selecting 32 simulated fields, we measure $\langle \mathcal{N}^2 M_{\rm ap} \rangle(\theta)$ using the FFT method and the tree method. In the upper panel of Fig. 4.1, the outcomes of the two methods are compared, showing good agreement between the results. The error bars, indicating the statistical error on the signal, tend to be smaller for the tree method than for the FFT method (for apertures larger than 2 arcmin), since the tree method makes better use of the fields' area. For example, for apertures larger than 20 arcmin, more than half of the field is not included in the FFT measurement. Consequently, the difference in scatter becomes more prominent on larger scales. The lower panel in Fig. 4.1 shows the field-by-field difference signal averaged over all fields. The difference between the methods is consistent with zero for $\theta \geq 1$ arcmin, but deviates from zero for $\theta < 1$ arcmin. This is due to a systematic underestimation of the signal in the tree method on small scales (Simon et al. 2008).

4.5 Results

4.5.1 Main lens samples

In this section, we present results for the second- and third-order aperture cross-correlations and aperture number count dispersion for the Durham and the Garching model in the 64 simulated fields created from the Millennium Run. For simplicity, the background population is chosen to be located at $z = 0.99$. Unless stated otherwise, lens galaxies are selected to have redshifts $0.14 \leq z \leq 0.62$, observer-frame r-band apparent magnitude $m_r \leq 22.5$, and stellar masses $M_* \geq 10^9 h^{-1}\,\mathrm{M}_\odot$. This yields 8.5×10^6 lens galaxies in the Durham model and 8.7×10^6 galaxies in the Garching model. The resulting redshift distributions for the lens populations are shown in Fig. 4.2.

For this sample of galaxies, the aperture number count dispersion $\langle \mathcal{N}^2 \rangle$ as a function of aperture radius is shown in the top panel of Fig. 4.3. The galaxy models clearly differ in the predicted dispersion: the Durham model predicts an up to two times larger amplitude than the Garching model. A similar difference has been observed for the angular galaxy correlation function by Kim et al. (2009), who attribute the discrepancy to too many bright satellites in the Durham model. However, as will be discussed below, the Garching model also appears to suffer from problems with the modeling of the satellite population.

The predictions for $\langle \mathcal{N} M_{\rm ap} \rangle$, shown in the middle panel of Fig. 4.3, exhibit fairly large differences between the models, too. The higher values of $\langle \mathcal{N} M_{\rm ap} \rangle$ in the Durham model, especially for smaller angular scales, imply more massive lens halos on average compared to the Garching model. The larger halo masses may also explain the higher clustering amplitude seen in $\langle \mathcal{N}^2 \rangle$. More massive halos host larger concentrations of galaxies and are themselves more clustered, which increases the correlation

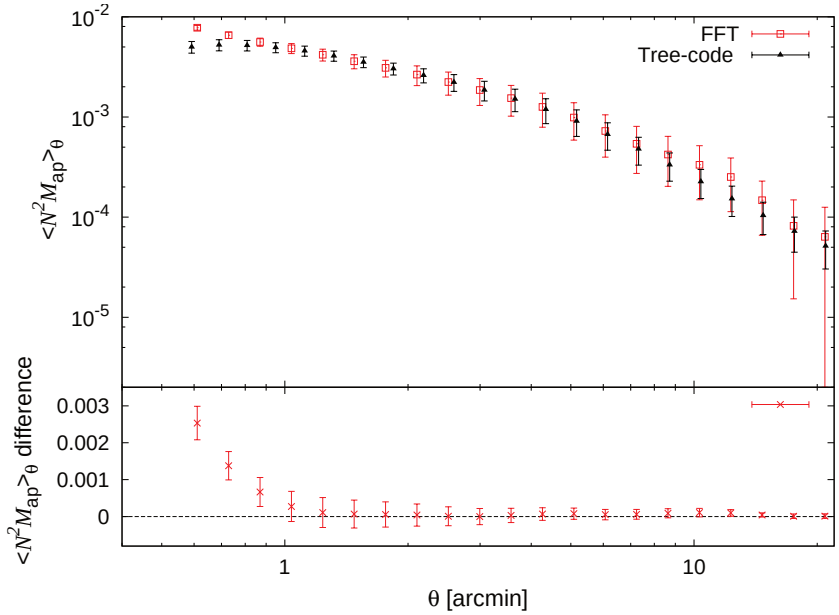

Figure 4.1: Upper panel: Aperture statistics $\langle \mathcal{N}^2 M_{\rm ap} \rangle(\theta)$ as a function of filter scale θ measured in the Garching model. The FFT method (squares) and the tree method (triangles) are compared for lenses at redshift $z = 0.17$ with $m_r \leq 22.5$, stellar masses $M_* \geq 10^9 h^{-1}\,M_\odot$ and convergence field of sources at redshift $z = 0.99$. Error bars indicate the standard deviation of $\langle \mathcal{N}^2 M_{\rm ap} \rangle(\theta)$ for aperture radius θ estimated across 32 fields. Lower panel: Average difference signal between the FFT method and the tree method. Again the error bars show the standard deviation of the mean (field variance of difference signal divided by $\sqrt{31}$).

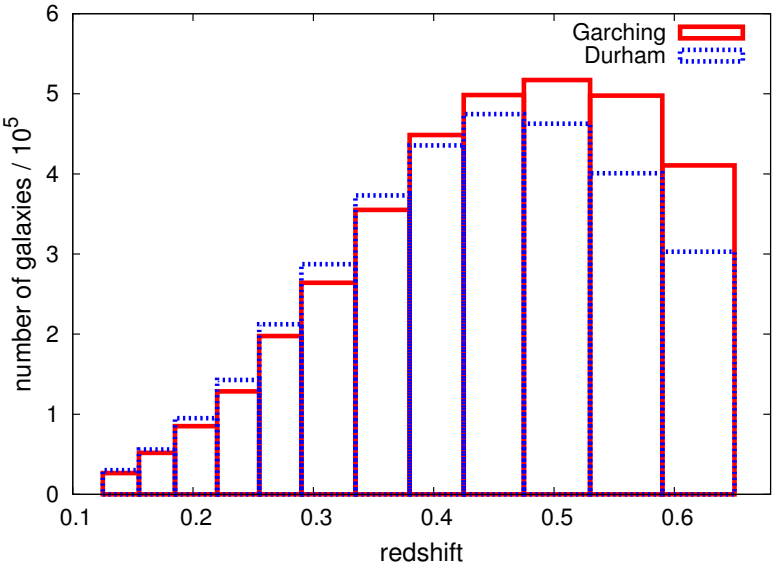

Figure 4.2: Redshift distribution of galaxies in the main lens samples (i.e. galaxies with redshifts $0.14 \leq z \leq 0.62$, observer-frame r-band apparent magnitude $m_r \leq 22.5$, and stellar masses $M_* \geq 10^9 h^{-1} M_\odot$) in the Garching and Durham models.

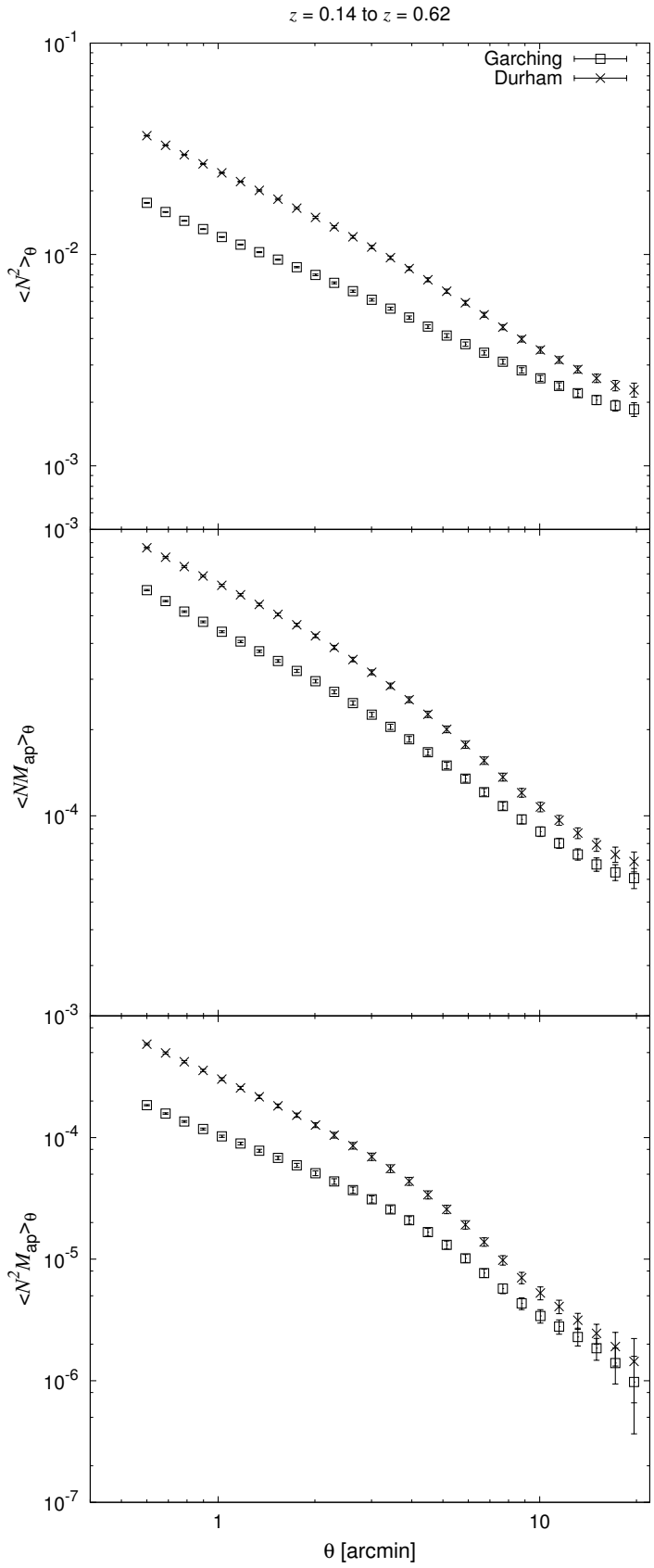

Figure 4.3: Aperture number count dispersion (top panel), $\langle \mathcal{N} M_{\rm ap} \rangle$ (middle panel) and $\langle \mathcal{N}^2 M_{\rm ap} \rangle$ (bottom panel) measurements in the Garching model and Durham model.

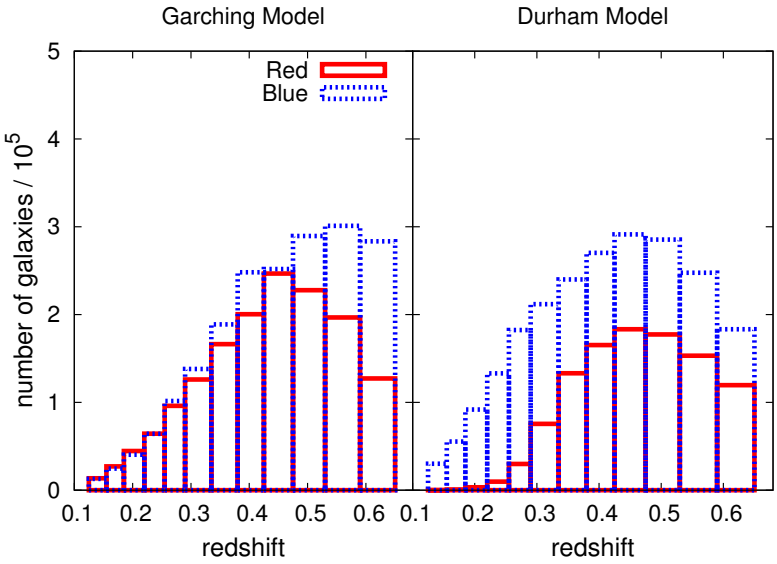

Figure 4.4: Number of red and blue galaxies in the Garching model and the Durham model. Red galaxies are selected to have $u - r > 2.2$ and blue galaxies are to have $u - r \leqslant 2.2$.

of the hosted galaxies on small and large scales. Another consequence is a larger third-order signal $\langle \mathcal{N}^2 M_{\rm ap} \rangle$, which is confirmed by the bottom panel of Fig. 4.3.

4.5.2 Color-selected samples

For a further analysis, we divide the main lens galaxy samples into groups selected by color. From observations, the color distribution of galaxies is well characterized by a bimodal function (Strateva et al. 2001). At low redshifts, this can be approximated by the sum of two Gaussian functions representing red and blue subpopulations of galaxies on the red and blue side of the color distribution, respectively.

Following observations (e.g. Mandelbaum et al. 2006a), we split the main lens galaxy samples at observer-frame color $u - r = 2.2$ to obtain subsamples of red and blue lens galaxies. For the Durham model, we obtain $2.4{\times}10^6$ red and $6.1{\times}10^6$ blue galaxies compared to $4{\times}10^6$ red and $4.7{\times}10^6$ blue galaxies in the Garching model. The redshift distributions of the color subsamples are shown in Fig. 4.4. The histograms show that the relative numbers of red and blue galaxies in each redshift bin differ significantly between the models.

The aperture statistics for these red and blue galaxy populations in both models are shown in the left panels of Fig. 4.5. In both models, red galaxies show higher signals than the blue galaxies. This trend is not surprising, since galaxies of different types follow different distribution patterns and clustering properties. Red galaxies are expected to be found mainly in groups and clusters associated with strong clustering and large halo masses, whereas blue galaxies are mostly field galaxies with smaller halos and lower clustering. The plot also shows that galaxies in the two models show different clustering statistics in both red and blue populations. This may be a result of selecting different objects in the models.

Studying the previous version of the Garching model based on the De Lucia & Blaizot (2007), Bett (2012) pointed out that the distributions of the observer-frame $u - r$ colors are very different in the Garching model and the Durham model. In particular, galaxies appear redder in the Garching model than in the Durham model. We thus consider another way of dividing the galaxies into red and blue samples. We identify the minima of the bimodal distributions at each redshift. The positions of the

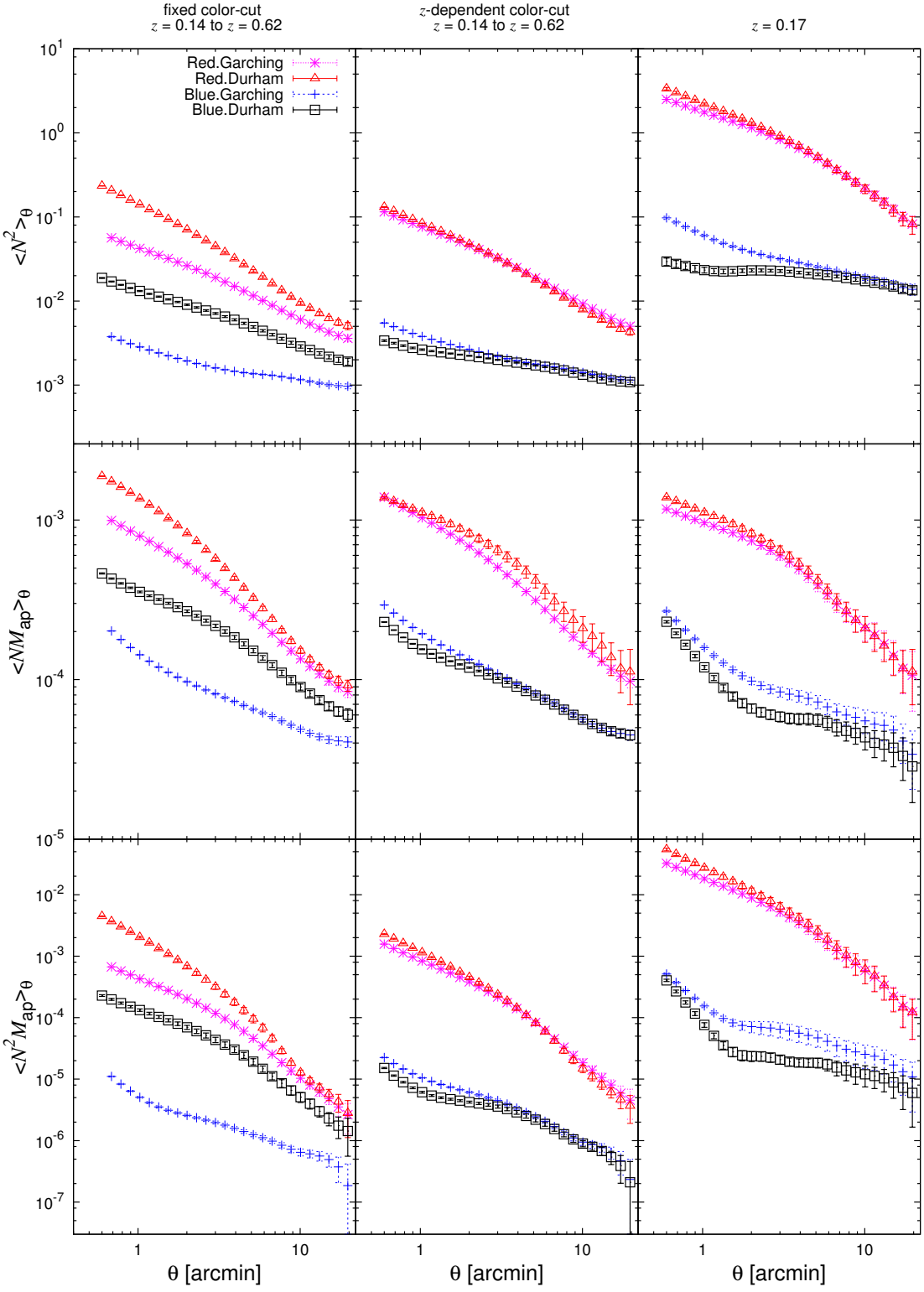

Figure 4.5: Aperture statistics for samples of red and blue galaxies in the Garching and Durham models. The left column shows the results for a fixed color-cut at $u - r = 2.2$ for galaxies with redshift between $z = 0.14$ and $z = 0.62$. The middle column displays the signals for galaxies between $z = 0.14$ and $z = 0.62$ separated using a redshift-dependent color cut. In the right column, galaxies are restricted to come from a single snapshot at redshift $z = 0.17$; accordingly error bars are larger.

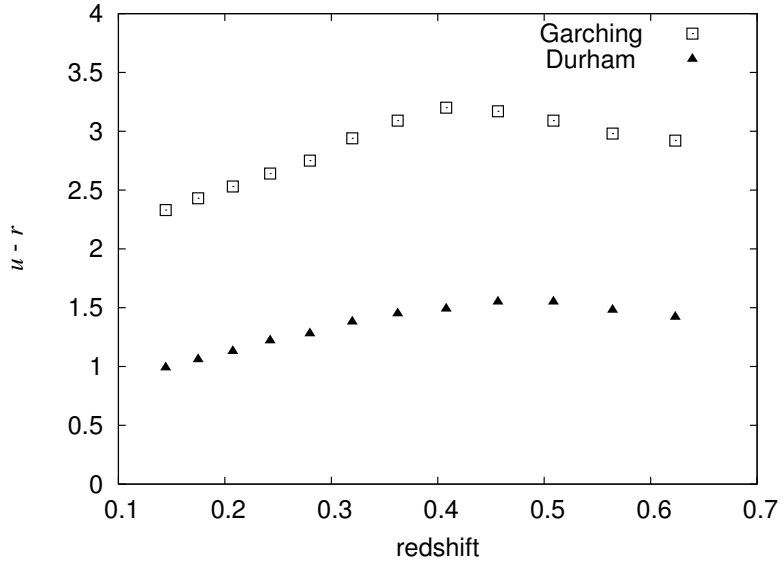

Figure 4.6: The $u - r$ color-cut at each redshift in the Garching and Durham models.

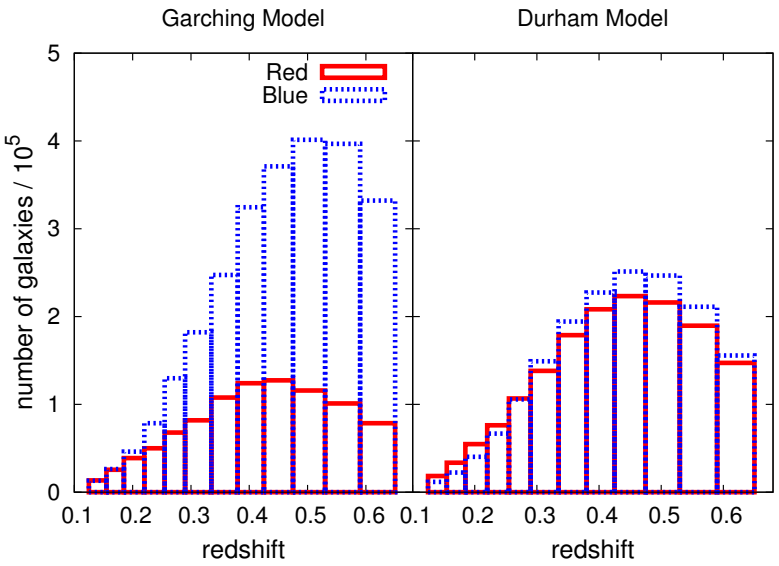

Figure 4.7: Number of red and blue galaxies counted in the Garching model and the Durham model. Galaxies at each redshift are selected according to the color-cut in Fig. 4.6.

minima are plotted in Fig. 4.6, clearly showing a large difference between the models in their color distribution. We then use the minima to separate red and blue galaxies.

Fig. 4.7 shows the resulting redshift distributions of the red and blue subsamples. There are 4.2×10^6 red and 4.3×10^6 blue galaxies in the Durham model compared to 2.5×10^6 red and 6.2×10^6 blue galaxies in the Garching model. Now the difference between the models in the predicted numbers of red and blue galaxies is larger than for the case of a fixed color cut. This suggests that the redshift-dependent color cut selects very different objects in the two models. Surprisingly, the aperture statistics predicted by the two models are much more similar for the redshift-dependent color cuts than for the fixed color cut, as seen in the middle column of Fig. 4.5. The better agreement results from a decrease in the blue signals in the Durham model and an increase in the red signals in the Garching model.

The agreement between the two models shown in the middle column of Fig. 4.5 indicates that although the redshift distributions of red and blue galaxies differ, galaxies populate dark matter halos in such a way to produce similar results. This agreement between the models is more prominently seen in $\langle \mathcal{N}^2 \rangle$ and $\langle \mathcal{N}^2 M_{\rm ap} \rangle$. Looking at $\langle \mathcal{N} M_{\rm ap} \rangle$, red Durham galaxies show a stronger signal on intermediate scales compared to the red Garching galaxies. This can happen, for example, if red galaxies in the Durham model are mostly central galaxies populating large massive halos. On the other hand, this difference may also be a result of the distinct redshift distributions. As will discussed this difference is not seen when galaxies are restricted to come from a single redshift.

Selecting lens galaxies at a single redshift amplifies the signal for $\langle \mathcal{N}^2 \rangle$ and $\langle \mathcal{N}^2 M_{\rm ap} \rangle$ compared to a sample with a broad redshift distribution, where many of the projected galaxy pairs are at different redshifts and are therefore not correlated and suppress the overall signal. The third column of Fig. 4.5 displays the aperture measurements for lens galaxy populations selected from a single redshift slice around $z = 0.17$ with thickness $\Delta z = 0.02$. Now the signals for red galaxies agree well between the two models. The agreement is not so good for blue model galaxies, where the Garching model shows stronger signals on small and intermediate scales. In the halo-model language, blue Garching model galaxies at this redshift appear to live in more massive halos.

Both the Durham and the Garching models predict a larger ratio between the clustering strength of red and blue galaxies than has been obtained in observations. A similar behavior was seen when considering the previous incarnation of the Garching model based on De Lucia & Blaizot (2007). In particular, our results confirm the previous work of de la Torre et al. (2011), who compared the color-dependent projected two-point correlation function of a color subsample of galaxies in the VIMOS-VLT Deep Survey (VVDS; Le Fèvre et al. 2005) and in the model based on De Lucia & Blaizot (2007). They showed that red galaxies in the semi-analytic models have stronger clustering amplitudes than the observed ones. They linked this discrepancy to an overproduction of bright red galaxies in the model.

The different clustering strengths of red and blue galaxies show up very clearly in $\langle \mathcal{N}^2 \rangle$, $\langle \mathcal{N} M_{\rm ap} \rangle$, and $\langle \mathcal{N}^2 M_{\rm ap} \rangle$. The ratio of the clustering amplitude of the red and blue samples is related to their relative bias (Sect. 4.3.3). This ratio can be measured based on different aperture statistics measurements presented in Fig. 4.5. Assuming a simple linear deterministic bias, the relative bias and its uncertainty is calculated on aperture scales of $\theta \sim 1$ arcmin and $\theta \sim 10$ arcmin in the Garching and Durham models. The results are shown in Table 4.1.

The differences in the bias ratios measured from different statistics point out that a linear deterministic bias model is not sufficient to describe the relation between the galaxy and matter distribution on different scales. This relation may be described by scale-dependent stochastic bias.

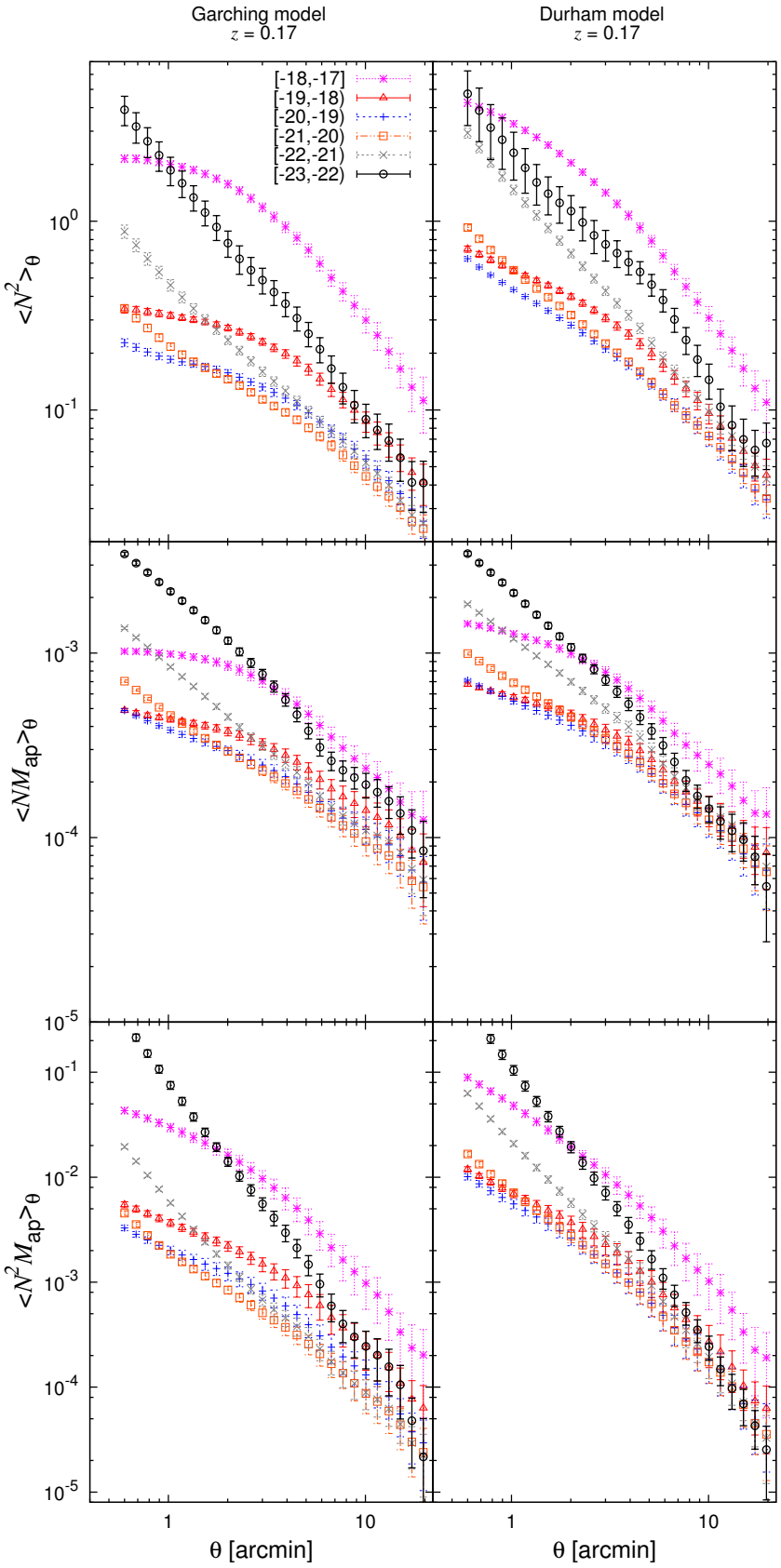

Figure 4.8: Aperture measurements in the Garching model (left panel) and the Durham model (right panel) in 6 different r-band absolute magnitude, M_r, bins.

Table 4.1: The relative bias $b_{\rm red}/b_{\rm blue}$ based on different aperture statistics (Sect. 4.3.3) measured according to the right column of Fig. 4.5 on scales of 1 and 10 arcmin in the Garching and Durham models. The values are obtained assuming a linear deterministic bias model.

		$\langle \mathcal{N}^2 \rangle$	$\langle \mathcal{N} M_{\rm ap} \rangle$	$\langle \mathcal{N}^2 M_{\rm ap} \rangle$
$1'$	Garching	5.4±0.1	6.06±0.21	10.83±0.32
	Durham	9.73±0.13	9.34±0.37	18.9±0.64
$10'$	Garching	3.37±0.19	3.84±0.93	4.8±0.94
	Durham	3.52±0.21	4.82±1.1	7.15±1.5

4.5.3 Magnitude-selected samples

In this section, we present the measurements of the second- and third-order aperture statistics for lens galaxies in six different bins of r-band absolute observer frame magnitude M_r. To eliminate effects of possibly different redshift distributions on the signals, we restrict the redshift range of the lens galaxy population to one redshift slice at $z = 0.17$. The results for all magnitude bins for the Garching (Durham) model are shown in the left (right) panels of Fig. 4.8.

There are common trends seen for both models in the second- and third-order aperture statistics. For the brighter bins ($-23 \leq M_r < -20$), the aperture signals decrease rapidly with increasing magnitude M_r and filter scales θ. However, the Durham model predicts up to 200% higher $\langle \mathcal{N}^2 M_{\rm ap} \rangle$, and $\langle \mathcal{N}^2 \rangle$ signals than the Garching model. Bright galaxies appear more clustered and on average to be located in more massive halos in the Durham model.

For the fainter bins ($-20 \leq M_r < -18$), the signals *increase* with decreasing luminosity. This increase is contrary to observations of galaxy clustering and GGL (see e.g. McBride et al. 2011), where brighter galaxies show stronger clustering and larger lensing signals than fainter galaxies.

In the Garching model, the faint magnitude bins are over-populated with satellite galaxies, many of which have no own subhalo (this occurs when a galaxy has been stripped of its own halo during a merger process with a larger halo). These galaxies are abundant in massive halos, which contribute substantially to the $\langle \mathcal{N} M_{\rm ap} \rangle$ and $\langle \mathcal{N}^2 M_{\rm ap} \rangle$ signal due to their large mass and stronger clustering. In the Durham model a similar trend is seen in $\langle \mathcal{N} M_{\rm ap} \rangle$ and $\langle \mathcal{N}^2 M_{\rm ap} \rangle$, indicating similar problems with the modeling of the satellite population in massive halos.

The luminosity dependence of galaxy clustering has been studied extensively with the aid of galaxy surveys. Li et al. (2007) compared the luminosity dependence of the clustering of galaxies in the model of Croton et al. (2006) to results from the Sloan Digital Sky Survey Data Release Four (SDSS DR4; Adelman-McCarthy et al. 2006), and found that the faint model galaxies show a stronger clustering than SDSS galaxies.

Kim et al. (2009) compared the galaxy clustering predicted by the models of Bower et al. (2006), De Lucia & Blaizot (2007) and Font et al. (2008) to observed clustering in the two-degree Field Galaxy Redshift Survey (2dF, Colless et al. 2001). They found that none of the models are able to match the observed clustering properties of galaxies in different luminosity bins. In particular, the Durham model shows a stronger signal than expected, which could possibly be corrected, if the number of satellite galaxies in halos is reduced.

Both Li et al. (2007) and Kim et al. (2009) emphasize the problems of the galaxy models in predicting the luminosity dependence of galaxy clustering. Li et al. (2007) showed that the number of faint satellite galaxies has to be reduced by 30 per cent (regardless of their host halo mass) to better match the observed galaxy clustering. Kim et al. (2009) showed that the fraction of satellites declines with increasing luminosity (see, e.g. Fig 4 in Kim et al. 2009) in the host halo mass range of $10^{12} h^{-1}\,{\rm M}_\odot \lesssim M_{\rm halo} \lesssim$

$10^{14}h^{-1}\,\mathrm{M}_{\odot}$. Since the clustering strength depends strongly on the halo mass, satellite galaxies can affect the overall clustering amplitude. To investigate this they used a simple HOD model to show that satellite galaxies show a strong bias due to a strong two-halo clustering term. This indicates that satellite galaxies are preferentially found in massive halos which exhibits larger bias (see Fig. 5 in Kim et al. 2009). They argued that the results can be improved if the satellites are removed from massive halos by adding satellite-satellite merger processes in the models.

Our results suggest that the Garching model shows a similar problem with faint satellite galaxies, though to a lesser degree. Indeed, we find that the amplitude of the aperture signals in the faint bins are completely dominated by satellite galaxies in both the Durham and the Garching model. Most of these faint satellites reside in massive group and cluster halos, which results in very large aperture signals on the scales considered in this work.

4.6 Summary and discussion

Through observations of galaxy-galaxy(-galaxy) lensing, valuable information on the clustering properties of the galaxy and matter density field in the Universe can be obtained. Measurements of galaxy-galaxy lensing (GGL) can be used to infer information on the properties of dark matter halos hosting the lens galaxies (see, e.g., Schneider & Rix 1997; Johnston et al. 2007; Mandelbaum et al. 2008). Third-order galaxy lensing (G3L) can be used to infer information on the properties of a common dark matter halo hosting two lens galaxies (Simon et al. 2008; 2012).

In this work, we study how the information from GGL and G3L aperture statistics can be used to test models of galaxy formation and evolution. We investigate two semi-analytic galaxy formation models based on the Millennium Run N-body simulation of structure formation (Springel et al. 2005): the Durham model by Bower et al. (2006), and the Garching model by Guo et al. (2011). Using mock galaxy catalogs based on these models in conjunction with ray-tracing (Hilbert et al. 2009), we create simulated fields of galaxy lensing surveys. From these simulated surveys, we compute the model predictions for the second- and third-order aperture statistics $\langle \mathcal{N}^2 \rangle$, $\langle \mathcal{N} M_{\mathrm{ap}} \rangle$, and $\langle \mathcal{N}^2 M_{\mathrm{ap}} \rangle$ for various galaxy populations.

We find that both semi-analytic models predict aperture signals that are qualitatively similar, but there are large quantitative differences. The Durham model predicts larger amplitudes for most considered galaxy samples. This indicates that lens galaxies in the Durham model tend to reside in more massive halos than lens galaxies in the Garching model.

In both the Durham and the Garching model, red galaxies exhibit stronger aperture signals than blue galaxies, in qualitative agreement with observations. However, both models predict a larger ratio between the clustering strength of red and blue galaxies than has been obtained in observations. These findings corroborate the findings of de la Torre et al. (2011), who showed that red galaxies in the semi-analytic models have stronger clustering amplitudes than red galaxies in observations.

We argue that considering the amplitude ratio between the red and blue galaxies and making comparison between the second- and third-order aperture statistics leads to the conclusion that the third-order bias differs from the second-order bias. In other words, third-order aperture statistics provides new information which cannot be obtained from the second-order statistics alone. The large amplitude ratio between the clustering of red and blue galaxies in the models means a large relative bias of these galaxy populations. Measuring the biasing of galaxies provides information on the relative distribution of galaxies and the underlying matter distribution. We find that a linear deterministic bias model, even with scale-dependent bias parameters, is clearly ruled out by considering second and third-order aperture statistics for the simulated data. We expect that both statistics in combination will provide new

information to constrain more advanced galaxy biasing models in the future.

In addition to the different prediction for red and blue galaxies, there are discrepancies between the predictions of the two models. For a fixed color cut at $u - r = 2.2$, the signals predicted by the Durham model are larger than those predicted by the Garching model. If a redshift-dependent color cut is used instead, the prediction from the two models for the aperture signals become more similar. However, the models then strongly disagree about the total numbers and redshift distributions of blue and red galaxies.

Both galaxy models predict that the aperture statistics decrease with decreasing luminosity for brighter galaxies in accordance with observations. However, the models also predict that the signals increase again for fainter galaxies. This behavior is most likely an artifact related to too many faint satellite galaxies in massive group and cluster halos predicted by the models. In fact, the fainter magnitude bins are completely dominated by satellite galaxies in both models. The problem appears more severe in the Durham model than in the Garching model, which differ in their treatment of satellite evolution.

We plan to extent our treatment in future work to study how well galaxy bias models with scale-dependent stochastic bias can be constrained with second- and third-order galaxy lensing statistics. One important question is how much information can be obtained from G3L in addition to that obtained from GGL.

Furthermore, we are looking forward to measurements of GGL and G3L signals in large ongoing and future surveys. The comparison of the observed signals and the signals predicted by galaxy models will help to identify shortcomings of the models and provide valuable hints for improvements in the models. This will also require a deeper understanding of the relation between the various details of the galaxy formation models and the predicted galaxy lensing and clustering signals.

CHAPTER 5

Confronting semi-analytic galaxy models with galaxy-matter correlations observed by CFHTLenS

This chapter is based on Saghiha et al. (2016), submitted to Astronomy & Astrophysics.

5.1 Abstract

Testing predictions of semi-analytic models of galaxy evolution against observations help to understand the complex processes that shape galaxies. We compare predictions from the Garching and Durham models implemented on the Millennium Run with observations of galaxy-galaxy lensing (GGL) and galaxy-galaxy-galaxy lensing (G3L) for various galaxy samples with stellar masses in the range $0.5 \leq M_*/10^{10}\,\mathrm{M}_\odot < 32$ and photometric redshift range $0.2 \leq z < 0.6$ in the Canada-France-Hawaii Telescope Lensing Survey (CFHTLenS). We find that the predicted GGL and G3L signals are in qualitative agreement with CFHTLenS data. Quantitatively, the models succeed in reproducing the observed signals in the highest stellar mass bin ($16 \leq M_*/10^{10}\,\mathrm{M}_\odot < 32$) but show different degrees of tension for the other stellar mass samples. The Durham model is strongly excluded on a 95% confidence level by the observations as it largely over-predicts the amplitudes of GGL and G3L signals, probably owing to a larger number of satellite galaxies in massive halos.

5.2 Introduction

In the framework of the ΛCDM cosmology, galaxies and stars form from the gravitational collapse of baryonic matter inside dark matter halos. Semi-analytic models (SAMs) of galaxies are used to describe the connection between the resulting galaxy properties and the underlying distribution of dark matter (White & Frenk 1991; Kauffmann et al. 1999; Springel et al. 2001; Baugh 2006). Herein SAMs apply analytic prescriptions to approximate the complex processes of gas cooling, star formation, and feedback due to supernovae and active galactic nuclei. These prescriptions are calibrated to observations of galaxy properties such as the galaxy luminosity function or the Tully-Fischer relation using efficiency parameters and halo merger trees extracted from N-body simulations of structure formation (e.g., Springel et al. 2005; Angulo et al. 2012).

Gravitational lensing allows us to study the distribution of galaxies in relation to the matter density (e.g. Bartelmann & Schneider 2001; Schneider et al. 2006). In the weak lensing regime, the tangential distortion of the image of a distant source galaxy or its "shear" may be measured as function of separation to foreground lenses to probe their correlation to the matter density field. This tangential shear is averaged over many lens-source pairs to obtain a detectable lensing signal. This galaxy-galaxy lensing (hereafter GGL) signal has been first detected by Brainerd et al. (1996). The field of GGL has been growing rapidly since then thanks to larger surveys and more accurate shear measurements (see e.g. Mandelbaum et al. 2006b; van Uitert et al. 2011; Leauthaud et al. 2012; Velander et al. 2014; Viola et al. 2015; van Uitert et al. 2016; Clampitt et al. 2016). In essence, GGL measures the average projected matter density around lens galaxies. It thereby probes the statistical properties of dark matter halos in which galaxies reside. On small scales, GGL is dominated by the contribution from the host halo, but on larger scales, the neighboring halos also contribute to the signal.

Schneider & Watts (2005) considered third-order correlations between lens galaxies and shear, called galaxy-galaxy-galaxy lensing (G3L). They defined two classes of three-point correlations: galaxy-shear-shear correlation function measured using triples composed of two sources and one lens galaxy, and the galaxy-galaxy-shear correlation function measured using triples comprising two lenses and one source galaxy. For this study, we consider only the lens-lens-shear correlations ($\mathcal{G}$), which measures the average tangential shear about lens pairs. The first detection of G3L was reported by Simon et al. (2008) using the Red sequence Cluster Survey (RCS, Gladders & Yee 2005) data. The lens-lens-shear G3L essentially probes the stacked matter density around lens pairs in excess to the stack of two single lenses (Simon et al. 2012). Recently, the G3L signal was analyzed in the CFHTLenS by Simon et al. (2013), where it was found that the amplitude of G3L increases with stellar mass and luminosity of the lens galaxies.

Measurements of GGL and G3L provide valuable data to test the ability of SAMs to correctly describe the connection between dark matter and galaxies as a function of scale and galaxy properties. The predictions for the expected lensing signals from SAMs needed for this comparison can be obtained by combining the simulated galaxy catalogs from the SAMs with outputs from gravitational lensing simulations using ray-tracing through the matter distribution of the underlying N-body simulation (e.g. Hilbert et al. 2009). In Saghiha et al. (2012), the G3L signal was computed for various galaxy models based on the Millennium Simulation (Springel et al. 2005). There, the second- and third-order galaxy-matter correlation functions were represented in terms of aperture measures in the simulation, thereby allowing a straightforward comparison of different SAMs. According to this study, G3L is a sensitive probe of galaxy properties such as color, luminosity, and of different implementations of SAMs.

In this chapter, we compare SAM predictions of GGL and G3L to CFHTLenS data. We consider three SAMs based on the Millennium Run: Bower et al. (2006, hereafter B06), Guo et al. (2011, hereafter G11), and Henriques et al. (2015, hereafter H15).

The chapter is organized as follows: Section 5.3 summarizes the formulation of GGL and G3L in terms of tangential shear and aperture statistics. In Sect. 5.4, we describe the complete data set and the method that we apply to select model galaxies from the SAMs. In Sect. 5.5, we compare the model predictions with lensing observations for various sub-samples of galaxies, based on redshift and stellar mass. We discuss our results in Sect. 5.6.

5.3 Theory

GGL probes the correlation of the inhomogeneities in the matter density and galaxy number density fields, namely the cross-correlation of the tangential shear in the source image and the position of the lens galaxy, (Eq. 3.33). For a choice of compensated filter function such as $U_\theta(|\boldsymbol{\vartheta}|)$ defined in Eq. (4.5),

the aperture mass (Eq. 4.3) can be written as

$$M_{\rm ap}(\boldsymbol{\vartheta};\theta) = \int \mathrm{d}^2\vartheta'\, Q_\theta(|\boldsymbol{\vartheta}-\boldsymbol{\vartheta}'|)\,\gamma_{\rm t}(\boldsymbol{\vartheta}'), \tag{5.1}$$

with

$$Q_\theta(\vartheta) = \frac{2}{\vartheta^2}\int_0^\vartheta \mathrm{d}\vartheta'\vartheta' U_\theta(\vartheta') \;-\; U_\theta(\vartheta). \tag{5.2}$$

We make predictions of G3L with $\left\langle \mathcal{N}^2 M_{\rm ap}\right\rangle(\theta)$ which is the third-order correlation of aperture mass and aperture number counts $\mathcal{N}$ at zero lag (Eq. 4.12). For simplicity we used the same aperture sizes for $\mathcal{N}$ and $M_{\rm ap}$. For homogeneous random fields such as κ and $\kappa_{\rm g}$, the ensemble average $\left\langle \mathcal{N}^2 M_{\rm ap}\right\rangle$ is independent of the position of the centre of the aperture and can be calculated by (spatial) averaging the product $\mathcal{N}^2(\boldsymbol{\vartheta};\theta)M_{\rm ap}(\boldsymbol{\vartheta};\theta)$. In our analysis, as in Chapter 4, we thus calculate the product $\mathcal{N}^2 M_{\rm ap}$ over the simulated area. Third-order aperture statistics can also be calculated from the measurements of three-point galaxy-shear correlation functions (Schneider & Watts 2005). In particular their Eq. (63) shows that $\left\langle \mathcal{N}^2 M_{\rm ap}\right\rangle$ is related to the galaxy-galaxy-shear correlation function via an integral transformation. This has been done to obtain the CFHTLenS measurements.

5.4 Data

5.4.1 CFHTLenS galaxies

CFHTLens is a multi-color lensing survey (Heymans et al. 2012; Erben et al. 2013; Miller et al. 2013), incorporating $u^*g'r'i'z'$ multi-band data from the CFHT Legacy Survey Wide Programme. It covers 154 deg^2 of the sky. Accurate photometry provided photometric redshifts of 7×10^6 galaxies (Hildebrandt et al. 2012). The stellar masses of galaxies are estimated by fitting a model of the spectral energy distribution (SED) to the galaxy photometry. In this method, a set of synthetic SEDs are generated using a stellar population synthesis (SPS) model, and the maximum likelihood SED template that fits the observed photometry of a galaxy is obtained. Thus the SED fitting method relies on assumptions of the SPS models, star formation histories, initial mass function (IMF), and dust extinction models. The stellar masses of CFHTLenS galaxies are estimated using the SPS model of Bruzual & Charlot (2003) and assuming an IMF by Chabrier (2003). By taking into account the error on the photometric redshift estimates as well as the uncertainties in the SED fitting, Velander et al. (2014) estimated that the statistical uncertainties on the stellar mass estimates of CFHTLenS galaxies are about 0.3 dex.

In Simon et al. (2013), the G3L analysis of CFHTLenS data is presented in terms of aperture statistics for a sample of source galaxies with $i' < 24.7$ and mean redshift of $z = 0.93$, and lens galaxies brighter than $i' < 22.5$. The foreground sample is further subdivided in six stellar mass bins as given in Table 5.1. These stellar mass bins are then further split into two photometric redshift samples, $0.2 \le z_{\rm ph} < 0.44$ ("low-z") and $0.44 \le z_{\rm ph} < 0.6$ ("high-z"). The redshift distribution of galaxies in these samples can be found in Fig. 5 of Simon et al. (2013). We utilize these for the predictions of the lensing statistics.

5.4.2 Mock galaxies

We use simulated lensing data obtained by a ray-tracing algorithm applied to the Millennium Simulation which is an N-body simulation that traces the evolution of 2160^3 particles in a cubic region of comoving side length $500h^{-1}$Mpc from redshift $z = 127$ to the present time (MS, Springel et al. 2005). The MS

Table 5.1: Binning in stellar mass of CFHTLenS galaxies for the low-z and high-z samples.

stellar mass bin	selection
sm1	$0.5 \leq M_*/10^{10}\mathrm{M}_\odot < 1$
sm2	$1 \leq M_*/10^{10}\mathrm{M}_\odot < 2$
sm3	$2 \leq M_*/10^{10}\mathrm{M}_\odot < 4$
sm4	$4 \leq M_*/10^{10}\mathrm{M}_\odot < 8$
sm5	$8 \leq M_*/10^{10}\mathrm{M}_\odot < 16$
sm6	$16 \leq M_*/10^{10}\mathrm{M}_\odot < 32$

Table 5.2: Cosmological parameters for the assumed cosmology in the MS compared to the Planck cosmology.

Parameters	MS	Planck
Ω_Λ	0.75	0.685
Ω_b	0.045	0.0487
Ω_m	0.25	0.315
f_b	0.17	0.155
σ_8	0.9	0.829
n_s	1.0	0.96
$H_0[\mathrm{km\,s^{-1}Mpc^{-1}}]$	73	67.3

assumes a ΛCDM cosmology with parameters based on 2dFGRS (Colless et al. 2001) and first-year WMAP data (Spergel et al. 2003). These parameters are summarized in Table 5.2.

We use galaxy catalogs from B06, G11, and H15 implemented on the MS.[1] All these three models use similar treatments for basic physical baryonic processes such as gas cooling, star formation and feedback from supernovae and AGNs, but they differ in various details. We refer to some of these differences later in the chapter.

The gravitational lensing in the Millennium simulation is computed by the multiple-lens-plane ray-tracing algorithm of Hilbert et al. (2009) in 64 fields of view of $4 \times 4\,\mathrm{deg}^2$ each. The resulting synthetic data include the convergence and shear (on regular meshes of 4096^2 pixels) of sources at a set of redshifts given by the output times of the simulation snapshots. These are then combined into convergence and shear fields for the CFHTLenS redshift distribution. Furthermore, the data contains the image positions, redshifts, stellar masses, and various other galaxy properties of the galaxies computed by the SAMs.

We generate mock galaxy samples similar to the lens samples observed in CFHTLenS following three steps.

(i) We convert the SAM magnitudes to the Megacam AB magnitudes in CFHTLenS. We convert the SDSS AB magnitudes of G11 and H15 to Megacam AB magnitude i'_AB by applying the conversion relation from Erben et al. (2013):

$$i'_\mathrm{AB} = i_\mathrm{AB} - 0.085(r_\mathrm{AB} - i_\mathrm{AB})\,. \tag{5.3}$$

[1] One prominent improvement in H15 is that the simulations are rescaled to the Planck cosmology according to the method described in Angulo & White (2010) and Angulo & Hilbert (2015). However, here we use the H15 model adjusted to the original MS cosmology.

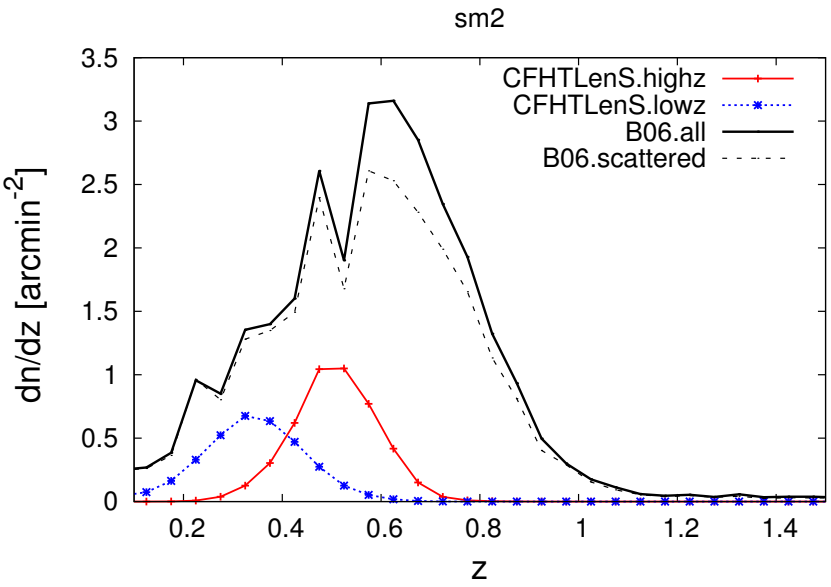

Figure 5.1: Number density distribution per unit solid angle and redshift interval of flux-limited galaxies in sm2 (the total area below each curve is the total number density of galaxies). The blue and red curves show the distribution of CFHTLenS galaxies in the low-z and high-z samples, respectively. The solid black curve represents all galaxies of the B06 model above the flux limit and with stellar mass in the sm2 bin. The dashed black curve shows the distribution when also applying a random error to the stellar masses of the B06 galaxies.

We convert the SDSS Vega magnitudes of B06 to CFHTLenS AB magnitudes using:[2]

$$i'_{\rm AB} = (i_{\rm Vega} + 0.401) - 0.085\left(\left[r_{\rm Vega} + 0.171\right] - \left[i_{\rm Vega} + 0.401\right]\right) . \tag{5.4}$$

We then select lens galaxies brighter than $i'_{\rm AB} < 22.5$. The redshift distribution of all flux-limited galaxies from the B06 model that fall into the stellar-mass bin sm2 is shown in Fig. 5.1.

(ii) In order to emulate the CFHTLenS error of stellar masses, we randomly add Gaussian noise with RMS 0.3 dex to the stellar mass $\log M_*$ in the mocks. The resulting redshift distribution of galaxies in B06 is also shown in Fig. 5.1.

(iii) As can be seen in Fig. 5.1, the redshift distribution of model galaxies differs from that of CFHTLenS (the dashed black curve compared to the red or blue curves in Fig. 5.1). To select a realistic simulated sample, the mock samples must have the same redshift distributions as the corresponding CFHTLenS samples to produce the same lensing efficiency. Therefore, in the last step, we use a rejection method to reproduce the redshift distribution of galaxies in CFHTLenS. In this step, we randomly discard a galaxy at redshift z from the mock sample if

$$x > \frac{{\rm d}n_{\rm SAM}/{\rm d}z}{{\rm d}n_{\rm CFHTLenS}/{\rm d}z} \tag{5.5}$$

is satisfied for a random number in the range 0 to 1. The distribution of selected galaxies in the low-z and high-z samples are not shown in Fig. 5.1 since they are practically identical to the corresponding CFHTLenS distributions.

[2] `http://www.cfht.hawaii.edu/Instruments/Imaging/MegaPrime/specsinformation.html`

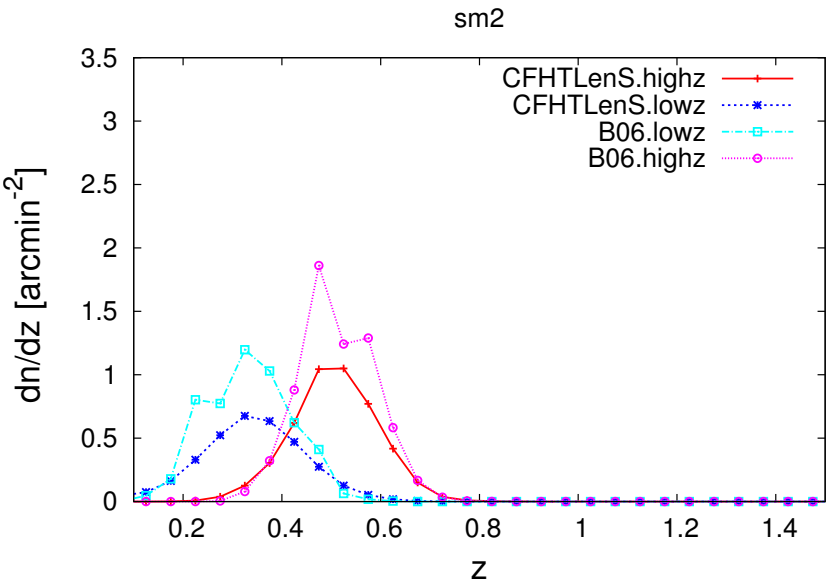

Figure 5.2: Similar to Fig. 5.1, the blue and red curves show the distribution of CFHTLenS galaxies in the low-z and high-z samples, respectively. The curves labeled as "B06.lowz" (cyan) and "B06.highz" (magenta) correspond to a sample of galaxies selected from the distribution shown by the dashed black curve in Fig. 5.1 after adding the error of photometric redshifts in CFHTLenS to the mock redshifts.

One should note that in the method described above, we have not included the error in the photo-z estimation. However, including such an uncertainty has no effect on the statistical properties of the SAM galaxy distributions. Indeed, Fig. 5.2 shows the true redshift distribution of B06 galaxies for low-z and high-z samples after including an emulated photo-z error, and after applying the same photo-z cuts as in CFHTLens. For this, we choose galaxies from the "B06.scattered" distribution (dashed black curve in Fig. 5.1) and add a random Gaussian photo-z error with RMS $0.04(1 + z)$ (Hildebrandt et al. 2012). The PDF of the true redshifts of low-z and high-z samples are labelled "B06.lowz" and "B06.highz" in Fig. 5.2. Despite having slightly different amplitudes, these distributions have similar shapes as the "CFHTLenS.lowz" (blue) and "CFHTLenS.highz" (red) distributions, respectively. After applying the rejection method (step iii) on those distributions, one obtains mock galaxy samples with the same statistical properties of the mock galaxy samples that we produce following the three steps described previously.

5.5 Results

5.5.1 GGL

Fig. 5.3 shows the azimuthally averaged tangential shear $\langle\gamma_t\rangle(\theta)$ for an angular range of 0.5 to 35 arcmin as measured in CFHTLenS in comparison to the SAM predictions. The samples are split in stellar mass and redshift. For both CFHTLenS data and model galaxies, the amplitude of the GGL signal increases with stellar mass. For a given stellar mass bin, the amplitudes of the observed and simulated signals decrease when increasing the lens-source separation θ.

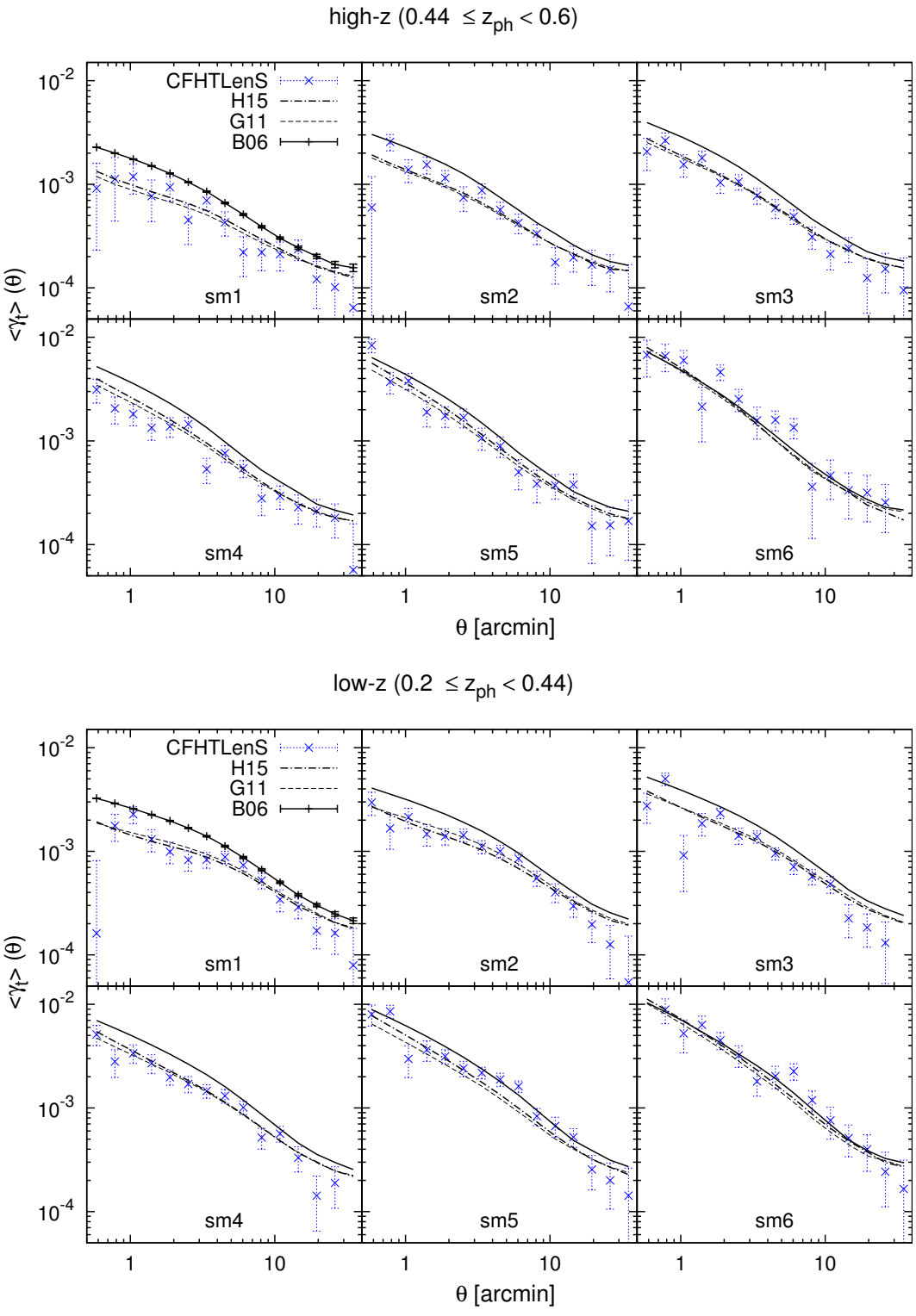

Figure 5.3: GGL as function of projected separation for the six stellar mass samples according to Table 5.1. The top panel corresponds to the high-z sample and the bottom panel to low-z. The data points with error bars (indicating the standard error of the mean over 129 fields) show the CFHTLenS measurements, which are compared to the predictions from the B06 (solid lines), G11 (dashed lines) and H15 (dash dotted lines). The B06 predictions for sm1 show the error of the mean over 64 fields.

To quantify the significance of the difference between model predictions and CFHTLenS measurements of $\langle\gamma_t\rangle$, we compute

$$\chi^2 = \left(\mathbf{d}^{\rm sam} - \mathbf{d}^{\rm obs}\right)^{\rm T} \mathbf{C}^{-1} \left(\mathbf{d}^{\rm sam} - \mathbf{d}^{\rm obs}\right) , \tag{5.6}$$

where $\mathbf{d}^{\rm sam}$ and $\mathbf{d}^{\rm obs}$ are data vectors containing the SAMs predictions and CFHTLenS measurements, respectively. The covariance matrix $\mathbf{C}$ of the difference signal is $\mathbf{C}^{\rm sam}+\mathbf{C}^{\rm obs}$ since SAMs and CFHTLenS measurements are uncorrelated. Here $\mathbf{C}^{\rm obs}$ is the Jackknife covariance of CFHTLenS measurements as explained in Appendix B1 of Simon et al. (2013), and $\mathbf{C}^{\rm sam}$ is the covariance matrix of SAMs estimated by

$$\mathbf{C}^{\rm sam}_{ij} = \frac{1}{N^{\rm sam}-1} \sum_{k=1}^{N^{\rm sam}} \left(d^{\rm sam}_{ik} - d^{\rm sam}_{i}\right)\left(d^{\rm sam}_{jk} - d^{\rm sam}_{j}\right) , \tag{5.7}$$

where $N^{\rm sam} = 64$ is the number of simulated fields and $d^{\rm sam}_{ik}$ is the measurement of the ith bin in θ in the kth simulated field with the mean

$$d^{\rm sam}_{i} = \frac{1}{N^{\rm sam}} \sum_{k=1}^{N^{\rm sam}} d^{\rm sam}_{ik}.$$

For our χ^2 test, we have $\mathbf{C} \simeq \mathbf{C}^{\rm obs}$ because the elements of the SAMs covariance matrix are negligible in comparison with the elements of the CFHTLenS covariance matrix. We apply the estimator of Hartlap et al. (2007) to obtain an estimator for the inverse of the covariance $\mathbf{C}^{-1}$ for $\mathbf{C}^{\rm obs}$,

$$\mathbf{C}^{-1} = \frac{N^{\rm obs} - P - 2}{N^{\rm obs} - 1} (\mathbf{C}^{\rm obs})^{-1}, \tag{5.8}$$

when $P < N^{\rm obs} - 2$. P is the total number of bins and $N^{\rm obs} = 129$ is the number of Jackknife realizations used for $\mathbf{C}^{\rm obs}$.

For $P = 15$ degrees of freedom, a tension between CFHTLenS and the SAM predictions with 95% confidence is given by values of $\chi^2/15 > 1.67$ (written in bold in Table 5.3). The results from Table 5.3 clearly show that the B06 model is in tension for all stellar mass bins except for sm5 in the high-z sample and sm6. In comparison to B06, the H15 and G11 models have lower χ^2 test values although they are also in tension for sm3 and sm5 at low-z.

Table 5.3: χ^2-test with 15 degrees-of-freedom applied to measurements of GGL shown in Fig. 5.3. Each number quotes $\chi^2/15$ for the corresponding model and stellar mass bin. Bold values indicate a tension between CFHTLenS and a SAM at 95% confidence level.

	low-z			high-z		
	G11	H15	B06	G11	H15	B06
sm1	1.25	1.27	**6.07**	0.68	0.71	**2.61**
sm2	0.54	0.56	**4.58**	1.26	1.23	**3.00**
sm3	**2.43**	**2.36**	**6.78**	0.45	0.46	**3.75**
sm4	0.93	1.11	**5.37**	1.11	1.64	**7.09**
sm5	**2.30**	**1.77**	**2.12**	1.06	0.88	1.62
sm6	1.26	0.97	1.00	**1.79**	1.63	1.49

5.5.2 G3L

The $\langle \mathcal{N}^2 M_{\rm ap} \rangle(\theta)$ values measured in CFHTLenS for the low-z and high-z samples in all stellar mass bins are shown in Fig. 5.4. Also shown there are the predictions from the SAMs. The observed $\langle \mathcal{N}^2 M_{\rm ap} \rangle(\theta)$ signal is dominated by the "transformation bias" below 1 arcmin and above 10 arcmin (Simon et al. 2008). This bias is caused by galaxy blending and the finite size of the observed field, thus leading to insufficient sampling of the three-point correlation function (Kilbinger et al. 2006). Therefore, only data points between $1' < \theta < 10'$ are used for comparison, indicated by the dashed vertical lines in the top left panel. We retain $P = 8$ data points for each stellar mass and redshift bin.

Our measurements show that the G11 and H15 predictions agree better with CFHTLenS than B06. The B06 model over-predicts the $\langle \mathcal{N}^2 M_{\rm ap} \rangle(\theta)$ signal in all but the highest stellar mass bin. In addition, the tension between B06 and CFHTLenS is more prominent for G3L than in the GGL measurements. The χ^2 test results can be found in Table 5.4. Model measurements with $\chi^2/8 > 1.94$, i.e. a SAM signal inconsistent with CFHTLenS (95% confidence) are written in bold.

To quantify the overall difference in G3L between the SAMs and CFHTLenS, we combine the measurements of all stellar mass samples and test for a vanishing difference signal consisting of $P = 48$ data points. Since data points between different stellar masses are correlated, we estimate a new 48×48 covariance by Jackknifing the combined bins in 129 CFHTLenS and for the 64 mock fields. The results of the χ^2 test are presented in Table 5.5. A tension between model and observation is now indicated by $\chi^2/48 > 1.35$ (95% confidence level). According to the χ^2 test, only the predictions of H15 for the low-z sample are in agreement with the CFHTLenS.

Table 5.4: Numbers indicate the χ^2-test values with 8 degrees-of-freedom applied to measurements of G3L shown in Fig. 5.4. Only data points between $1' < \theta < 10'$ were used for this test. Each number quotes $\chi^2/8$ for the corresponding model and stellar mass bin. Bold values indicate a tension between CFHTLenS and a SAM at 95% confidence level.

	low-z			high-z		
	G11	H15	B06	G11	H15	B06
sm1	0.88	1.33	**27.35**	**2.07**	1.73	**3.20**
sm2	**5.66**	**4.13**	**33.18**	1.27	1.39	**11.19**
sm3	1.69	0.29	**38.80**	1.15	0.99	**35.59**
sm4	1.43	0.81	**68.81**	1.31	1.19	**44.99**
sm5	1.24	1.26	**8.67**	1.57	1.57	**7.15**
sm6	0.59	0.63	0.71	1.70	1.59	1.48

Table 5.5: χ^2-test with 48 degrees-of-freedom applied to the measurements of G3L for all stellar mass samples combined. Only data points between $1' < \theta < 10'$ were used for this test. Tension between the models and CFHTLenS on a 95% confidence level are shown in bold.

	low-z			high-z		
	G11	H15	B06	G11	H15	B06
sm1-6	**2.56**	1.34	**27.73**	**2.18**	**2.08**	**12.88**

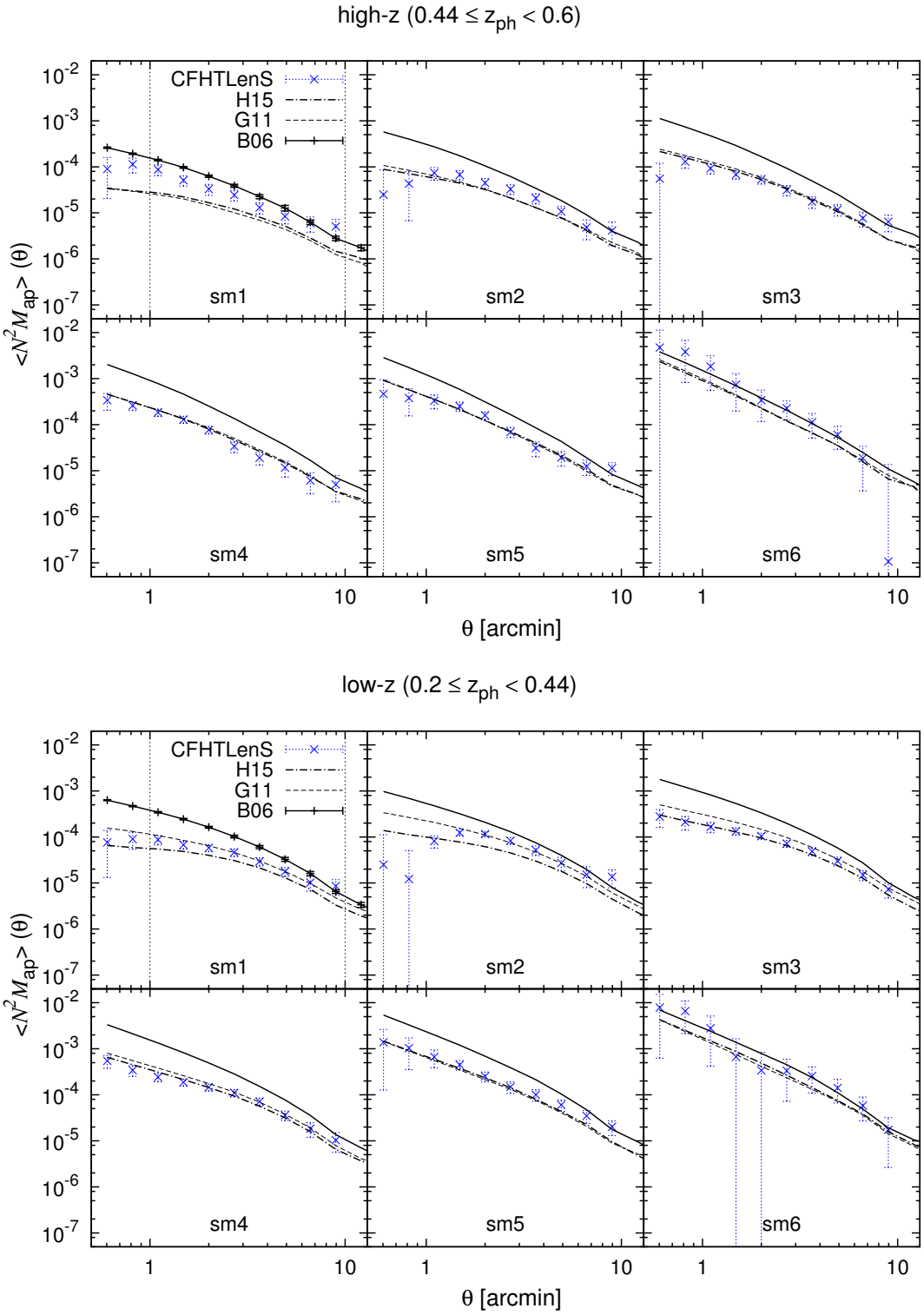

Figure 5.4: Measurements of the G3L aperture statistics as function of aperture scale θ in CFHTLenS (blue symbols) and SAMs (black curves). Measurements are presented for various stellar mass and redshift (high-z and low-z) samples. Error bars indicate the standard error of the mean. The dotted vertical lines show the limits of the range used for our χ^2 analysis.

5.5.3 Power-law fits

For aperture scales larger than 1.5 arcmin, the $\langle \mathcal{N}^2 M_{\rm ap} \rangle(\theta)$ measurements can be approximated by a power law. Therefore, we fit a power law function of form $A\theta^{-\alpha}$ according to the method by Simon et al. (2013). The power-law slopes α measured for all stellar mass bins are plotted in Fig. 5.5. The results indicate that the B06 model not only predicts a higher amplitude in $\langle \mathcal{N}^2 M_{\rm ap} \rangle$ measurements but also predicts steeper slopes than CFHTLenS. The H15 and G11 models are consistent with CFHTLenS, as can be seen in Fig. 5.5.

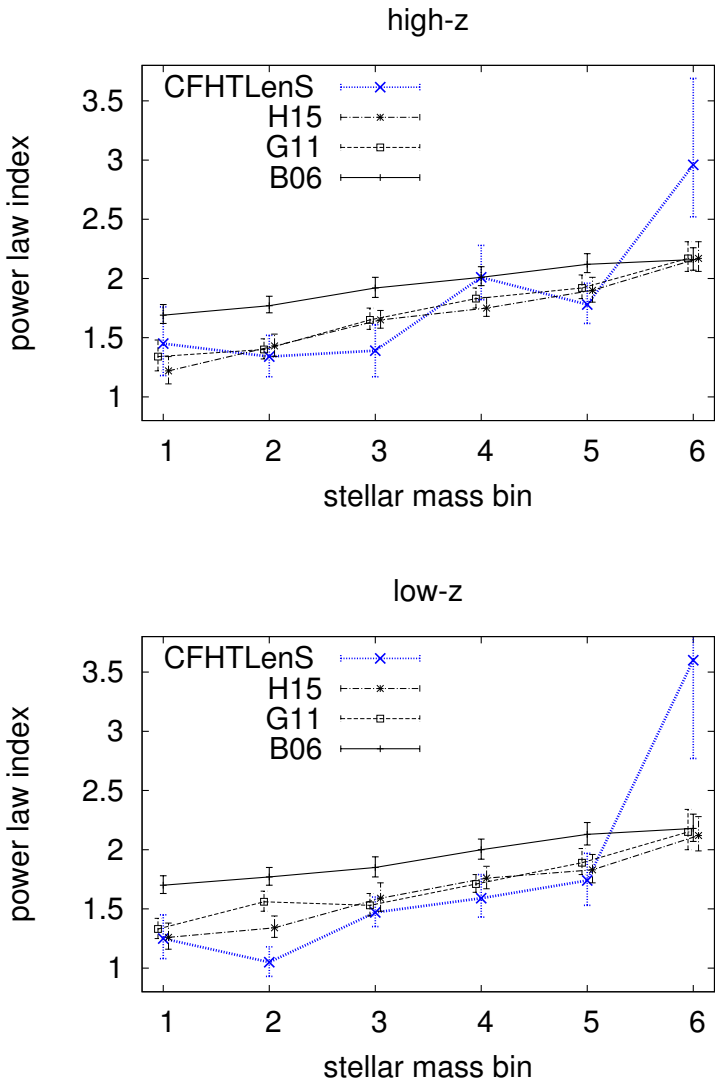

Figure 5.5: Slope of a power law fit to $\langle \mathcal{N}^2 M_{\rm ap} \rangle(\theta)$ between $1' < \theta < 10'$ in different stellar mass samples and for the high-z (top panel) and low-z (bottom panel) galaxies.

5.5.4 Stellar mass distribution

Given the foregoing results, we test if the stellar masses of galaxies are systematically different between the SAMs. For this purpose, we selected mock galaxies as described in Sect. 5.4.2 for a broad stellar mass bin including M_* from 5×10^{10} to $3.2 \times 10^{11} \mathrm{M}_\odot$ and plot the resulting distribution $\mathrm{d}N/\mathrm{d}\log M_*$ in Fig. 5.6 for 63 bins in M_*. The number of galaxies N in a bin is normalized by the total number $N_{\rm tot}$ in the plotted range. The ratios of the model predictions and the CFHTLenS results are shown in the upper panel of each plot. For comparison, we indicate on top of the plot labels corresponding to stellar mass samples sm1-sm6. The SAMs results are lower than that of CFHTLenS in high stellar mass bins, and their distributions drop more quickly. In low stellar mass bins, there are differences between G11 and B06 compared to H15, for instance there is a dip for B06 in the range sm2 to sm4 compared to H15. The stellar mass distribution of H15 is the closest to CFHTLenS.

5.6 Discussion

In this work, we have studied second- and third-order galaxy-mass correlation functions in terms of average tangential shear $\langle\gamma_{\rm t}\rangle$ and aperture statistics $\langle\mathcal{N}^2 M_{\rm ap}\rangle$, respectively. We used mock galaxies from B06, G11, and H15 which are SAMs implemented on the Millennium Simulation. We compared our results with the observational results of CFHTLenS for galaxies binned in stellar mass within $0.6 < M_*/10^{10}\mathrm{M}_\odot < 32$ and redshift within $0.2 \leq z_{\rm ph} \leq 0.6$. In addition, all lens galaxies are subject to a flux limit of $i'_{\rm AB} < 22.5$.

Our results indicate that not all models can reproduce the GGL and G3L observations although there is an overall qualitative agreement between the models and CFHTLenS as visible in the Fig. 5.3 and Fig. 5.4. All models best agree among each other and with CFHTLenS for sm6, i.e., for stellar masses of $\sim 2 \times 10^{11}\,\mathrm{M}_\odot$. However, the uncertainties of the CFHTLenS results are also largest here. At lower stellar masses, see Tables 5.3 and 5.4, B06 clearly over-predicts the amplitude of both GGL and G3L so that this model can be decisively excluded at the 95% confidence level. The agreement between G11, H15, and CFHTLenS, on the other hand, is good although the overall comparison to G3L still indicates some tension in Table 5.5. The fit of the more recent H15 is slightly better compared to G11. We also find from our χ^2 values that G3L has more discriminating power than GGL on the same data, as anticipated in Saghiha et al. (2012).

A systematically high galaxy-matter correlation in B06 might indicate that the stellar masses of B06 galaxies are systematically lower compared to G11 or H15. Such bias could impact the matter environment, clustering, and hence GGL and G3L of stellar-mass-selected galaxies. However, this is probably not the case here for the following reason. Knebe et al. (2015) compared the stellar mass function (SMF) at $z = 0$ in 14 various SAMs (including B06 and an earlier version of H15 by Henriques et al. 2013, H13). They studied whether SMF variations could be due to different initial mass functions (IMF) assumed in the models (B06 assumes a Kennicutt 1983 IMF while H15 and H13 use a Chabrier 2003 IMF). They transformed the stellar masses of galaxies using Chabrier IMF for all the models and showed that the scatter in SMF is only slightly changed by this transformation. Therefore, the specific IMFs of B06 and H15 or H13 are probably not the reason for the different lensing signals in our data. For our galaxy sample, we show the variations in the stellar mass distribution of galaxies between different SAMs (Fig. 5.6). We find that although both SMFs of B06 and G11 differ from that of H15, the GGL and G3L predictions of G11 and H15 are quite consistent, whereas there is a significant difference between the predictions of B06 and H15. This makes it unlikely that the discrepant predictions by B06 can be attributed to the somewhat different distribution of stellar masses.

Table 5.6: Mean satellite fraction and mean halo mass over 64 simulated fields for the high-z and low-z samples. The standard error of these mean values varies between 0.001 and 0.004 for the satellite fractions and between 0.1 and 0.4 for the halo masses.

high-z	Satellite fraction			Halo mass [$10^{13}M_\odot/h$]		
	G11	H15	B06	G11	H15	B06
sm1	0.28	0.29	0.30	2.6	2.8	4.2
sm2	0.33	0.32	0.34	3.1	3.3	4.6
sm3	0.36	0.33	0.35	3.6	3.8	5.3
sm4	0.35	0.32	0.36	4.2	4.6	6.1
sm5	0.32	0.30	0.34	4.9	5.4	6.7
sm6	0.28	0.27	0.31	6.4	6.3	6.9

low-z	Satellite fraction			Halo mass [$10^{13}M_\odot/h$]		
	G11	H15	B06	G11	H15	B06
sm1	0.38	0.34	0.38	3.8	3.8	5.6
sm2	0.41	0.35	0.39	4.2	4.2	6.0
sm3	0.40	0.35	0.37	4.7	4.8	6.9
sm4	0.37	0.33	0.37	5.3	5.5	7.8
sm5	0.33	0.31	0.35	5.9	6.4	8.5
sm6	0.29	0.28	0.32	7.4	7.7	8.7

The discrepancies in model prediction of the lensing signals indicate model variations in the galaxy-matter correlations. It reflects the variations in the way galaxies are distributed among the dark matter halos. This argument is in agreement with the results presented in Kim et al. (2009) and Saghiha et al. (2012) who attributed this trend in B06 to the generation of too many satellite galaxies in massive halos. Indeed, the mean halo masses are higher in B06 than in G11 and H15 for all stellar masses but sm6 and the satellite fraction is somewhat higher for B06 (Table 5.6). One main general difference between the B06 and G11 (H15) models is the definition of independent halos and the way descendants of the halos are identified in the merger trees. These differences have an impact on the treatment of some physical processes such as mergers which, in turn, influence the abundance of satellites in halos. Using a halo model description, Watts & Schneider (2005) showed that the galaxy-matter power spectrum, and hence the GGL signal, increases in amplitude when the mean number of galaxies inside halos of a specific mass scale is increased. Similarly, the galaxy-galaxy-matter bispectrum, hence G3L, increases in amplitude if the the number of galaxy pairs is increased for some mass scale. Therefore, an over-production of satellite galaxies in massive halos can explain the relatively high signal of GGL and G3L in B06. This interpretation is supported by the higher mean mass of parent halos of galaxies in B06 compared to G11 or H15 as shown in Table 5.6.

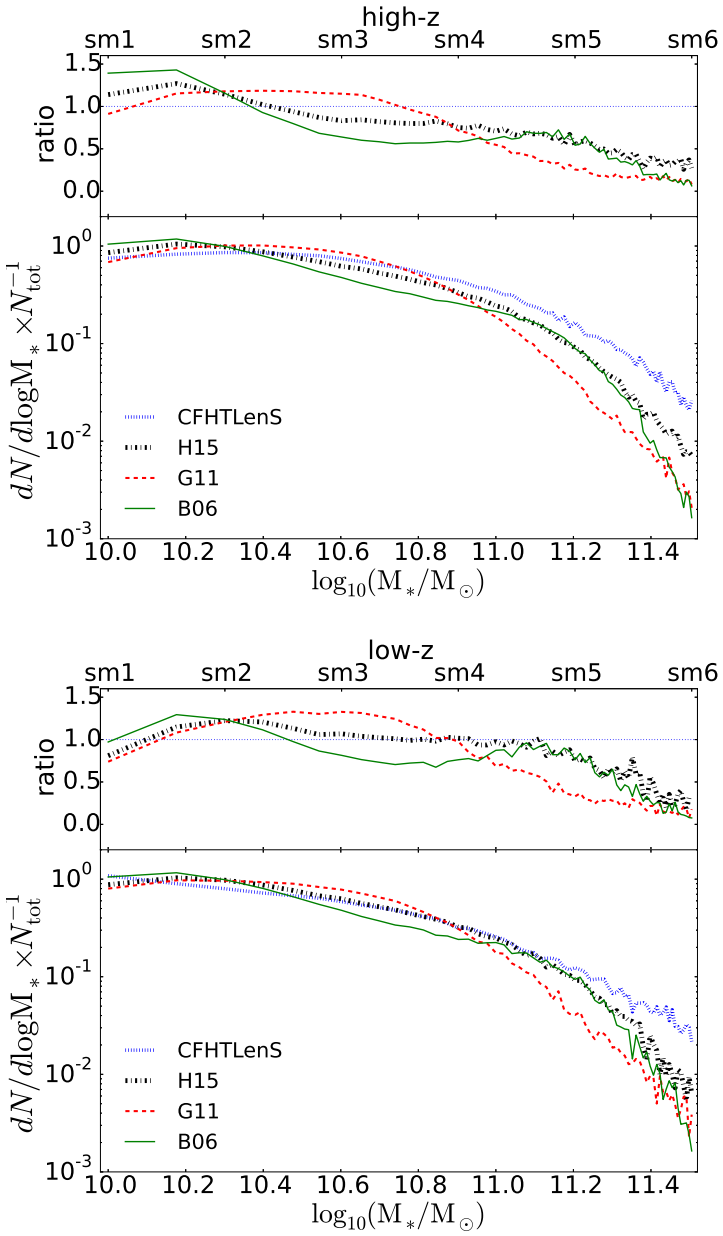

Figure 5.6: The stellar mass function of galaxies normalized with the total number of galaxies in all three SAMs and CFHTLenS. We used a sample of sm1 to sm6 combined and repeated the three-step selection in Sect. 5.4.2 to produce high-z (top figure) and low-z (bottom figure) subsamples. The top of each panel shows the ratio between the SAM and CFHTLenS stellar mass function.

CHAPTER 6

Mapping the matter density distribution

The three-point correlation function $\mathcal{G}$ quantifies the excess in the average shear profile around galaxy pairs relative to the average profile around individual galaxies. In the previous chapters, $\mathcal{G}$ was studied with the third-order aperture statistics $\left\langle \mathcal{N}^2 M_{\rm ap} \right\rangle$. Third-order aperture statistics quantifies the third-order moments of fluctuations in the smoothed projected galaxy and matter density fields. We studied the matter environment of galaxy pairs using $\left\langle \mathcal{N}^2 M_{\rm ap} \right\rangle$ and showed that it is sensitive to the galaxy population under consideration. Aperture statistics is useful to obtain information on the statistical properties of the common dark matter halo of galaxy pairs. However, questions such as *what is the shape of the mass distribution around galaxy pairs*, *is it different for different samples of galaxy pairs*, or *is it isotropic*, can not be answered using $\left\langle \mathcal{N}^2 M_{\rm ap} \right\rangle$. In this chapter we use an alternative approach to obtain $\mathcal{G}$ and to answer these questions.

In Johnston (2006), a method was introduced to map the shear profile around lens galaxy pairs. This method was further applied by Simon et al. (2008) to galaxy pairs with fixed angular separation in the Red-sequence Cluster Survey (RCS, Gladders & Yee 2005). The shear map is converted into a projected convergence (matter density) map using the Kaiser-Squires relation (see Sect. 3.2). Then, one can define the "excess mass map", which is related to the average excess in the projected matter density around lens pairs, the average matter density profile of individual lenses, and the clustering of the lenses. As an example, we show in Fig. 6.1 the excess mass map measurements from Simon et al. (2008) for a sample of galaxies in the RCS. The difference between the left and right panel is the separation between the lenses. The figure shows that when the lenses are not too far apart, they live in a common dark matter halo whose mass is more than only the sum of their individual halos. In the following, we summarize the basics of the method used to obtain excess mass maps using galaxies from the SAMs catalogues and CFHTLenS data.

6.1 Excess mass maps

The excess mass map or *convergence* connected to an average galaxy pair is defined by

$$\left\langle \kappa_{\rm g}(\boldsymbol{\theta}_1)\kappa_{\rm g}(\boldsymbol{\theta}_2)\kappa(\boldsymbol{\theta}_3) \right\rangle = \frac{\langle N(\boldsymbol{\theta}_1)N(\boldsymbol{\theta}_2)\kappa(\boldsymbol{\theta}_3)\rangle}{\bar{N}^2} - \bar{\kappa}_{\rm ind}(\theta_{13}) - \bar{\kappa}_{\rm ind}(\theta_{23}) \; . \tag{6.1}$$

In this equation, the lenses are distributed according to the underlying number density field $N(\boldsymbol{\theta})$ (Eq. 3.23) with mean number density $\bar{N}$ (Eq. 3.24), and $\kappa_{\rm g}(\boldsymbol{\theta})$ is their fractional number density contrast (Eq. 3.26).

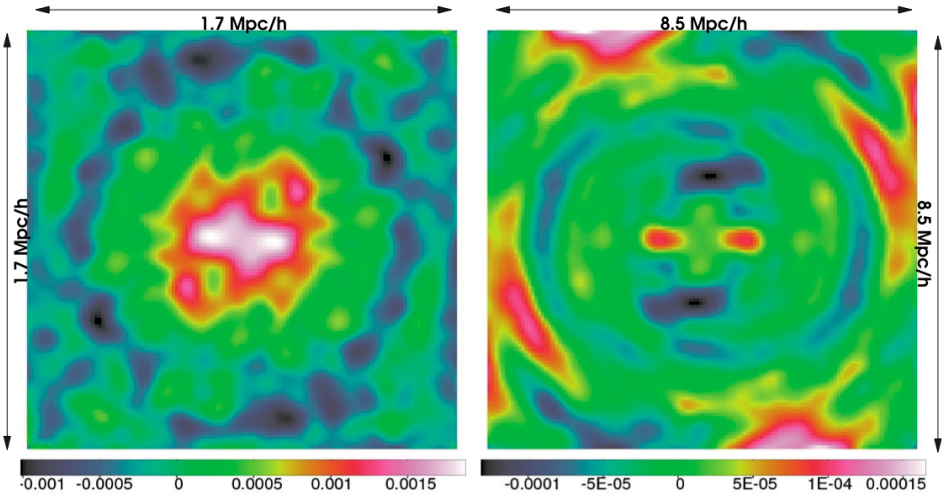

Figure 6.1: The excess mass map measured in the RCS (Simon et al. 2008). Lens pairs have angular separation between 40 and 80 arcsec (4 and 8 arcmin) corresponding to a projected physical scale of about $250h^{-1}$kpc ($1.5h^{-1}$Mpc) in the left (right) panel. The entire map corresponds to a projected physical scale of about $1.7h^{-1}$Mpc $\times$ $1.7h^{-1}$Mpc ($8.5h^{-1}$Mpc $\times$ $8.5h^{-1}$Mpc) in the left (right) panel.

The average convergence around an individual lens $\bar{\kappa}_{\rm ind}(\theta_{i3})$ with $i = 1, 2$ is denoted by

$$\bar{\kappa}_{\rm ind}(\theta_{i3}) = \frac{\langle N(\boldsymbol{\theta}_i)\kappa(\boldsymbol{\theta}_3)\rangle}{\bar{N}}\,. \tag{6.2}$$

Using the definition of the angular clustering of galaxies (Eq. 3.45), we can rewrite Eq. (6.1) into

$$\Big\langle \kappa_{\rm g}(\boldsymbol{\theta}_1)\kappa_{\rm g}(\boldsymbol{\theta}_2)\kappa(\boldsymbol{\theta}_3)\Big\rangle = \Big(1 + w_{\rm gg}(\theta_{12})\Big)\frac{\langle N(\boldsymbol{\theta}_1)N(\boldsymbol{\theta}_2)\kappa(\boldsymbol{\theta}_3)\rangle}{\langle N(\boldsymbol{\theta}_1)N(\boldsymbol{\theta}_2)\rangle} - \bar{\kappa}_{\rm ind}(\theta_{13}) - \bar{\kappa}_{\rm ind}(\theta_{23})\,, \tag{6.3}$$

in which appears the average convergence around galaxy pairs of fixed separation θ_{12},

$$\bar{\kappa}_{\rm pair}(\boldsymbol{\theta}_1, \boldsymbol{\theta}_2; \boldsymbol{\theta}_3) := \frac{\langle N(\boldsymbol{\theta}_1)N(\boldsymbol{\theta}_2)\kappa(\boldsymbol{\theta}_3)\rangle}{\langle N(\boldsymbol{\theta}_1)N(\boldsymbol{\theta}_2)\rangle}\,. \tag{6.4}$$

The $\langle ...\rangle$ symbol denotes the ensemble average, i.e. the average over many realizations of the random field for triplets of galaxies located at $\boldsymbol{\theta}_1$, $\boldsymbol{\theta}_2$, and $\boldsymbol{\theta}_3$ on the sky. Matter density and galaxy number density fields are ergodic random fields. Using the ergodicity of these random fields, we can thus replace the ensemble average by spatial average. Therefore, $\langle N(\boldsymbol{\theta}_1)N(\boldsymbol{\theta}_2)\kappa(\boldsymbol{\theta}_3)\rangle$ can be replaced by a spatial average of $N(\boldsymbol{\theta}_1)N(\boldsymbol{\theta}_2)\kappa(\boldsymbol{\theta}_3)$ over the entire field for all triangles of galaxies with the same geometry as the triangle made by triplet of galaxies at $\boldsymbol{\theta}_1$, $\boldsymbol{\theta}_2$, and $\boldsymbol{\theta}_3$.

In order to understand why the left hand side of the Eq. (6.4) equals the average convergence around two lens galaxies, one should consider the number density field of lenses projected on a regular grid with a large number of *microcells*, each with an area σ. Each microcell is fine enough to contain either no lens or one lens ($\int_\sigma {\rm d}\sigma N(\boldsymbol{\theta}) = 0$ or 1). We have a contribution to the average convergence only for $\int {\rm d}\sigma N(\boldsymbol{\theta}_1) = \int {\rm d}\sigma N(\boldsymbol{\theta}_2) = 1$, while $\langle N(\boldsymbol{\theta}_1)N(\boldsymbol{\theta}_2)\rangle$ is the probability of having a cell pair with $\int {\rm d}\sigma N(\boldsymbol{\theta}_1) = \int {\rm d}\sigma N(\boldsymbol{\theta}_2) = 1$ (normalisation factor).

By injecting Eq. (6.4) into Eq. (6.3), we can rewrite the excess mass map as:

$$\left\langle \kappa_{\rm g}(\boldsymbol{\theta}_1)\kappa_{\rm g}(\boldsymbol{\theta}_2)\kappa(\boldsymbol{\theta}_3)\right\rangle = \Big(1 + w_{\rm gg}(\theta_{12})\Big)\,\bar{\kappa}_{\rm pair}(\boldsymbol{\theta}_1, \boldsymbol{\theta}_2; \boldsymbol{\theta}_3) - \bar{\kappa}_{\rm ind}(\theta_{13}) - \bar{\kappa}_{\rm ind}(\theta_{23})\,. \tag{6.5}$$

6.2 Methods

The synthetic data contains the convergence to the sources $\kappa(\boldsymbol{\theta})$ and the galaxy number density field of lenses $N(\boldsymbol{\theta})$, which are both projected on a regular grid. The 2D sky positions are denoted by $\boldsymbol{\theta}$. The estimator for the $\bar{\kappa}_{\rm pair}$ is obtained by stacking the convergence field around lens galaxy pairs with a certain fixed separation or a separation within a small range.

We use an affine transformation to map the convergence field around lens pairs. An affine transformation is a combination of a linear transformation and a translation. Each position $\boldsymbol{\theta}$ is transformed to $\boldsymbol{\vartheta}$ following the relation

$$\boldsymbol{\vartheta} = a\boldsymbol{\theta} + \boldsymbol{b}\,,$$

where a represents the linear transformation corresponding to a rotation and scaling while $\boldsymbol{b}$ represents the translation. The rotation places the lenses in the field such that the line connecting two lenses is along the x-axis while the translation vector bring this line to the center of the field. The scaling is required for placing lenses at a fix separation in the field. Given the positions of galaxy pairs before and after transformation, we can calculate a and $\boldsymbol{b}$ for each pair. The transformation matrix a can be written as

$$a = S\begin{bmatrix}\cos(\alpha) & -\sin(\alpha)\\ \sin(\alpha) & \cos(\alpha)\end{bmatrix} \tag{6.6}$$

where S represent the scaling which is multiplied by the rotation matrix corresponding to an angle α.

Let us denote the 2D positions of the two lens galaxies before the transformation $\boldsymbol{\theta}_1 = \begin{bmatrix}\theta_{1x}\\ \theta_{1y}\end{bmatrix}$ and $\boldsymbol{\theta}_2 = \begin{bmatrix}\theta_{2x}\\ \theta_{2y}\end{bmatrix}$, and after the transformation $\boldsymbol{\vartheta}_1 = \begin{bmatrix}\vartheta_{1x}\\ \vartheta_{1y}\end{bmatrix}$ and $\boldsymbol{\vartheta}_2 = \begin{bmatrix}\vartheta_{2x}\\ \vartheta_{2y}\end{bmatrix}$. Using the vector notation, the affine transformation can be written as

$$\begin{bmatrix}\vartheta_{1x}\\ \vartheta_{1y}\end{bmatrix} = S\begin{bmatrix}\cos(\alpha) & -\sin(\alpha)\\ \sin(\alpha) & \cos(\alpha)\end{bmatrix}\begin{bmatrix}\theta_{1x}\\ \theta_{1y}\end{bmatrix} + \begin{bmatrix}b_x\\ b_y\end{bmatrix} \tag{6.7}$$

$$\begin{bmatrix}\vartheta_{2x}\\ \vartheta_{2y}\end{bmatrix} = S\begin{bmatrix}\cos(\alpha) & -\sin(\alpha)\\ \sin(\alpha) & \cos(\alpha)\end{bmatrix}\begin{bmatrix}\theta_{2x}\\ \theta_{2y}\end{bmatrix} + \begin{bmatrix}b_x\\ b_y\end{bmatrix}.$$

Separating the equations, we can write

$$\begin{aligned}\vartheta_{1x} &= a_x\theta_{1x} - a_y\theta_{1y} + b_x\\ \vartheta_{2x} &= a_x\theta_{2x} - a_y\theta_{2y} + b_x\\ \vartheta_{1y} &= a_x\theta_{1y} + a_y\theta_{1x} + b_y\\ \vartheta_{2y} &= a_x\theta_{2y} + a_y\theta_{2x} + b_y\,,\end{aligned} \tag{6.8}$$

where

$$a_x = S\cos(\alpha) \qquad \text{and} \qquad a_y = S\sin(\alpha)\,. \tag{6.9}$$

Finally, we can calculate a_x and a_y by solving the set of equations in Eq. (6.8) as

$$\begin{aligned} a_x &= \frac{\Delta\boldsymbol{\theta} \cdot \Delta\boldsymbol{\vartheta}}{|\Delta\boldsymbol{\theta}|^2} \\ a_y &= \frac{\Delta\boldsymbol{\theta} \times \Delta\boldsymbol{\vartheta}}{|\Delta\boldsymbol{\theta}|^2}\,, \end{aligned} \tag{6.10}$$

where $\Delta\boldsymbol{\theta} = \boldsymbol{\theta}_1 - \boldsymbol{\theta}_2$ and $\Delta\boldsymbol{\vartheta} = \boldsymbol{\vartheta}_1 - \boldsymbol{\vartheta}_2$. By substituting a_x and a_y in Eq. (6.8), b_x and b_y can be expressed as follows:

$$\begin{aligned} b_x &= \vartheta_{1x} - \theta_{1x}\left(\frac{\Delta\boldsymbol{\theta} \cdot \Delta\boldsymbol{\vartheta}}{|\Delta\boldsymbol{\theta}|^2}\right) + \theta_{1y}\left(\frac{\Delta\boldsymbol{\theta} \times \Delta\boldsymbol{\vartheta}}{|\Delta\boldsymbol{\theta}|^2}\right) \\ b_y &= \vartheta_{1y} - \theta_{1y}\left(\frac{\Delta\boldsymbol{\theta} \cdot \Delta\boldsymbol{\vartheta}}{|\Delta\boldsymbol{\theta}|^2}\right) - \theta_{1x}\left(\frac{\Delta\boldsymbol{\theta} \times \Delta\boldsymbol{\vartheta}}{|\Delta\boldsymbol{\theta}|^2}\right)\,. \end{aligned} \tag{6.11}$$

Applying this mapping technique to all galaxy pairs and stacking the convergence field around pairs and calculating resulting average convergence yields $\bar{\kappa}_{\rm pair}$. A schematic of the stacking of the convergence field around lens pairs is shown in the the right panel of Fig. 6.2.

To obtain a map of the average convergence around individual lenses in a similar way as for the convergence map around lens pairs, we proceed as follows. For each lens galaxy with position $\boldsymbol{\theta}_1$ we randomly select the position $\boldsymbol{\theta}_2$ for a second "imaginary" lens that satisfies the relation $\boldsymbol{\theta}_2 = \boldsymbol{\theta}_1 + \delta\theta\, \mathrm{e}^{\mathrm{i}\phi}$, where ϕ defines a random orientation ($\phi \in [0, 2\pi]$) and $\delta\theta$ is the separation between the lens galaxy and the imaginary lens. This separation is selected randomly from the distribution of lens-lens separations obtained when calculating $\bar{\kappa}_{\rm pair}$. Then we use the affine transformation as before. By using this method, we obtain $\bar{\kappa}_{\rm ind}$ and $\bar{\kappa}_{\rm pair}$ maps in a consistent manner.

A schematic of the stacking of the convergence field around individual lenses is shown in the the left panel of Fig. 6.2. Each galaxy in the simulated field, is mapped in such a way that it is located once at the position of the first lens and once at the position of the second lens (the two red dots in the small map). Therefore, by stacking the convergence field around each lens and calculating the resulting average convergence one finds $\bar{\kappa}_{\rm ind}(\theta_{13})$ for the first lens and $\bar{\kappa}_{\rm ind}(\theta_{23})$ for the second lens.

In order to estimate the excess mass (Eq. 6.3), the remaining ingredient needed is an expression for the angular clustering of galaxies $w_{\rm gg}$. For a simulated field with area A consisting of $N_{\rm g}$ galaxies, the mean number density is $\bar{N}_{\rm g} = N_{\rm g}/A$. For such field, the number of galaxy pairs with separation between θ and $\theta + \Delta\theta$ is $2A\pi\,\bar{N}_{\rm g}\,\theta\,\Delta\theta\,\bar{N}_{\rm g}$. If we call $N_p(\theta)$ the true number of pairs, the clustering of lens galaxies becomes

$$(1 + w_{\rm gg}(\theta)) = \frac{N_p(\theta)}{2A\pi\,\bar{N}_{\rm g}\,\theta\,\Delta\theta\,\bar{N}_{\rm g}}\,. \tag{6.12}$$

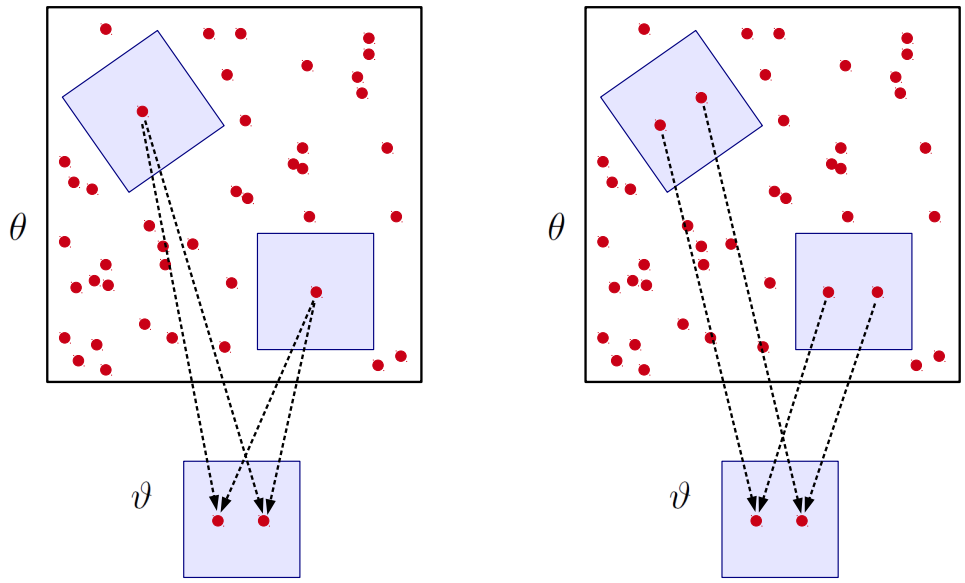

Figure 6.2: Left: Schematic of the stacking of the convergence field around individual lenses. Each galaxy is mapped such that it is located once at the position of first lens and once at the position of the second lens (shown by the two red spheres in the small map). Averaging the κ values then results in a $\overline{\kappa}_{\rm ind}$. Right: Schematic of the stacking of the convergence field around lens pairs. Galaxy pairs are mapped such that they have a separation of 30 pixels. A $\overline{\kappa}_{\rm pair}$ map is the average of κ values in each pixels.

6.3 Results

We use galaxy properties from the SAMs mock galaxy catalogues and the convergence field from the Millennium simulation. The convergence field $\kappa(\boldsymbol{\theta})$ of the source galaxies and the lens galaxy number density fields are projections of the density fields simulated on square meshes of 4096^2 pixels. The convergence fields are obtained directly from the ray-tracing algorithm and the galaxy density fields are obtained by projecting the apparent position of the lens galaxies in the fields and counting the number of galaxies in each pixel.

We compute the excess mass map using B06, G11, and H15 SAMs. We select lens galaxies with stellar masses $0.5 \leq M_*/10^{10}\mathrm{M}_\odot < 32$ for the high$-z$ ($0.44 \leq z_{\rm ph} < 0.6$) and the low$-z$ ($0.2 \leq z_{\rm ph} < 0.44$) samples. We used the three steps explained in Sect. 5.4.2 to obtain lens galaxy samples with the same redshift distribution as CFHTLenS. To compare our models with observations, we use the mean convergence to the sources with the redshift distribution according to the redshift distribution of sources in CFHTLenS with mean redshift $z = 0.9$. We use all 64 simulated fields of $4 \times 4\,\mathrm{deg}^2$ each. To compute the excess mass map we select lens pairs with separation between 0.53 and 1.04 arcmin (0.66 and 1.3 arcmin) for the the high$-z$ (low$-z$) sample, respectively. We recall that after the affine transformation, lenses have fixed positions with separation 30 pixels. The maps have size of 100^2 pixels which corresponds to about $(2.7\,\mathrm{arcmin})^2$ for the high$-z$ sample, and $(3.3\,\mathrm{arcmin})^2$ for the low$-z$ sample.

The CFHTLenS excess mass map is measured by stacking the shear field around lenses and using the Kaiser-Squires (KS) relation (Eq. 3.18) in Fourier space to convert the shear fields to the convergence field. The transformation in the Fourier space is done using a Fast Fourier Transform (FFT) method. Two artificial effects can be observed when using the KS transformation. First, artefacts at the boundaries appear because the KS inversion from shear to convergence requires data on an infinite space whereas the CFHTLenS data is available on a finite field which makes the boundary effects unavoidable. Second effect is that inversion from shear to convergence in KS relation is unique only up to an additive constant. This is because adding a constant convergence does not change the shear, a problem known as *mass sheet degeneracy*. To account for this effect and to be able to compare the SAMs with the CFHTLenS, we subtract the central pixel value from all pixel values over the entire map.

In order to be consistent with CFHTLenS, all maps predicted by SAMs must be smoothed. For each pixel (i, j), the convergence is smoothed using a Gaussian function w centred at the pixel and with standard deviation $\sigma = 3$ pixels. The convergence in the smoothed map at the pixel $\kappa^{i,j}_{\rm smooth}$ is then:

$$\kappa^{i,j}_{\rm smooth} = \frac{\sum_{m,n} \kappa^{m,n} w(d^{i,j}_{m,n})}{\sum_{m,n} w(d^{i,j}_{m,n})},$$

where $\kappa^{m,n}$ is the convergence at pixel (m, n) in the original map, $w(d) = \mathrm{e}^{-d^2/2\sigma^2}$ is the weight function and $d^{i,j}_{m,n}$ is the separation (on the sky) between pixels (i, j) and (m, n).

Taking into account these considerations and using the method described in Sect. 6.2, we make predictions of the excess mass maps. The results shown in Fig. 6.3 and Fig. 6.4 correspond to the high$-z$ and low$-z$ samples, respectively. In order to verify the codes used to compute the excess mass map in the SAMs and CFHTLenS, we have run the code used for the CFHTLenS measurements but with the SAMs galaxy samples. The results are shown in Fig. 6.5 and Fig. 6.6 for the high$-z$ and low$-z$ samples.

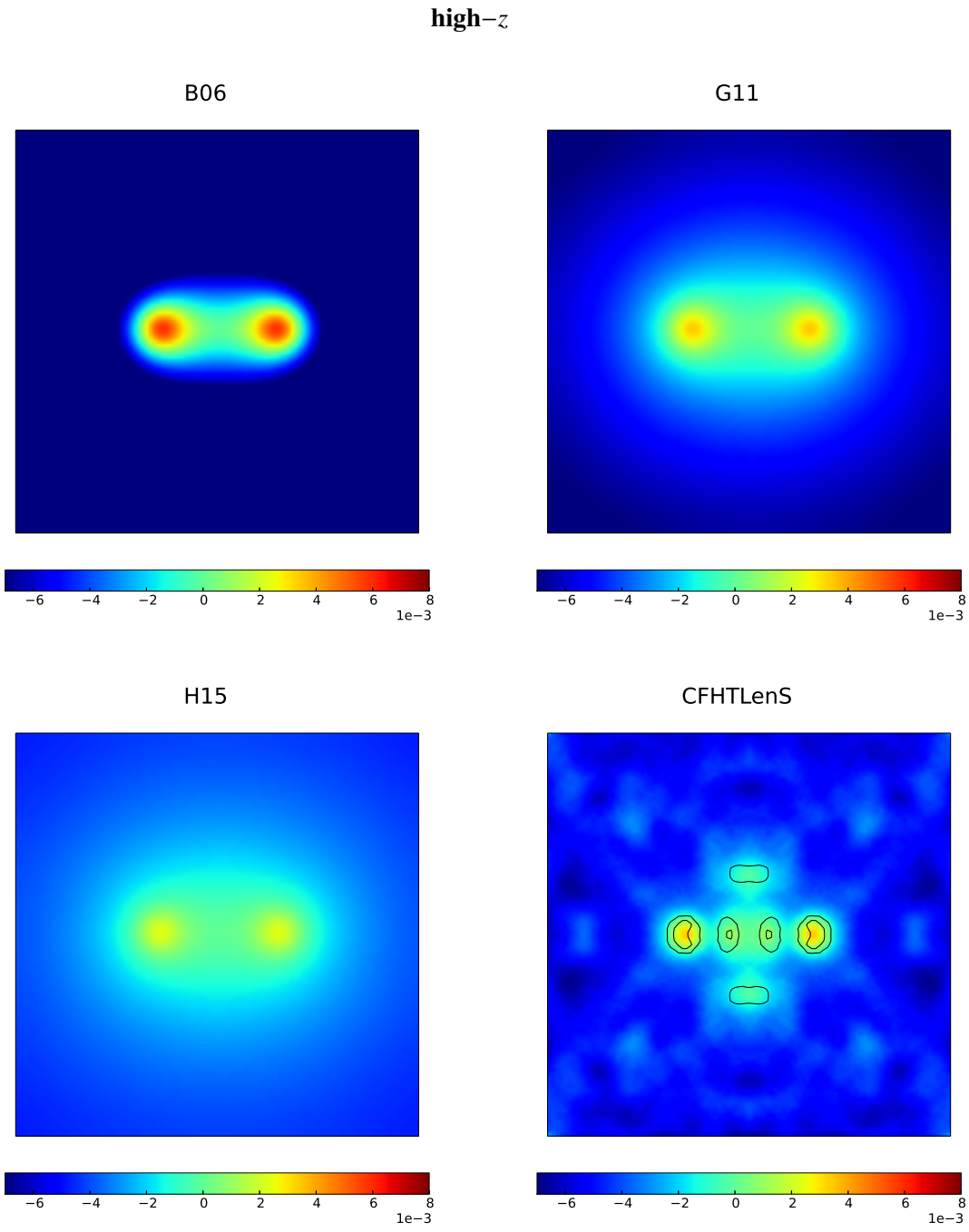

Figure 6.3: The excess mass map (intensity scale) obtained by stacking the convergence field around lenses shown for H15, G11, and B06 models. The CFHTLenS map is obtained by stacking the shear field around lenses and then applying a transformation to obtain the convergence field. Galaxies are selected from the high$-z$ sample and have separations between 0.53 and 1.04 arcmin. The map is 100^2 pixels large, corresponding to $(2.7\,\mathrm{arcmin})^2$. The contours show the signal-to-noise levels 4, 5, 6.

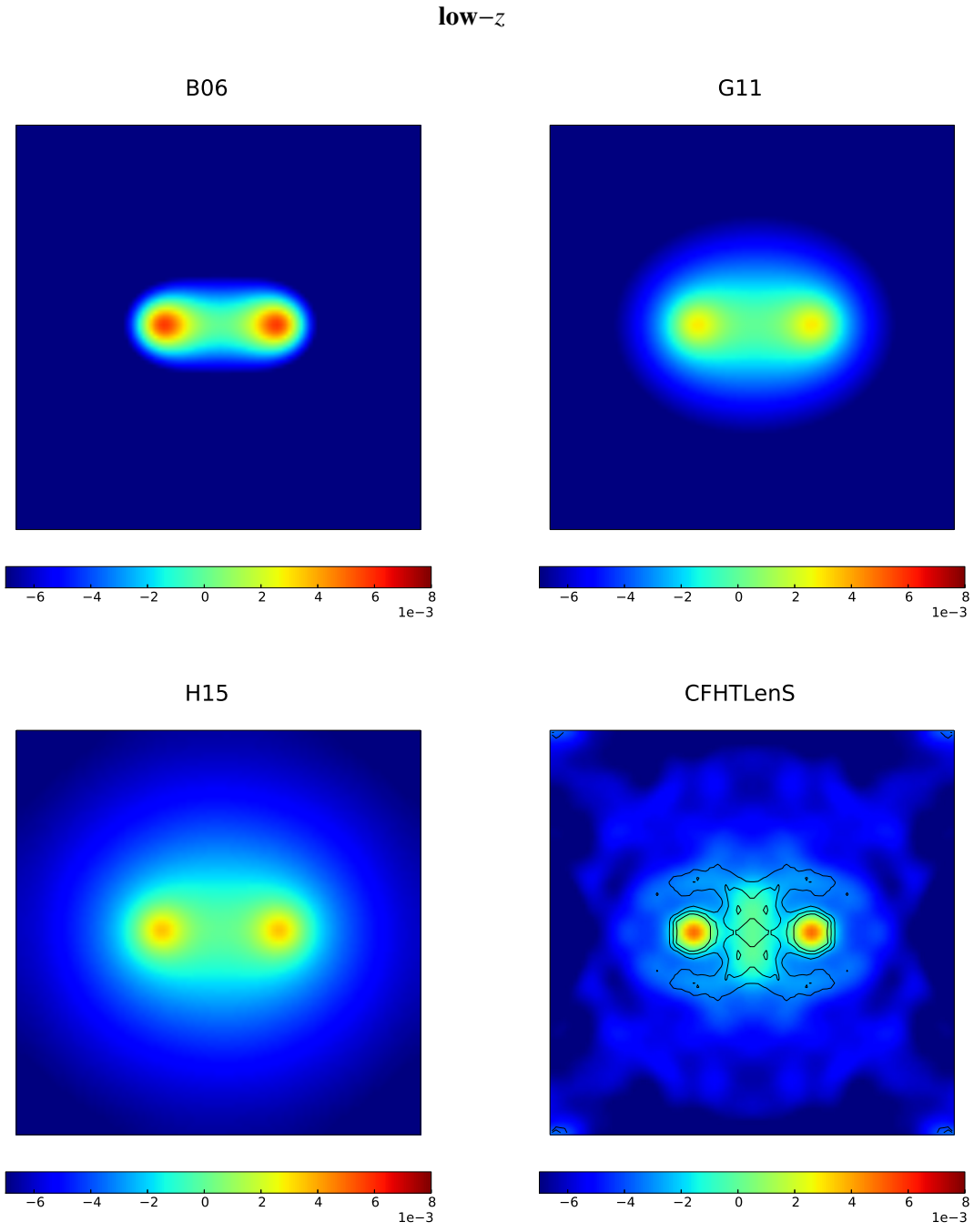

Figure 6.4: Same as Fig. 6.3 but lenses are selected from the low−z sample with angular separations between 0.66 and 1.3 arcmin. The map is 100^2 pixels large, corresponding to $(3.3\,\mathrm{arcmin})^2$.

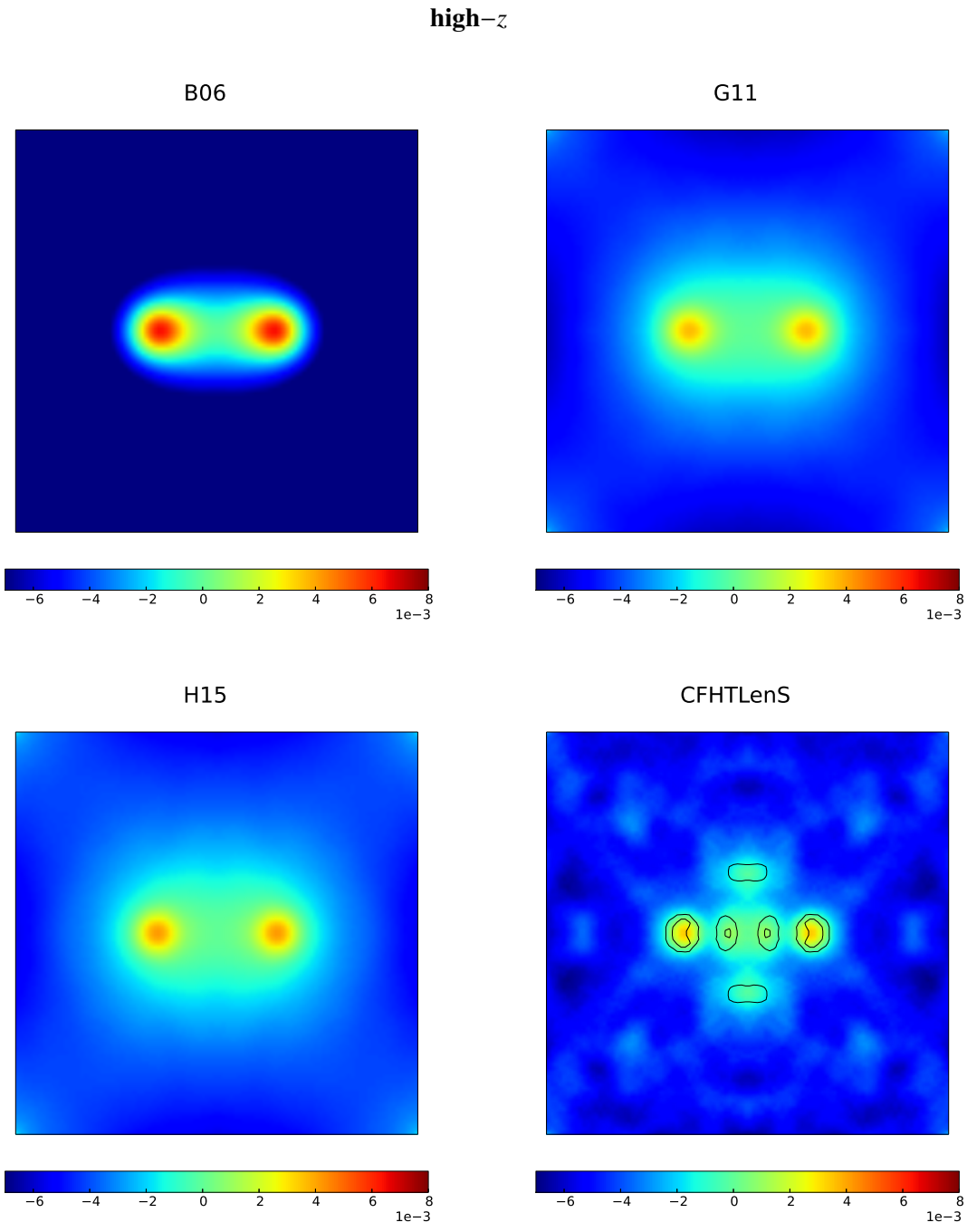

Figure 6.5: The excess mass map obtained by transforming the stacked shear fields to the convergence fields. The model results are obtained by applying the same method as for the CFHTLenS, as opposed to Fig. 6.3 which uses the method explained in Sect. 6.2. Lenses have separations between 0.53 and 1.04 arcmin and are selected from the high−z sample. The map is 100^2 pixels large, corresponding to $(2.7\,\mathrm{arcmin})^2$. The contours show the signal-to-noise levels 4, 5, 6.

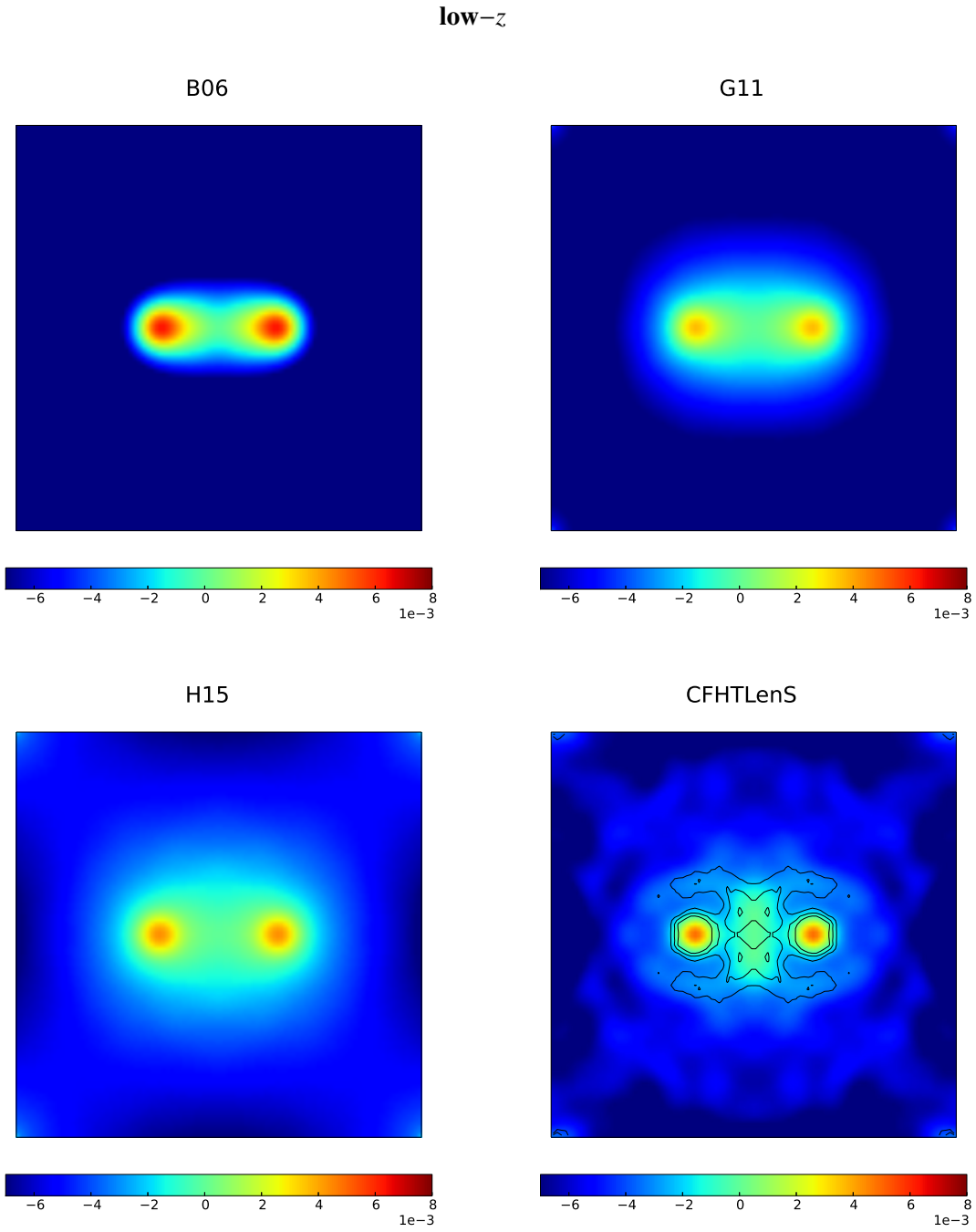

Figure 6.6: Same as Fig. 6.5 but lenses have separations between 0.66 and 1.3 arcmin and are selected from the low−z sample. The map is 100^2 pixels large, corresponding to $(3.3\,\mathrm{arcmin})^2$.

6.4 Discussion

The results presented in Fig. 6.3 and Fig. 6.4 show that the average excess in the convergence around two lenses of fixed separation predicted by B06 model is larger than that from the CFHTLenS measurements. This is seen in both high-z and low-z samples. Given that the results predicted by applying two independent codes (see e.g. Fig. 6.3 and Fig. 6.5) agree on the amplitude of the average convergence, the discrepancy between the B06 and CFHTLenS must be due to differences in the distribution of galaxies in dark matter halos. The G11 model also predicts higher convergence values compared to the CFHTLenS maps in the high-z sample, however to a lesser degree. Among all the models, the H15 model shows the best agreement with the CFHTLenS measurements when comparing the amplitude of the convergence values in the maps.

We recall that the excess mass maps and $\left\langle \mathcal{N}^2 M_{\rm ap} \right\rangle$ are both representations of $\mathcal{G}$. In the previous chapter we showed that the B06 predicts higher $\left\langle \mathcal{N}^2 M_{\rm ap} \right\rangle$ signal in both redshift bins and that the H15 model is in better agreement with CFHTLenS compared to the other models. Hence, our results obtained with the excess mass maps agree with the results presented in the previous chapter.

Apart from these differences, the CFHTLenS maps contain more structure compared to the models. There is significant excess mass centred between the two lenses in CFHTLenS in both high-z and low-z samples. These features are not seen in the model predictions. Also, for the CFHTLenS measurements we depict the signal-to-noise levels 4, 5, 6. These CFHTLenS noise maps represent the Jackknife field to field variance, and show contributions from the shape noise, the shot noise, and the cosmic variance. In comparison, the cosmic variance is the only noise component present in the simulations. Given the high signal-to-noise ratio between the two lenses in CFHTLenS, it would be important to understand the structures seen in the CFHTLenS data.

To further investigate these maps, the first step would be to analyze the excess mass maps for various lens-lens separations. Another approach would be to compare directly the shear maps such that the effects due to the transformation from the shear to convergence will not be present. Certainly, follow-up investigations are necessary before one can fully understand these results and their intrinsic differences.

CHAPTER 7

Summary and outlook

Summary

In this thesis, we used weak gravitational lensing to investigate the second-order and third-order correlations in the galaxy and matter density fields. These correlation functions correspond to galaxy-galaxy and galaxy-galaxy-galaxy lensing (GGL and G3L), respectively. We used one of the largest dark matter N-body simulations, the Millennium Simulation in combination with semi-analytical models (SAMs) of galaxy formation. We used the SAMs of Bower et al. (2006, B06), Guo et al. (2011, G11), and Henriques et al. (2015, H15). Although these SAMs are all implemented on the Millennium simulations and model the processes of galaxy formation in a somewhat similar way, they differ in various details. These differences lead to different predictions of GGL and G3L. Therefore, by comparing SAMs predictions for various galaxy populations against each other we obtain information on the physical processes leading to the predicted signal and how the different treatment used in the models impact the signal. Since a SAM should be able to explain the observational measurements, we compared the SAMs predictions to the GGL and G3L measurements of Canada-France-Hawaii Telescope Lensing Survey (CFHTLenS). By selecting galaxy samples resembling CFHTLenS galaxy samples, we investigated whether SAMs can reproduce the observational trends.

We started in chapter 2 by summarizing the important aspects of the standard model of cosmology that we use to describe the Universe. We explained how the structures we observe today are the consequence of tiny perturbations in the matter density field in the very early times. We can infer statistical properties of the structures in the linear regime (where the fluctuations in the density field are small) by using linear perturbation theory. In the non-linear regime however, where the fluctuations in the density field are considerably larger, we must rely on cosmological numerical simulations. A large portion of the chapter is dedicated to describe dark matter N-body simulations and SAMs. These SAMs provide a powerful tool to include galaxies in dark matter simulations. The chapter ends by introducing the SAMs used for this thesis and emphasizing their similarities and differences.

In chapter 3, gravitational lensing effect was analyzed. We introduced GGL and G3L, defined the related second- and third-order correlation functions, and gave the corresponding estimators. We also discussed how we can infer lensing information from the simulations by applying ray-tracing algorithms.

We used the G11 and B06 SAMs to investigate GGL and G3L with aperture statistics for various populations of galaxies in chapter 4. We explained the concept of second- and third-order galaxy bias. We selected galaxies according to their color and their magnitude. We argued that GGL and G3L

measurements provide valuable information on the clustering properties of galaxies and the underlying matter density. We showed that although the predictions of GGL and G3L for both models are in qualitative agreement, there are large quantitative discrepancies. The B06 model predicts larger GGL and G3L signals compared to the G11 model. There is a large amplitude ratio between the model predictions for the red and blue galaxy samples, which indicates that red galaxies are more clustered than blue galaxies. When comparing the amplitude ratio between the second- and third-order predictions, we concluded that second-order biasing differs from that of third-order and that the third-order statistics provide new information that is not obtained by the second-order statistics.

To have a better understanding of the differences in the model, we compared model predictions of GGL and G3L to the CFHTLenS measurements for various stellar mass samples in chapter 5. Our results show that not all models can explain the observational measurements and thus their validity can be questioned. Although they can all predict the qualitative behavior of the CFHTLenS measurements, they fail to present a quantitative agreement with observations. This is particularly seen in the B06 model where the amplitude of signal is larger for all measurements except for galaxies with high stellar masses. We argued that the stellar mass distribution of galaxies in the SAMs varies only slightly between the models and observation, therefore the differences in the predictions can not be explained by systematic errors in stellar mass estimates. The power spectrum increases with the average number of galaxies and the bi-spectrum increases with the average number of galaxy pair in a halo of given mass. Therefore, we concluded that the large amplitude predicted by the B06 is due to over-production of satellite galaxies in massive halos.

The G3L correlation function can be expressed by an alternative method, the excess mass map. In chapter 6, we introduced a method that gives a visualization of matter density profile around pairs of galaxies with fixed angular separation. The excess mass map quantifies the excess in the matter density field around galaxy pairs relative to the matter density profile around individual galaxies. We introduced the estimators and presented the SAMs predictions of the excess mass map for redshift-selected samples. Moreover, we showed the CFHTLenS measurements for the same galaxy samples. The comparison between the SAMs and CFHTLenS agrees well with the results presented in the previous chapters. While all SAMs predict a larger amplitude for the excess mass map compared to CFHTLenS, the effect is seen more prominently in the B06 model. Moreover, the structures and patterns seen in the CFHTLenS measurements are not present in the SAMs predictions.

Outlook

We are living in an era of tremendous achievements in the field of astronomy. This is partly due to progress in observational instruments which can now provide us with vast amounts of data. Although CFHTLenS is one of the completed multi-color optical surveys optimised for weak lensing analysis, it covers a rather small area of the sky (154 $\deg^2$) in comparison with some ongoing optical wide and deep fields imaging surveys. The Kilo Degree Survey (KiDS)[1] covers an area 10 times larger than CFHTLenS, and the Dark Energy Survey (DES)[2] will image about 5000 $\deg^2$ of the sky by the end of its five-year mission. These surveys can image millions of galaxies with accurate redshift and shape measurements. These surveys with improved shear measurements will be able to measure GGL and G3L with higher accuracy. This will allow us to better understand clustering properties of foreground galaxies with the underlying matter distribution.

Another important aspect is related to the cosmological simulations. Thanks to the constantly increasing numerical power and the improving efficiency of numerical codes, one can expect to have dark matter simulations with improved mass resolution and larger volumes. It will enable the resolution of structures both on small and large scales, respectively. This is already the case with the Millennium-II simulation (Boylan-Kolchin et al. 2009) with 125 times better mass resolution and the Millennium-XXL simulation (Angulo et al. 2012) which has 200 times more volume than the Millennium simulation. Combining them with SAMs in a post-processing step would allow us to improve our understanding and modelling of the processes governing galaxy evolution.

We showed that we can constrain SAMs using GGL, G3L, and lensing observations. Since GGL and G3L measure the correlation in the galaxy and matter density fields, we obtained information on the clustering properties of galaxies and galaxy pairs. G3L also provides valuable new information that is not attainable by considering second-order only. With accurate shear measurement from the ongoing surveys, new measurements of G3L will be available soon. These measurements provide not only valuable insight on the matter environment of galaxy pairs, but also the testbed for the development of SAMs. Currently, it is believed that SAMs produce too many satellite galaxies that turn red too fast. This could be due to inaccurate gas cooling rates and merging history of galaxies. More accurate GGL and G3L measurements could help us not only to improve these aspects, but also to uncover the numerical and theoretical reasons for the non-trivial discrepancies between the different SAMs.

It is true that significant progress has been made since the initial attempt to implement SAMs (White & Frenk 1991). However, the work presented in this thesis shows that these models must still be improved. Recent improvements in the SAMs make them "modular" and "costumizable". For instance the *Semi-Analytic Galaxy Evolution* (SAGE, Croton et al. 2016) can be implemented on various N-body simulations as long as their halos and their corresponding merging tree have the appropriate format. This will allow one to use all the aspects of different simulations to reproduce various observations simultaneously. Recently, Kamdar et al. (2016) used machine learning techniques to model galaxy formation. They studied in particular halo-galaxy connection by using the G11 model implemented on the Millennium simulation to test their machine learning algorithms. The advantage of using this technique is the high computational efficiency and powerful capability to make predictions of complex physical models on large and high-dimensional datasets. With all these advances, the future of N-body simulations and SAMs looks promising.

[1] http://kids.strw.leidenuniv.nl/index.php
[2] https://www.darkenergysurvey.org

APPENDIX A

Shot-noise correction

Assume a realization $(\boldsymbol{\vartheta}_i^{(r)})$, $i = 1, \ldots, N_\mathrm{g}$, of a set of N_g galaxies with sky positions $\boldsymbol{\vartheta}_i^{(r)}$ in a field $\mathcal{A}$ with area A and mean galaxy number density of $\bar{n}_\mathrm{g} = N_\mathrm{g}/A$. Assume that each galaxy position is distributed in the field according to an underlying 'true' number density field $n_\mathrm{g}(\boldsymbol{\vartheta})$. The ensemble average of a quantity $o(\boldsymbol{\vartheta})$ over all realizations reads:

$$\langle o(\boldsymbol{\vartheta})\rangle = \left[\prod_{k=1}^{N_\mathrm{g}} \frac{1}{N_\mathrm{g}} \int_\mathcal{A} \mathrm{d}^2\boldsymbol{\vartheta}_k^{(r)}\, n(\boldsymbol{\vartheta}_k^{(r)})\right] o(\boldsymbol{\vartheta})\,. \tag{A.1}$$

For each realization, the random positions of the galaxies provide an estimate of the density field n_g:

$$\hat{n}_\mathrm{g}^{(r)}(\boldsymbol{\vartheta}) = \sum_{i=1}^{N_\mathrm{g}} \delta_\mathrm{D}\left(\boldsymbol{\vartheta} - \boldsymbol{\vartheta}_i^{(r)}\right). \tag{A.2}$$

This estimator is unbiased:

$$\begin{aligned}
\left\langle \hat{n}_\mathrm{g}^{(r)}(\boldsymbol{\vartheta})\right\rangle &= \left[\prod_{k=1}^{N_\mathrm{g}} \frac{1}{N_\mathrm{g}} \int_\mathcal{A} \mathrm{d}^2\boldsymbol{\vartheta}_k^{(r)}\, n_\mathrm{g}(\boldsymbol{\vartheta}_k^{(r)})\right] \sum_{i=1}^{N_\mathrm{g}} \delta_\mathrm{D}\left(\boldsymbol{\vartheta} - \boldsymbol{\vartheta}_i^{(r)}\right) \\
&= \sum_{i=1}^{N_\mathrm{g}} \left[\prod_{k=1}^{N_\mathrm{g}} \frac{1}{N_\mathrm{g}} \int_\mathcal{A} \mathrm{d}^2\boldsymbol{\vartheta}_k^{(r)}\, n_\mathrm{g}(\boldsymbol{\vartheta}_k^{(r)})\right] \delta_\mathrm{D}\left(\boldsymbol{\vartheta} - \boldsymbol{\vartheta}_i^{(r)}\right) \\
&= \sum_{i=1}^{N_\mathrm{g}} \frac{1}{N_\mathrm{g}} \int_\mathcal{A} \mathrm{d}^2\boldsymbol{\vartheta}_i^{(r)}\, n_\mathrm{g}(\boldsymbol{\vartheta}_i^{(r)}) \delta_\mathrm{D}\left(\boldsymbol{\vartheta} - \boldsymbol{\vartheta}_i^{(r)}\right) \\
&= n_\mathrm{g}(\boldsymbol{\vartheta}).
\end{aligned} \tag{A.3}$$

Using a filter function $U(\boldsymbol{\vartheta})$, we define a filtered density field $\mathcal{N}$ by:

$$\mathcal{N}(\boldsymbol{\vartheta}; U) = \int_\mathcal{A} \mathrm{d}^2\boldsymbol{\vartheta}'\, U(\boldsymbol{\vartheta} - \boldsymbol{\vartheta}')\, n_\mathrm{g}(\boldsymbol{\vartheta}')\,. \tag{A.4}$$

An estimator for the filtered field reads:

$$\hat{\mathcal{N}}^{(r)}(\boldsymbol{\vartheta}; U) = \int_{\mathcal{A}} \mathrm{d}^2\boldsymbol{\vartheta}'\, U(\boldsymbol{\vartheta} - \boldsymbol{\vartheta}')\, \hat{n}_{\mathrm{g}}^{(r)}(\boldsymbol{\vartheta}') = \sum_{i=1}^{N_{\mathrm{g}}} U(\boldsymbol{\vartheta} - \boldsymbol{\vartheta}_i^{(r)}). \tag{A.5}$$

Its expectation value

$$\begin{aligned}
\left\langle \hat{\mathcal{N}}^{(r)}(\boldsymbol{\vartheta}; U) \right\rangle_r &= \left[\prod_{k=1}^{N_{\mathrm{g}}} \frac{1}{N_{\mathrm{g}}} \int_{\mathcal{A}} \mathrm{d}^2\boldsymbol{\vartheta}_k^{(r)}\, n_{\mathrm{g}}(\boldsymbol{\vartheta}_k^{(r)}) \right] \sum_{i=1}^{N_{\mathrm{g}}} U(\boldsymbol{\vartheta} - \boldsymbol{\vartheta}_i^{(r)}) \\
&= \sum_{i=1}^{N_{\mathrm{g}}} \frac{1}{N_{\mathrm{g}}} \int_{\mathcal{A}} \mathrm{d}^2\boldsymbol{\vartheta}_i^{(r)}\, n_{\mathrm{g}}(\boldsymbol{\vartheta}_i^{(r)}) U(\boldsymbol{\vartheta} - \boldsymbol{\vartheta}_i^{(r)}) \\
&= \int_{\mathcal{A}} \mathrm{d}^2\boldsymbol{\vartheta}'\, n_{\mathrm{g}}(\boldsymbol{\vartheta}') U(\boldsymbol{\vartheta} - \boldsymbol{\vartheta}') \\
&= \mathcal{N}(\boldsymbol{\vartheta}; U).
\end{aligned} \tag{A.6}$$

Consider the square of the filtered density

$$\mathcal{N}^2(\boldsymbol{\vartheta}; U) = \int_{\mathcal{A}} \mathrm{d}^2\boldsymbol{\vartheta}' \int_{\mathcal{A}} \mathrm{d}^2\boldsymbol{\vartheta}''\, U(\boldsymbol{\vartheta} - \boldsymbol{\vartheta}')\, U(\boldsymbol{\vartheta} - \boldsymbol{\vartheta}'')\, n_{\mathrm{g}}(\boldsymbol{\vartheta}')\, n_{\mathrm{g}}(\boldsymbol{\vartheta}''). \tag{A.7}$$

A naive estimator is provided by:

$$\begin{aligned}
\left\langle [\hat{\mathcal{N}}^{(r)}(\boldsymbol{\vartheta}; U)]^2 \right\rangle &= \left[\prod_{k=1}^{N_{\mathrm{g}}} \frac{1}{N_{\mathrm{g}}} \int_{\mathcal{A}} \mathrm{d}^2\boldsymbol{\vartheta}_k^{(r)}\, n_{\mathrm{g}}(\boldsymbol{\vartheta}_k^{(r)}) \right] \\
&\qquad \times \sum_{i=1}^{N_{\mathrm{g}}} U(\boldsymbol{\vartheta} - \boldsymbol{\vartheta}_i^{(r)}) \sum_{j=1}^{N_{\mathrm{g}}} U(\boldsymbol{\vartheta} - \boldsymbol{\vartheta}_j^{(r)}) \\
&= \sum_{\substack{i \neq j \\ i,j=1}}^{N_{\mathrm{g}}} \frac{1}{N_{\mathrm{g}}^2} \int_{\mathcal{A}} \mathrm{d}^2\boldsymbol{\vartheta}_i^{(r)} \int_{\mathcal{A}} \mathrm{d}^2\boldsymbol{\vartheta}_j^{(r)}\, n_{\mathrm{g}}(\boldsymbol{\vartheta}_i^{(r)})\, n_{\mathrm{g}}(\boldsymbol{\vartheta}_j^{(r)}) \\
&\qquad \times U(\boldsymbol{\vartheta} - \boldsymbol{\vartheta}_i^{(r)})\, U(\boldsymbol{\vartheta} - \boldsymbol{\vartheta}_j^{(r)}) \\
&\quad + \sum_{i=1}^{N_{\mathrm{g}}} \frac{1}{N_{\mathrm{g}}} \int_{\mathcal{A}} \mathrm{d}^2\boldsymbol{\vartheta}_i^{(r)}\, n_{\mathrm{g}}(\boldsymbol{\vartheta}_i^{(r)}) U(\boldsymbol{\vartheta} - \boldsymbol{\vartheta}_i^{(r)})^2 \\
&= \frac{N_{\mathrm{g}}(N_{\mathrm{g}} - 1)}{N_{\mathrm{g}}^2} \mathcal{N}^2(\boldsymbol{\vartheta}; U) + \mathcal{N}(\boldsymbol{\vartheta}; U^2).
\end{aligned} \tag{A.8}$$

Hence, this estimator is biased. The first term of the last line is actually what is intended to be measured as aperture dispersion (up to a prefactor close to unity). The second term is due to shot noise arising

from the Poisson sampling of the density field. An unbiased estimator of $\mathcal{N}^2$ is provided by

$$\frac{N_\mathrm{g}}{N_\mathrm{g}-1}\left\{[\hat{\mathcal{N}}^{(r)}(\boldsymbol{\vartheta};U)]^2-\hat{\mathcal{N}}^{(r)}(\boldsymbol{\vartheta};U^2)\right\}=\frac{N_\mathrm{g}}{N_\mathrm{g}-1}\times\sum_{\substack{i\neq j\\ i,j=1}}^{N_\mathrm{g}}U(\boldsymbol{\vartheta}-\boldsymbol{\vartheta}_i^{(r)})U(\boldsymbol{\vartheta}-\boldsymbol{\vartheta}_j^{(r)}). \tag{A.9}$$

By projecting the galaxy positions of a realization onto a mesh (e.g. using Nearest-Grid-Point assignment), one obtains a discretized representation of the density estimate (A.2). The density estimate on the mesh can then be convolved, e.g. by using FFTs, with the filters U and U^2 to obtain gridded versions of the unbiased estimates for $\mathcal{N}_U$ and $\mathcal{N}_{U^2}$. The latter estimate can then be subtracted point-wise from the square of the former estimate to calculate the unbiased estimate (A.9).

Bibliography

Adelman-McCarthy, J. K., Agüeros, M. A., Allam, S. S., et al. 2006, ApJS, 162, 38

Angulo, R. E. & Hilbert, S. 2015, MNRAS, 448, 364

Angulo, R. E., Springel, V., White, S. D. M., et al. 2012, MNRAS, 426, 2046

Angulo, R. E. & White, S. D. M. 2010, MNRAS, 405, 143

Bardeen, J. M., Bond, J. R., Kaiser, N., & Szalay, A. S. 1986, ApJ, 304, 15

Bartelmann, M. & Schneider, P. 2001, Phys. Rep., 340, 291

Baugh, C. M. 2006, Reports on Progress in Physics, 69, 3101

Benson, A. J., Bower, R. G., Frenk, C. S., et al. 2003, ApJ, 599, 38

Benson, A. J., Frenk, C. S., Lacey, C. G., Baugh, C. M., & Cole, S. 2002, MNRAS, 333, 177

Bett, P. 2012, MNRAS, 420, 3303

Binney, J. & Tremaine, S. 1987, Galactic dynamics (Princeton, NJ, Princeton University Press, 1987, 747 p.)

Bower, R. G., Benson, A. J., Malbon, R., et al. 2006, MNRAS, 370, 645

Boylan-Kolchin, M., Springel, V., White, S. D. M., Jenkins, A., & Lemson, G. 2009, MNRAS, 398, 1150

Brainerd, T. G., Blandford, R. D., & Smail, I. 1996, ApJ, 466, 623

Bruzual, G. & Charlot, S. 2003, MNRAS, 344, 1000

Bruzual A., G. & Charlot, S. 1993, ApJ, 405, 538

Chabrier, G. 2003, PASP, 115, 763

Clampitt, J., Sánchez, C., Kwan, J., et al. 2016, ArXiv e-prints 1603.05790

Cole, S., Lacey, C. G., Baugh, C. M., & Frenk, C. S. 2000, MNRAS, 319, 168

Colless, M., Dalton, G., Maddox, S., et al. 2001, MNRAS, 328, 1039

Cooray, A. & Sheth, R. 2002, Phys. Rep., 372, 1

Crittenden, R. G., Natarajan, P., Pen, U.-L., & Theuns, T. 2002, ApJ, 568, 20

Croton, D. J., Springel, V., White, S. D. M., et al. 2006, MNRAS, 365, 11

Croton, D. J., Stevens, A. R. H., Tonini, C., et al. 2016, ApJS, 222, 22

Davis, M., Efstathiou, G., Frenk, C. S., & White, S. D. M. 1985, ApJ, 292, 371

de la Torre, S., Meneux, B., De Lucia, G., et al. 2011, A&A, 525, A125

De Lucia, G. & Blaizot, J. 2007, MNRAS, 375, 2

De Lucia, G., Boylan-Kolchin, M., Benson, A. J., Fontanot, F., & Monaco, P. 2010, MNRAS, 406, 1533

De Lucia, G., Kauffmann, G., & White, S. D. M. 2004, MNRAS, 349, 1101

Dekel, A. & Lahav, O. 1999, ApJ, 520, 24

Dodelson, S. 2003, Modern cosmology Amsterdam (Netherlands): Academic Press. ISBN 0-12-219141-2, 2003, XIII + 440 p.)

Eke, V. R., Navarro, J. F., & Frenk, C. S. 1998, ApJ, 503, 569

Erben, T., Hildebrandt, H., Miller, L., et al. 2013, MNRAS, 433, 2545

Ferrara, A., Bianchi, S., Cimatti, A., & Giovanardi, C. 1999, ApJS, 123, 437

Font, A. S., Bower, R. G., McCarthy, I. G., et al. 2008, MNRAS, 389, 1619

Frigo, M. & Johnson, S. G. 2005, Proceedings of the IEEE, 93, 216, invited paper, special issue on "The Design and Implementation of FFTW3".

Gladders, M. D. & Yee, H. K. C. 2005, ApJS, 157, 1

Gnedin, N. Y. 2000, ApJ, 542, 535

Guo, Q., White, S., Boylan-Kolchin, M., et al. 2011, MNRAS, 413, 101

Hartlap, J., Simon, P., & Schneider, P. 2007, A&A, 464, 399

Henriques, B. M. B., White, S. D. M., Thomas, P. A., et al. 2015, MNRAS, 451, 2663

Henriques, B. M. B., White, S. D. M., Thomas, P. A., et al. 2013, MNRAS, 431, 3373

Heymans, C., Van Waerbeke, L., Miller, L., et al. 2012, MNRAS, 427, 146

Hilbert, S., Hartlap, J., White, S. D. M., & Schneider, P. 2009, A&A, 499, 31

Hildebrandt, H., Erben, T., Kuijken, K., et al. 2012, MNRAS, 421, 2355

Hockney, R. W. & Eastwood, J. W. 1988, Computer simulation using particles (Bristol: Hilger, 1988)

Hoekstra, H., van Waerbeke, L., Gladders, M. D., Mellier, Y., & Yee, H. K. C. 2002, ApJ, 577, 604

Jain, B., Seljak, U., & White, S. 2000, ApJ, 530, 547

Johnston, D. E. 2006, MNRAS, 367, 1222

Johnston, D. E., Sheldon, E. S., Wechsler, R. H., et al. 2007, ArXiv e-prints 0709.1159

Jullo, E., Rhodes, J., Kiessling, A., et al. 2012, ApJ, 750, 37

Kaiser, N. 1984, ApJ, 284, L9

Kaiser, N. 1998, ApJ, 498, 26

Kaiser, N. & Squires, G. 1993, ApJ, 404, 441

Kamdar, H. M., Turk, M. J., & Brunner, R. J. 2016, MNRAS, 455, 642

Kauffmann, G., Colberg, J. M., Diaferio, A., & White, S. D. M. 1999, MNRAS, 303, 188

Kennicutt, Jr., R. C. 1983, ApJ, 272, 54

Kilbinger, M., Schneider, P., & Eifler, T. 2006, A&A, 457, 15

Kim, H.-S., Baugh, C. M., Cole, S., Frenk, C. S., & Benson, A. J. 2009, MNRAS, 400, 1527

Kleinheinrich, M., Schneider, P., Rix, H.-W., et al. 2006, A&A, 455, 441

Knebe, A., Pearce, F. R., Thomas, P. A., et al. 2015, MNRAS, 451, 4029

Lacey, C. & Cole, S. 1993a, in First Light in the Universe. Stars or QSO's, ed. B. Rocca-Volmerange, B. Guiderdoni, M. Dennefeld, & J. Tran Thanh Van, 381

Lacey, C. & Cole, S. 1993b, MNRAS, 262, 627

Le Fèvre, O., Vettolani, G., Garilli, B., et al. 2005, A&A, 439, 845

Leauthaud, A., Tinker, J., Bundy, K., et al. 2012, ApJ, 744, 159

Lemson, G. & Virgo Consortium. 2006, ArXiv Astrophysics e-prints 0608019

Li, C., Jing, Y. P., Kauffmann, G., et al. 2007, MNRAS, 376, 984

Mandelbaum, R., Hirata, C. M., Broderick, T., Seljak, U., & Brinkmann, J. 2006a, MNRAS, 370, 1008

Mandelbaum, R., Seljak, U., & Hirata, C. M. 2008, J. Cosmology Astropart. Phys., 8, 6

Mandelbaum, R., Seljak, U., Kauffmann, G., Hirata, C. M., & Brinkmann, J. 2006b, MNRAS, 368, 715

Maraston, C. 2005, MNRAS, 362, 799

McBride, C. K., Connolly, A. J., Gardner, J. P., et al. 2011, ApJ, 726, 13

Miller, L., Heymans, C., Kitching, T. D., et al. 2013, MNRAS, 429, 2858

Mo, H. J., Jing, Y. P., & White, S. D. M. 1996, MNRAS, 282, 1096

Navarro, J. F., Frenk, C. S., & White, S. D. M. 1997, ApJ, 490, 493

Okamoto, T., Gao, L., & Theuns, T. 2008, MNRAS, 390, 920

Peacock, J. A. 1999, Cosmological Physics (Cosmological Physics, by John A. Peacock, pp. 704. ISBN 052141072X. Cambridge, UK: Cambridge University Press, January 1999.)

Peebles, P. J. E. 1970, AJ, 75, 13

Planck Collaboration, Ade, P. A. R., Aghanim, N., et al. 2014, A&A, 571, A16

Saghiha, H., Hilbert, S., Schneider, P., & Simon, P. 2012, A&A, 547, A77

Saghiha, H., Simon, P., Schneider, P., & Hilbert, S. 2016, ArXiv e-prints 1608.08629

Schneider, P. 1996, MNRAS, 283, 837

Schneider, P. 1998, ApJ, 498, 43

Schneider, P. 2005, ArXiv Astrophysics e-prints 0509252

Schneider, P. 2009a, Cosmology Lecture Notes (Argelander-Institute for Astronomy)

Schneider, P. 2009b, Gravitational Lensing Lecture Notes (Argelander-Institute for Astronomy)

Schneider, P., Ehlers, J., & Falco, E. 1999, Gravitational lenses, Astronomy and astrophysics library (Springer)

Schneider, P., Kochanek, C., & Wambsganss, J. 2006, Gravitational lensing: strong, weak and micro, Saas-Fee Advanced Course: Swiss Society for Astrophysics and Astronomy (Springer)

Schneider, P. & Rix, H.-W. 1997, ApJ, 474, 25

Schneider, P., van Waerbeke, L., Jain, B., & Kruse, G. 1998, MNRAS, 296, 873

Schneider, P. & Watts, P. 2005, A&A, 432, 783

Shen, S., Mo, H. J., White, S. D. M., et al. 2003, MNRAS, 343, 978

Silk, J., Di Cintio, A., & Dvorkin, I. 2013, ArXiv e-prints 1312.0107

Simon, P., Erben, T., Schneider, P., et al. 2013, MNRAS, 430, 2476

Simon, P., Hetterscheidt, M., Schirmer, M., et al. 2007, A&A, 461, 861

Simon, P., Schneider, P., & Kübler, D. 2012, A&A, 548, A102

Simon, P., Watts, P., Schneider, P., et al. 2008, A&A, 479, 655

Spergel, D. N., Verde, L., Peiris, H. V., et al. 2003, ApJS, 148, 175

Springel, V., White, S. D. M., Jenkins, A., et al. 2005, Nature, 435, 629

Springel, V., White, S. D. M., Tormen, G., & Kauffmann, G. 2001, MNRAS, 328, 726

Stoughton, C., Lupton, R. H., Bernardi, M., et al. 2002, AJ, 123, 485

Strateva, I., Ivezić, Ž., Knapp, G. R., et al. 2001, AJ, 122, 1861

Toomre, A. 1964, ApJ, 139, 1217

Tormen, G. 1997, MNRAS, 290, 411

Vale, C. & White, M. 2003, ApJ, 592, 699

van Uitert, E., Cacciato, M., Hoekstra, H., et al. 2016, MNRAS, 459, 3251

van Uitert, E., Hoekstra, H., Velander, M., et al. 2011, A&A, 534, A14

van Waerbeke, L. 1998, A&A, 334, 1

Velander, M., van Uitert, E., Hoekstra, H., et al. 2014, MNRAS, 437, 2111

Viola, M., Cacciato, M., Brouwer, M., et al. 2015, MNRAS, 452, 3529

Walsh, D., Carswell, R. F., & Weymann, R. J. 1979, Nature, 279, 381

Watts, P. & Schneider, P. 2005, in IAU Symposium, Vol. 225, Gravitational Lensing Impact on Cosmology, ed. Y. Mellier & G. Meylan, 243–248

White, S. D. M. & Frenk, C. S. 1991, ApJ, 379, 52

Acknowledgement

First, I would like to thank my supervisor, Peter, who started it all and supported my project until the end. He was my brilliant guide who taught me how to think like a scientist. I am also in debt to Patrick who was a second supervisor to me. Thank you, Patrick, for patiently answering all my questions even the stupid ones. I also thank Stefan for all the fruitful comments and discussions we had. Although he is not in Bonn, he always found time to explain to me the complicated simulations. I thank Cristiano who was my mentor since I arrived in Bonn. During my time as a student, I also benefited from being in one of the most expert groups working on gravitational lensing. I thank all my colleagues for that, specially Hendrick, Reiko, Douglas, and Edo. Special thanks to my officemates, Sandra and Sophia, for making the office a happy place. Thank you Sabine, for patiently helping me with all the bureaucratic work.

I am happy that I became friends with some wonderful people during my studies. Among my friends, my special thanks goes to Jean-Claude for his constant support and motivation and for proof reading my entire thesis and helping me to learn python. Thank you to my friends who are not in Bonn anymore, Alina for all the motivating words, Marika for all the scientific and non-scientific discussions. Thank you to Angela for her support and for all the delicious food and to my Silvia for always being there for me even when she was pregnant. Thanks to Ana, Banafsheh, Nadeen, Richard, Ben, Sarah, Behnam, Zeinab, Talayeh, and Wolf (DM).

Last but not least, I will be always in debt to my parents for their endless love and support, and to my sister who is the rock of my life.

My work was partially supported by the Deutsche Forschungsgemeinschaft (DFG) through the Priority Programme 1177 ‘Galaxy Evolution’ (SCHN 342/6, SCHN 342/8–1, and WH 6/3) and through the Transregional Collaborative Research Centre TRR 33 ‘The Dark Universe’, and partially by the Deutsche Forschungsgemeinschaft through the project SI 1769/1-1.